2016

Cyclostratigraphy And Sedimentation Of The Cenomanian/ Turonian Tuscaloosa Marine Shale

Christian Gilbert Kunhardt
University of Mississippi

CYCLOSTRATIGRAPHY AND SEDIMENTATION OF THE CENOMAINAN-TURONIAN TUSCALOOSA MARINE SHALE

A Thesis
presented in partial fulfillment of requirements
for the degree of Master of Science
in the Department of Geology and Geological Engineering
The University of Mississippi

by

Christian G. Kunhardt

December 2016

ABSTRACT

A cyclostratigraphic and geochemical analysis was conducted on the basal high resistivity zone of the Tuscaloosa Marine Shale to determine if orbital forcing is apparent in mineralogical data suites. Geochemical data suites obtained via X-ray diffraction from five cored wells located near the southern Mississippi/Louisiana border were used in the study. The results were used in concert with previously published insolation and biostratigraphic data and unpublished stable carbon isotope data to determine sedimentation rate, to identify and correlate the Cretaceous Oceanic Anoxic Event 2 (OAE 2) recovery period within the studied interval, and to determine the possible mechanisms of orbital forcing. Results from multitaper spectral analysis and average spectral misfit reveal multiple statistically significant stratigraphic frequencies in four of the five studied wells, as well as significant correlation to orbital cyclicity ($p << 0.05$). Sedimentation rates range from 8.811 cm/ky to 12.321 cm/ky and average 10.332 cm/ky. TOC and resistivity values were used to correlate the OAE 2 recovery interval between the studied wells. Calculated durations range from 212 ky in the most distal well location to 251 ky in more proximal locations. The published insolation and unpublished stable carbon isotope data were used to anchor the time scale based on the terminus of OAE 2 at approximately 94 Ma. Based on geochemical proxies, it is proposed that variations in insolation and the hydrologic cycle drove cyclic sedimentation by varying primary productivity and continental weathering.

DEDICATION

For my family.

TABLE OF CONTENTS

LIST OF ABREVIATIONS AND SYMBOLS

ANOVA	Analysis of Variance
ASM	Average Spectral Misfit
C/T	Cenomanian/Turonian
DSDP	Deep Sea Drilling Project
FFT	Fast Fourier Transform
GC	Gulf Coast
GOM	Gulf of Mexico
GR	Gamma Ray
Ky	Thousand Years
MTM	Multitaper Method
MV	Millivolts
My	Million Years
OAE	Oceanic Anoxic Event
ohmm	Ohm Meters
RST	Regressive Systems Tract
SP	Spontaneous Potential
TMS	Tuscaloosa Marine Shale
TOC	Total Organic Carbon
T-R	Transgressive-Regressive
TST	Trangressive Systems Tract
WIS	Western Interior Seaway
XRD	X-Ray Diffraction

ACKNOWLEDGEMENTS

Gratitude is extended to my advisor Dr. Louis Zachos, who provided invaluable guidance during this project throughout its development and execution. Thanks are also due to the members of my thesis committee, Dr. Brian Platt and Dr. Greg Easson, who provided insight and support during my research. Additionally, I am indebted to Dr. Christopher Lowery for sharing unpublished carbon isotope data. I would also like to thank the University of Mississippi Geology and Geological Engineering Department and the Mississippi Mineral Research Institute for providing financial support and access to software/facilities during my graduate studies and research. Finally, this research would not have been possible without the generous donation of data sets by Goodrich Petroleum.

LIST OF TABLES

LIST OF FIGURES

I. INTRODUCTION

The Cenomanian/Turonian Tuscaloosa Marine Shale (TMS) was deposited along the northern border of the proto Gulf of Mexico in what is now Mississippi, Louisiana, and Alabama. Deposition of the TMS is approximately synchronous with the estimated occurrence of Oceanic Anoxic Event 2 (OAE 2), a period of globally widespread black shale deposition. Recent studies have identified precise age dates for OAE 2 in the Eagle Ford Shale in Texas, and the Bridge Creek Limestone in Colorado (Meyers et al., 2012; Eldrett et al., 2015). The high resistivity zone at the base of the TMS, which has been linked to high levels of TOC content, is a superlative candidate to test for inclusion in OAE 2 (Lu et al., 2015). The purpose of this study is to perform cyclostratigraphic and sedimentological analyses on the high resistivity zone of the TMS to determine sedimentation rate, to correlate to the OAE 2 interval, and to compare geochemical proxies for variations in primary productivity and sediment supply.

Cyclostratigraphic analysis is conducted on five geochemical data suites that penetrate the high resistivity zone of the TMS. Thomson's multitaper method (MTM) of spectral estimation identifies significant frequencies in stratigraphic parameters (Thomson, 1982). Carbonate content will be utilized for MTM analysis given the sensitivity of carbonate accumulation to fluctuations in the ocean/climate interface. Average spectral misfit (ASM) utilizes the significant frequencies output by MTM in order to compare stratigraphic cyclicity to quasi-periodic orbital cycles of known duration (Meyers, 2007). The result is a statistically verifiable sedimentation rate for the tested stratigraphic section. If orbital forcing is significant, and the OAE 2 interval can be identified and correlated between the studied wells, the

stratigraphic framework for OAE 2 may be expanded. Additionally, by utilizing established estimates of the age of the OAE 2 termination and currently unpublished stable carbon isotope data for the TMS (Lowery et al., in prep.), a precise time scale for TMS deposition can be developed. Finally, by comparing geochemical proxies for environmental changes to modeled insolation values, the mechanisms of orbital forcing of TMS sedimentation may be inferred.

II. GEOLOGIC SETTING

CRETACEOUS PALEOCLIMATE

The Cretaceous period is commonly noted for high mean sea surface temperatures (Hay, 2008; Hay, 2011). Mean sea surface temperatures are estimated to have been between 30°C and 36°C (Wilson et al., 2002). The Cenomanian/Turonian (C/T) boundary, in particular, is referenced as the "greenhouse climate optimum" or hothouse. (Hay, 2011) The concept of a warmer Cretaceous period arose with Lyell's (1837) discovery of chalk layers in the high latitudes of Denmark and Sweden. The more recent Deep Sea Drilling Project and Ocean Drilling Project have recovered core and produced climate proxy data, especially oxygen stable isotope data, which corroborates the hypothesis of a warm Cretaceous (Huber at al., 2002). The high temperatures of the Cretaceous were exhibited as a lower pole-to-equator thermal gradient. The modern gradient is about 50°C, while the Cretaceous gradient was less than 30°C. Warmer poles led to seasonal ice caps in the earliest Cretaceous, and ice free poles during the C/T thermal maximum (Hay, 2008; Hay, 2011).

Ice free poles at the C/T boundary caused sea level to rise to approximately 250 meters above modern sea level. This global sea level highstand resulted in an increased area of the Earth covered by epeiric and deep marginal seas, 27% of the planet during the C/T highstand compared with 10% at present. The global highstand at the C/T boundary was a second-order eustatic event tied to the complete melting of polar ice leading to the resultant "greenhouse world." (Hay, 2008; Hay, 2011)

Another feature of the mid-Cretaceous is an abundance of black, organic-rich, shale deposits (Schlanger and Jenkyns, 1976; Arthur et al., 1988a; Arthur et al., 1988b; Hay, 2008; Hay, 2011). High temperatures led to high primary productivity and continental weathering. When combined with a high concentration of atmospheric CO_2 resulting from high rates of igneous activity, the nutrient supply from the water column to the sea floor induced high rates of organic carbon deposition and preservation in the form of black shales (Jenkyns, 2010). Additionally, a lack of cold polar water reduced global ocean water circulation which led to periods of ocean anoxia, dysoxia, and euxinia. The period of bituminous shale deposition at the C/T boundary is labeled Cretaceous Oceanic Anoxic Event 2 (OAE 2) (Schlanger and Jenkyns, 1976). Oceanic anoxic events were recurrent during the Cretaceous period. Cretaceous OAE 1 occurred near the Albian/Aptian boundary, and Cretaceous OAE 3 occurred near the Coniacian/Santonian boundary.

STRUCTURAL SETTING

The Gulf of Mexico Basin formed as a result of crustal extension and sea floor spreading during the break-up of Pangea in the early Mesozoic. It is underlain by oceanic crust in the center of the basin, continental crust along the periphery of the basin, and transitional crust in between the two (Bryant et al., 1991; Ewing, 1991; Salvador, 1991). The relief of the basin is mainly derived from second order structural formations caused predominantly by salt kinematics and uplift/subsidence as a result of allogenic plate movement (Ewing, 1991). The Gulf of Mexico Basin is subdivided into three provinces: the eastern carbonate margin, the western compressional margin, and the location of the area of interest of this study, the northwestern progradational margin. The northwestern progradational margin is further subdivided into the

Interior Zone and the Coastal Zone (Ewing, 1991). The area of interest of this study lies within the Interior Zone, and salient structural features of this zone warrant discussion.

The Interior Zone of the northwestern progradational zone is characterized by a series of embayments or basins separated by uplifts or arches (Figure 1) (Ewing, 1991). To the west of the northwestern progradational margin, the San Marcos Arch separates the Rio Grande Embayment to the west from the East Texas Basin, to the east. The East Texas Basin is confined to the east by the Sabine Uplift. The Sabine Uplift was last active during the Late Cretaceous, and was formed as a result of Paleozoic basement and Louann Salt uplift (Ewing, 1991). To the east is the North Louisiana Salt Basin that is bounded to the north and east by the Monroe Uplift and the LaSalle Arch respectively. The Monroe Uplift and the LaSalle Arch additionally bound the Mississippi Salt Basin, the location of the area of interest of this study (Ewing, 1991). The Mississippi Salt Basin is also bounded to the south by the Wiggins arch and to the north and east by the southern extension of the Appalachian Mountains. The Mississippi Salt Basin extends from eastern Louisiana to western Alabama. The basin is characterized by a series of salt diapirs. Additionally, the Tuscaloosa fault zone and the Cretaceous shelf edge lie to the south of the Mississippi Salt Basin (Ewing, 1991; Galloway, 2008).

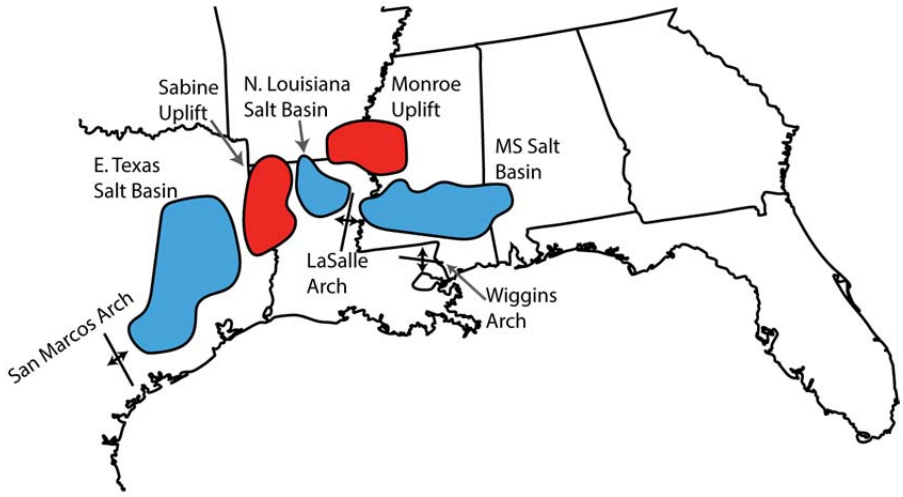

Figure 1: Structural features of the Interior Zone of the Northwest Progradational Margin, GOM basin. Blue represent basins and red represents positive features. Modified from Ewing (1991) and Mancini et al., (2008).

STRATIGRAPHY

Lithostratigraphy

Upper Cretaceous stratigraphic nomenclature of the Gulf of Mexico Basin is defined based on subbasin of deposition and geographic location (Mancini et al., 2008). Nomenclature used in this study will be based on units in western Alabama and east central Mississippi. The oldest Upper Cretaceous units in the Gulf of Mexico Basin were deposited in the early Cenomanian. In southern Mississippi, the early Cenomanian is represented by the uppermost Washita Group. In places, the Dantzler Formation can be recognized (Sohl et al., 1991; Galloway, 2008).

Directly overlying the Washita Group is the middle Cenomanian to Turonian age Tuscaloosa Group (Sohl et al., 1991; Galloway, 2008). The Tuscaloosa Group is informally divided into the lower Tuscaloosa, middle "marine" Tuscaloosa (TMS), and upper Tuscaloosa. The lower Tuscaloosa is further divided into the lower Coker Formation, and upper Gordo

Formation (Sohl et al., 1991). The Coker Formation is a micaceous, crossbedded sandstone interbedded with clay and gravel. The Gordo Formation is characterized by lenticular beds of conglomerate, sandstone, and claystone. The TMS is gray to black, fossiliferous, carboniferous shale, interbedded locally with sandstone. The Upper Tuscaloosa consists of alternating mudstones and sandstones. (Sohl et al., 1991).

Overlying the Tuscaloosa Group is the Coniacian to Santonian age Eutaw Formation (Sohl et al., 1991). The Eutaw Formation is informally divided into a lower and an upper unit. The lower is characterized by laminated, carbonaceous, gray shales that are glauconitic in places. The upper unit is composed of calcareous to non-calcareous sandstone and shale. To the southwest, the Eutaw Group consists of a dense chalk lithology (Sohl et al., 1991).

Sequence Stratigraphy

A detailed sequence stratigraphic framework for US Gulf Coast Upper Cretaceous strata is well documented in the literature (Mancini at al., 1996; Mancini et al., 2005; Mancini and Puckett, 2005; Mancini et al., 2008). The framework characterizes units in terms of third order Transgressive-Regressive (T-R) cycles. Each sequence is bounded by subaerial unconformities along basin margins and condensed sections in the basins. Sequences each contain a transgressive systems tract and a regressive systems tract. The two are separated by a maximum flooding surface (Mancini and Puckett, 2005; Mancini et al., 2008). Given these definitions of sequence boundaries, each third order sequence can be numbered. The formations described in the above section comprise sequences T-R Gulf Coast (GC) 10, T-R GC 11, and T-R GC 12. The Tuscaloosa Group represents one complete sequence, T-R GC 11 (Mancini and Puckett, 2005; Mancini et al., 2008).

The Lower Tuscaloosa comprises the aggrading facies of the TST of T-R GC 11. The TMS comprises the backstepping facies of the TST, and the maximum flooding surface of the third order transgression can be identified in spontaneous potential or gamma ray wireline logs. Finally, the Upper Tuscaloosa comprises the prograding facies of the RST of T-R GC 11. The Tuscaloosa Group unconformably overlies the Washita Group, and unconformably underlies the Eutaw Group (Mancini and Puckett, 2005; Mancini et al., 2008).

Biostratigraphy

The Tuscaloosa Group, as observed in outcrop at its type location, is assigned to the *Complexiopolis-Atlantopollis* Pollen Assemblage Zone (Sohl, 1991). However, the subcropping Tuscaloosa Group located further to the south and west in the study area has been classified as older. Based on planktonic microfossils, the Tuscaloosa Group of the study area belongs to the *Rotalipora cushmani-greenhornensis* and *Helvetoglobotruncana helvetica* subzones of the Late Cenomanian-Turonian Cretaceous (Mancini et al., 1996). The subzones are distinguished via the extinction of *R. appenninica* and *R. cushmani,* and the emergence of *H. helvetica* (Mancini et al., 1996). Definition of biostratigraphic assemblage zones has been the primary mode of chronostratigraphy within the Tuscaloosa Group.

DEPOSITIONAL ENVIRONMENT

Deposition of the Tuscaloosa Group initiated after a brief depositional hiatus (~2.5 My) following the deposition of the Washita Group (Galloway, 2008). During the hiatus, subaerial erosion resulted in large incised valleys throughout the northwestern progradational margin of the Gulf of Mexico. Uplift of the Mississippi embayment and elevation of the Sabine and Monroe uplifts associated with Laramide compression provided topographic relief to reinvigorate fluvial activity in the northern Gulf of Mexico basin (Galloway, 2008).

Transgression associated with the global increase in temperature leading up to the thermal maximum at the C/T boundary led to an upward deepening of the Tuscaloosa Group succession. The oldest Tuscaloosa group sediments are fluvial in origin (Galloway, 2008). As the coastline moved landward, large deltas from ancient Tuscaloosa rivers formed in the Mississippi Salt Basin near the Lower Cretaceous shelf edge. Fluvial deposition transitioned to deltaic deposition (Galloway, 2008). Sediment was sourced from the Appalachian Mountains to the northeast and the Ouachita Mountains to the northwest. Detrital minerals were transported to the Mississippi Salt Basin via ancient Tuscaloosa rivers (Galloway, 2008).

As transgression continued, the shelf was inundated and deltaic deposition transitioned to deposition of marginal marine sandstones (Galloway, 2008). As marine sandstone transitioned to marine shale, deposition of the lower Tuscaloosa terminated, and TMS deposition began. Depending upon the proximity to the Cretaceous shelf break, depositional environment varied from constructional shelf to continental slope (Galloway, 2008). At the complete inundation phase of the transgression, a condensed section formed representing a period of maximum flooding and a depleted sediment supply. As the coastline began moving basinward, marine deposition transitioned back to deltaic sandstone representing the upper Tuscaloosa Formation. The Tuscaloosa Group depositional cycle terminated with subaerial exposure and subsequent erosion of the upper Tuscaloosa Formation (Galloway, 2008).

III. LITERATURE REVIEW

CYCLOSTRATIGRAPHY AND ORBITAL MECHANICS

Although the term *cyclostratigraphy* was coined in the 1980's, the concept that Earth systems operate in stages or cycles has been recognized since the 18th century (Hutton, 1788). In *The Theory of the Earth,* Hutton famously concluded that with respect to cycles between deposition and erosion, "…we find no vestige of a beginning, no prospect of an end" (Hutton, 1788). Herschel (1830) built on this conclusion and suggested that changes in the geological record should reflect changes in climate caused by cycles in the Earth's orbit. In his seminal work relating ancient sedimentary strata to modern mechanisms of deposition, Lyell (1837) utilized climate changes caused by astronomical forces to explain changes in depositional environments. Gilbert (1895) made the first attempt to derive time scales from alternations in the rock record by measuring alternations in limestone and shale strata in Colorado, USA. Alternations in limestone and shale strata have become a useful and commonly used tool in cyclostratigraphy. The first assignment of stratigraphic cyclicity to orbital geometry came from Bradley (1930), who described varves, and their apparent fit to the precession of equinoxes every ~23,000 years.

Milankovitch (1941) was the first to quantify the degree to which orbital cycles affect the amount of solar radiation that reaches the Earth's surface (insolation). Cycles in insolation cause cycles in Earth's climate which are consequently observable as changes in sea level. The theory failed to gain momentum until analysis of carbon and oxygen stable isotopes provided an accurate proxy for paleotemperature (Schwarzacher, 1993). Time series analysis of stable

isotope data series provided the first quantitative results showing depositional frequencies aligning with Earth's eccentricity, obliquity, and precession of the equinoxes (Schwarzacher, 1993).

Eccentricity is the measure of the deviation of Earth's orbit from a perfect circle. Eccentricity cycles roughly every ~100 ky and ~400 ky. Obliquity, or inclination, measures the angle of Earth's central axis to the orbital plane around the sun. Obliquity cycles ~41 ky. Precession is a measure of the change in hemisphere pointed towards the sun at the equinoxes. Precession cycles every ~19 ky and ~23 ky (Figure 2) (Hays, 1976; de Boer and Smith, 2009). Cycle times noted here are approximate. The actual cycle times have varied through geologic time, and they are a function of the gravitational influence other planetary bodies have on Earth (Laskar, 1989; Berger et al., 1992; Laskar, 1999; Matthews and Frohlich, 2002; Matthews and Al-Husseini, 2010; Berger, 2013; Al-Husseini, 2015; Waltham, 2015). More specific approximations have been modeled for deep time, most notably by Berger et al. (1992), Laskar (1990), Laskar (2004), and Laskar (2011). Most recent cyclostratigraphic analyses use a combination of time series analysis and models of Milankovitch cyclicity to tie changes in strata to periodic changes in climate (Sageman et al., 1997; Meyers et al., 2001; Sageman, 2006; Meyers and Sageman, 2007; Kuiper et al., 2008; Malinverno et al., 2010; Meyers et al., 2012; Cantalejo and Pickering, 2014).

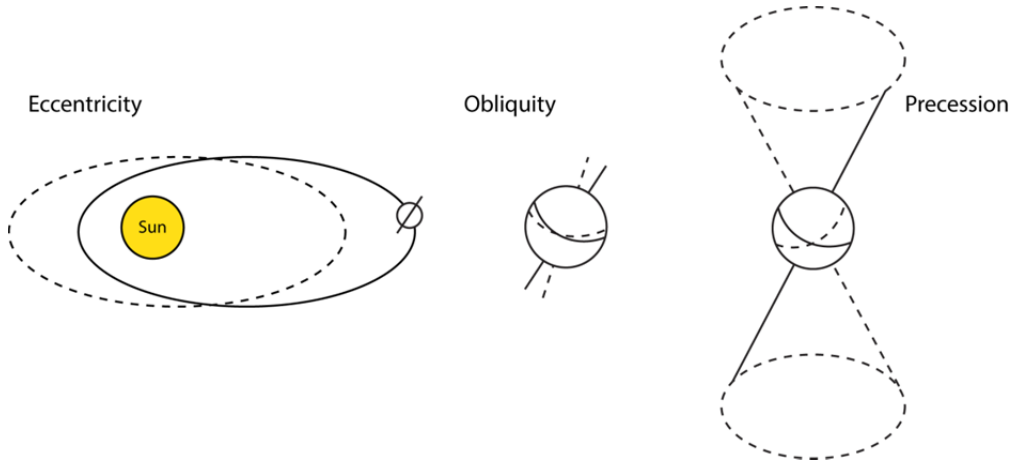

Figure 2: Illustration of Milankovitch processes. Modified from deBoer (1983).

MECHANISMS OF ORBITAL FORCING

It is clear that variations in solar radiation affect temperatures on the Earth's surface. However, the mechanisms that translate changes in climate into variations in sedimentation are less direct (Schwarzacher, 1993). This problem is made more complex by the inclusion of stochastic events and varied sedimentation rates in the stratigraphic record. Such events introduce noise and non-linearity into the stratigraphic record (Schwarzacher, 1993). However, those climatic changes that influence sedimentation have been well documented.

Eustasy

The clearest mechanism of orbital forcing in sedimentary strata is eustasy (global sea-level fluctuations). The volume of the world oceans is controlled by a great number of factors, some of which are in turn controlled by solar insolation. Different factors operate over various time scales and affect sea level to different degrees. Additionally, the factors controlling eustasy vary whether the climate is in icehouse, greenhouse, or hothouse mode (Wendler and Wendler, 2015; Sames et al., 2016, Wendler et al., 2016).

Factors affecting eustasy can be categorized as those that change sea level through increasing or decreasing the capacity (accommodation space) of ocean basins and those that change sea level through increasing or decreasing ocean water volume. Factors that affect the capacity of the ocean basins are mostly tectonic (Wendler and Wendler, 2015; Sames et al., 2016; Wendler et al., 2016). Examples of these mechanisms include mid ocean ridge basalt generation, large igneous province activity, continental collisions, and regional uplift/subsidence. The degree to which these factors alter sea level can be large, but tectonic processes operate in the geological long term, typically over 50 to 100 My (Wendler and Wendler, 2015; Sames et al., 2016; Wendler et al., 2016). These mechanisms operate in all climate modes, but have no direct connection to solar insolation (Wendler and Wendler, 2015; Sames et al., 2016; Wendler et al., 2016).

Conversely, eustatic factors affecting the volume of ocean water are intrinsically linked to changes in climate (Wendler and Wendler, 2015; Sames et al., 2016). The effect of glacial to interglacial cyclicity on sea level, termed glacioeustasy, is the greatest catalyst of sea level change in the icehouse and greenhouse climate modes. Glacioeustasy operates between 10 Ky and 100 Ky timescales (Sames, 2016). However, eustatic changes during hothouse climate modes cannot be resolved by glacioeustasy (Wendler and Wendler, 2015; Sames et al., 2016). In the hothouse climate mode, two climate-driven factors influence eustasy. Changes in water temperature and salinity cause ocean water to expand and contract. This is termed thermosteric eustasy, and causes short term eustatic cycles between 1 year and 10 Ky (Sames, 2016). Changes in climate are also reflected in the volume of water stored on land in either lakes or groundwater (Wendler and Wendler, 2015; Sames et al., 2016; Wendler et al., 2016). Changes in sea level tied to storage and discharge of water stored on continents is termed limnoeustasy

and causes eustatic cycles on the order of 10 Ky (Wendler and Wendler, 2015; Sames et al., 2016; Wendler et al., 2016).

Continental Weathering

The geochemical composition of siliciclastic sedimentary rocks is controlled by the detrital minerals supplied to the deposition site. Sedimentary rock geochemistry is therefore controlled by continental weathering rates which vary with regional tectonics and with shifts in climate and the hydrologic cycle (Chamley, 1989; Hofmann et al., 2001; Beckmann et al., 2005). Periods of high continental weathering coincide with continental uplift (higher hinterland gradients) and humid climates with high precipitation volumes (Wendler et al., 2016). Climate cycles between arid and humid continents can therefore be observed in the sedimentary record (Chamley, 1989; Hofmann et al., 2001; Beckmann et al., 2005; Wendler and Wendler, 2015; Sames et al., 2016; Wendler et al., 2016)

Clay mineralogy of fine grained sedimentary rocks is a uniquely suited proxy for climate change cycles. For instance, clay minerals develop in different types of soils weathered from specific substrata associated with certain climate types (Chamley, 1989; Weaver, 1989; Wignall, 1994; Velde, 1995; Wendler et al., 2016). Additionally, certain clay minerals are more indicative of chemical weathering than others. A prominent mechanism of clay formation is hydrolysis (Chamley, 1989; Weaver, 1989; Velde, 1995). Hydrolysis, which means "destruction by water," is the process by which crystalline minerals (such as aluminosilicates) react with water to form silicic acid, basic solution, and secondary clay minerals (Chamley, 1989). The primary clay species formed by hydrolysis depends on the chemistry of the primary mineral undergoing hydrolysis (Chamley, 1989; Weaver, 1989; Velde, 1995). Based upon the Appalachian source of detrital clay minerals in the TMS, kaolinite is considered to be the

primary product of hydrolysis present in the TMS. Because hydrolysis requires water for the chemical reaction to occur, the process is sensitive to variations in precipitation (Chamley, 1989; Weaver, 1989; Velde, 1995). As a result, variations in kaolinite concentrations relative to other clay species not prone to production via hydrolysis can be considered a proxy for variations in precipitation in the source area (Chamley, 1989; Weaver, 1989; Velde, 1995).

Primary Productivity

Changes in climate also affect primary productivity in the water column. Primary productivity is measurable as the rate of creation of organic material via photosynthesis. Primary producers, or autotrophs, comprise the bottom of the food chain, and therefore have an effect on organism populations and diversity in an ecosystem. Increases or decreases in primary productivity are reflected in marine sedimentary rocks, particularly in fine grained marine sedimentary rocks (Wignall, 1994; Kuypers, 2002; Jenkyns, 2010; Lebedel et al., 2013; van Bentum et al., 2012). Based on its composition, organic material can be classified as either terrestrial or marine (Tissot and Welte, 1978, van Bentum et al., 2012). Increases in marine organic material can therefore be interpreted as increased primary productivity in the water column (Wignall, 1994). Biogenic mineral concentrations, such as calcite, may also vary in sedimentary strata as a result of increases or decreases in primary productivity (Lebedel et al., 2013). Observations of proxies for primary productivity reflect changes in climate, and can be used to interpret orbital cyclicity to the extent that cyclicity affects climate.

CRETACEOUS OCEANIC ANOXIC EVENTS

Oceanic anoxic events were first reported as a result of analysis of data recovered from the Deep Sea Drilling Project in the late 1970s (Schlanger and Jenkyns, 1976). Recovery of core from separate locations in the south central and western North Pacific led to the observation of

several condensed sections of carbonaceous sediment deposited during the same geologic time periods, as dated using index biomarkers. Waxy, greenish black, carbonaceous sediment was consistently recovered from two time intervals in particular: the Barremian-Aptian boundary, and the Cenomanian-Turonian boundary (Schlanger and Jenkyns, 1976). The discovery of pervasive carbonaceous intervals on a global scale led researchers to the conclusion that the intervals were deposited during global events resulting from poor oceanic mixing, rather than from phenomena affecting localized basins. As a result of this conclusion, these events were named Cretaceous Oceanic Anoxic Events 1 and 2 respectively (OAE 1 and OAE 2) (Schlanger and Jenkyns, 1976).

Schlanger and Jenkyns (1976) proposed a geologic interpretation for the widespread, coeval deposition of carbonaceous sediments. Their model relied on two factors: the Late Cretaceous eustatic high and the high global temperatures that have been well documented from $\delta^{18}O$ and other temperature proxies (Schlanger and Jenkyns, 1976). Global eustatic rise led to increased area and volume of shallow and marginal seas. High temperatures diminished the supply of cold oxygenated water to the benthic water layer. The combination of these factors led to high rates of primary production at the surface of shallow and marginal seas, and the increased preservation of organic material on the ocean floor (Schlanger and Jenkyns, 1976).

Schlanger and Jenkyns (1976) first suggested global oceanic anoxia as a driver for carbonaceous preservation in Late Cretaceous deposits. In their research, the authors compared samples from the Cenomanian-Turonian boundary retrieved from core from the Deep Sea Drilling Project (DSDP) and samples taken from Cenomanian-Turonian outcrops from across the globe. DSDP samples were described from the Atlantic Basin, the Caribbean Basin, the Indian Ocean Basin, and the Pacific Basin. Outcrop data were described from Venezuela, the

Mediterranean region, Italy, England, and California (Schlanger and Jenkyns, 1976). The authors observed strata of enhanced organic carbon preservation at each of the studied localities. Samples described are predominantly black marine shales with varying concentrations of terrestrial and marine plant material (Schlanger and Jenkyns, 1976). Additionally, the depositional setting of each sampled locality varied from local, silled basins, to broad rises in the open oceans of the Late Cretaceous. The authors adopted a model of global anoxia to explain the preservation of organic material on this massive scale (Schlanger and Jenkyns, 1976). Two established parameters support the model: eustatic rise associated with the Zuni (Sloss, 1963) sequence, and the Hays-Pitman model (Hays and Pitman, 1973) for rapid sea-floor spreading between the Aptian and Cenomanian. As a result of these processes, 35 x $10^6 km^2$ of new epicontinental seas formed (Schlanger and Jenkyns, 1976). Additionally, mild temperatures at the poles diminished the volume of oxygenated cold water circulating into the benthic water column. The authors labeled the Cenomanian-Turonian event OAE 2 (Schlanger and Jenkyns, 1976).

Since OAE 2 was originally identified, research efforts have focused on delineating the upper and lower boundaries of OAE 2, and improving the interpretation of mechanisms driving the development of a globally anoxic benthic water layer. Because OAE 2 represents a major disruption of the carbon cycle, many researches have focused on analyses of stable carbon isotopes and organic carbon composition as methods for delineating OAE 2 (Jenkyns, 2010). Arthur and Schlanger (1976) were among the first researchers to employ analysis of total organic carbon to describe OAE 2. By correlating the Cenomanian-Turonian marine transgression with an enrichment of organic carbon content in cores recovered from North Atlantic legs of the

DSDP, the authors provided a quantifiable model for delineating OAE 2 (Arthur and Schalnger, 1976).

IV. DATA AND METHODS

DATA AND STUDY AREA

Geochemical data for this study were taken from six core analyses from wells located in southern Mississippi and central Louisiana (Figure 3). Core samples were analyzed from wells drilled in Wilkinson and Pike counties in Mississippi, and East Feliciana and St. Helena parishes in Louisiana. Core data were depth corrected to wireline data using resistivity and gamma ray data. Additionally, wireline logs from 296 wells were used to supplement core data to construct a structure map of the TMS formation top. Wells were chosen based on geographic location, wireline inventory, and log image quality. Spontaneous potential (SP) and resistivity measurements were considered requirements for inclusion in the study. However, most wells also included gamma ray (GR), sonic, and porosity logs.

METHODS

Mapping

A structure map was generated on the top of the TMS (Figure 3). The map was constructed based on 296 wireline logs. Formation picks were referenced to the #1 Spinks type log (Figure 4). The data curves used for picking formations varied based on the age of the data. Generally, spontaneous potential, gamma ray, and resistivity data were used to make formation picks. Maps were generated in ESRI ArcMap using the Spatial Analysis toolbox. The interpolation method used was natural neighbor.

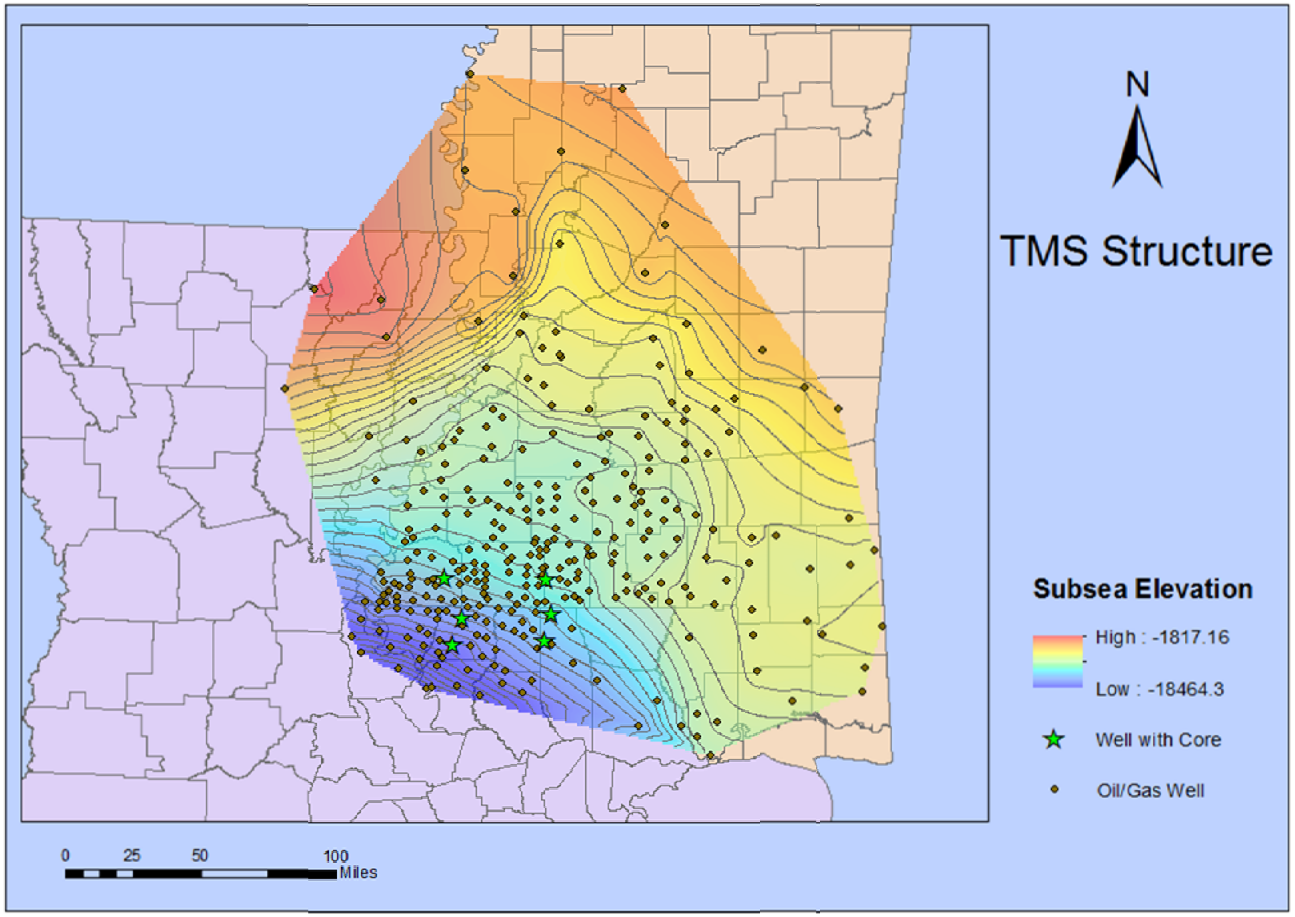

Figure 3: Structure map of the top of the TMS. Depth is in subsea feet.

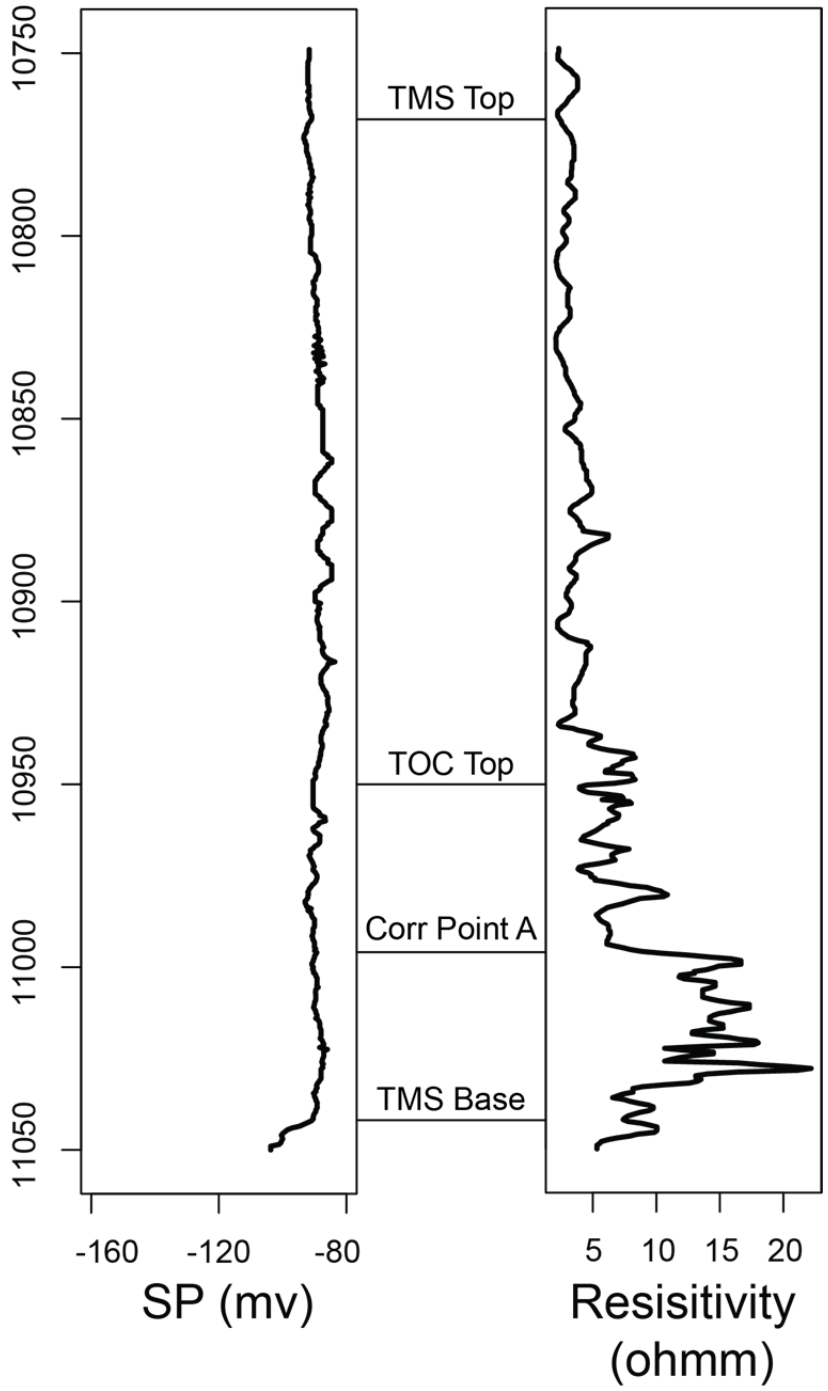

Figure 4: Type log displaying TMS top and base. Also included are the top off the TOC-enriched zone and correlation point A used for correlating from the #1 Spinks well to other cored wells.

Mineralogy

Mineralogy data were analyzed from six wells in Louisiana and Mississippi. With the exception of the #1 Spinks well, the wells were drilled and cored as pilot wells for horizontal drilling programs targeting the TMS. The cored intervals in these wells are the basal, high resistivity zone of the TMS. The #1 Spinks well was drilled as a production test well, and the cored interval includes most of the TMS, including the upper portion of the lower Tuscaloosa.

Mineralogy data from the six cored wells were obtained via X-Ray diffraction (XRD) analysis. XRD whole rock mineralogy reported and analyzed herein is weight percent. Relative clay mineralogy data are calculated from whole rock mineralogy. TOC and other geochemical data were obtained using Rock-Eval pyrolysis and LECO TOC analysis. All laboratory analyses were conducted by external laboratory service companies.

Statistics

Statistical methods are used to identify periodicity in stratigraphic parameters and quantify any orbital forcing in the periodicity. Before any orbital forcing can be determined, periodicity in the depth series must be identified. This objective is made more difficult by noise introduced into the signal by random sedimentation events. Joseph Fourier (1822) introduced the Fast Fourier Transform (FFT), which is a method of transforming a time (or depth) series from the temporal domain to the frequency domain. While FFT is the most commonly used method of time series analysis (Schwarzacher, 1993), its application to stratigraphic time series is problematic (Babadi and Brown, 2014). In principle, FFT requires a sample of infinite length to accurately estimate the spectral density. Relying on a finite sample introduces variance and bias to spectral estimates (Babadi and Brown, 2014). Further complicating spectral estimation of

stratigraphic parameters is that natural phenomenon exhibit cyclicity through stochastic processes (Schwarzacher, 1993; De Boer and Smith, 1994; Berger et al., 1994; Meyers, 2012). As a result, FFT tends to introduce false positives indicating periodicities not driven by cyclic forces (Meyers, 2012).

The solution to this problem is to apply a method of time series analysis that both minimizes the effects of variance and bias, as well as provides a means to test against false positives. Thomson (1982) introduced a method of spectrum estimation that has been subsequently named the Multitaper Method (MTM) that addresses these issues. Additionally, MTM has been applied in many recent cyclostratigraphic studies (Meyers et al., 2001; Sageman et al., 2006; Meyers and Sageman, 2007; Meyers et al., 2012; Cantalejo and Pickering, 2014; Ma et al., 2014). MTM minimizes bias and variance by applying a weighted average of multiple tapers applied to the data series at independent data windows (Thomson, 1982; Babadi and Brown, 2014; Rahim et al., 2014).

MTM is a multiple step process that begins with the design of the tapers, or filters, to be applied to the data series. The tapers most commonly used in MTM analysis are discrete prolate spheroidal sequences (DPSS) as developed by Slepian (1968). To construct the DPSS, the analyst must first define the time (in this case depth)-bandwidth product *NW*, as well as the number of DPSS to use in the analysis, *L* (Lees and Park, 1995; Babadi and Brown, 2014; Rahim, 2014). *NW* is typically chosen as an integer between 2 and 7. This study employs an *NW* of 3. By convention, $L = (2NW) - 1$ (Lees and Park, 1995; Babadi and Brown, 2014; Rahim, 2014). Using these parameters, a symmetric matrix Φ_R is built such that $(\Phi_R)_{k,l} = \frac{\sin(\pi W(k-l))}{\pi(k-l)}$. Each row in Φ_R is the inverse FFT of a rectangular window of width $2W$ centered on increasing

integers from 0 to *N-1* (Thomson, 1982). Principal component analysis of the matrix Φ_R yields *N* orthogonal eigenvectors and associated eigenvalues. The DPSS are the eigenvectors with *L* highest eigenvalues (Lees and Park, 1995; Babadi and Brown, 2014; Rahim, 2014). Because the DPSS are orthogonal, they are uncorrelated and provide independent estimates of the spectral density of the data series. Single taper methods introduce substantial data leakage near the beginning and end of the data series. By utilizing multiple DPSS that are by definition uncorrelated, data leakage from the filtering process is minimized (Lees and Park, 1995; Babadi and Brown, 2014; Rahim, 2014). The FFT spectrum estimate is then determined for each tapered data series, and the resulting spectral estimates are averaged to generate the multitaper spectral estimate (Lees and Park, 1995Babadi and Brown, 2014; Rahim, 2014). A schematic representation of the process is shown in figure 5 (Babadi and Brown, 2014).

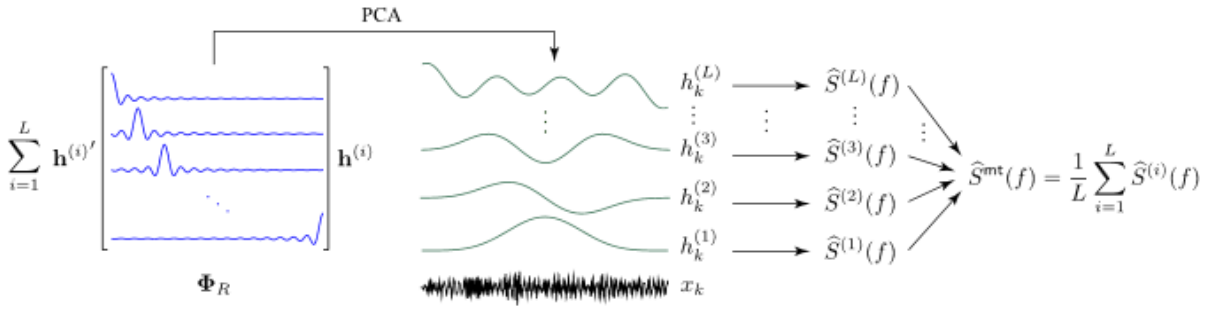

Figure 5: Schematic representation of multitaper spectral estimation from Babadi and Brown (2014). The left panel shows the matrix of waveforms centered on integers between 0 and *N*-1, Φ_R. The next panel shows the DPSS constructed via principal component analysis of waveforms in matrix Φ_R. The right panels show the calculation of Fourier spectral estimates of each tapered data series, and the averaging of each spectral estimate to form the multitaper spectral estimate.

The formula applied is an average of FFT spectral estimates of *L* DPSS and is shown in summation form below (Equation 1):

$$\hat{S}^{mt}(f) = \frac{1}{L}\sum_{i=1}^{L}\hat{S}^{(i)}(f) \qquad \text{(Eq. 1)}$$

Where:

$h_k^{(1)}, h_k^{(2)}, \ldots h_k^{(L)}$ = a set of tapers

L = the number of tapers utilized

$\hat{S}^{(i)}(f) = \Delta\left|\sum_{i=1}^{N-1} h_k^{(i)} x_k e^{-i2\pi k f \Delta}\right|^2 \ (tapered\ spectral\ estimate)$

x = time series to which MTM is applied

For this study, data sets are prepared for spectral analysis in the following ways. First, a regular sampling interval is constructed via linear interpolation. The interpolated sampling interval is determined based on the median sampling interval of the raw data series. Additionally, the raw data series were converted to standard normal form by removing trends and the mean.

Spectral density estimates of stratigraphic parameters return frequencies in cycles per depth unit. In order to convert periodicity from the depth domain into the time domain, the cycles must be compared to known cycles in the time domain. In this study, orbital cycles are used for calibration. Early studies calibrated stratigraphic cyclicity by comparing ratios observed within stratigraphic signals to ratios between the orbital cycles. For instance, the approximate 5:2:1 ratio observed between short eccentricity, obliquity, and precession has been used to

calibrate stratigraphic signals (Meyers and Sageman, 2007). However, this method lacks the ability to test the strength of the fit between stratigraphic and orbital cycles.

Average spectral misfit (ASM), a method of comparing stratigraphic and orbital cycles, developed by Meyers and Sageman (2007), provides a metric to test the strength of fit between stratigraphic and orbital cycles and test the significance against a null hypothesis (no orbital forcing) (Meyers and Sageman, 2007). The metric of ASM is a quantification of the fit between significant stratigraphic frequencies and orbital cycles. Significant frequencies are stretched or contracted in order to minimize misfit between orbital frequencies and stratigraphic frequencies (Figure 6).

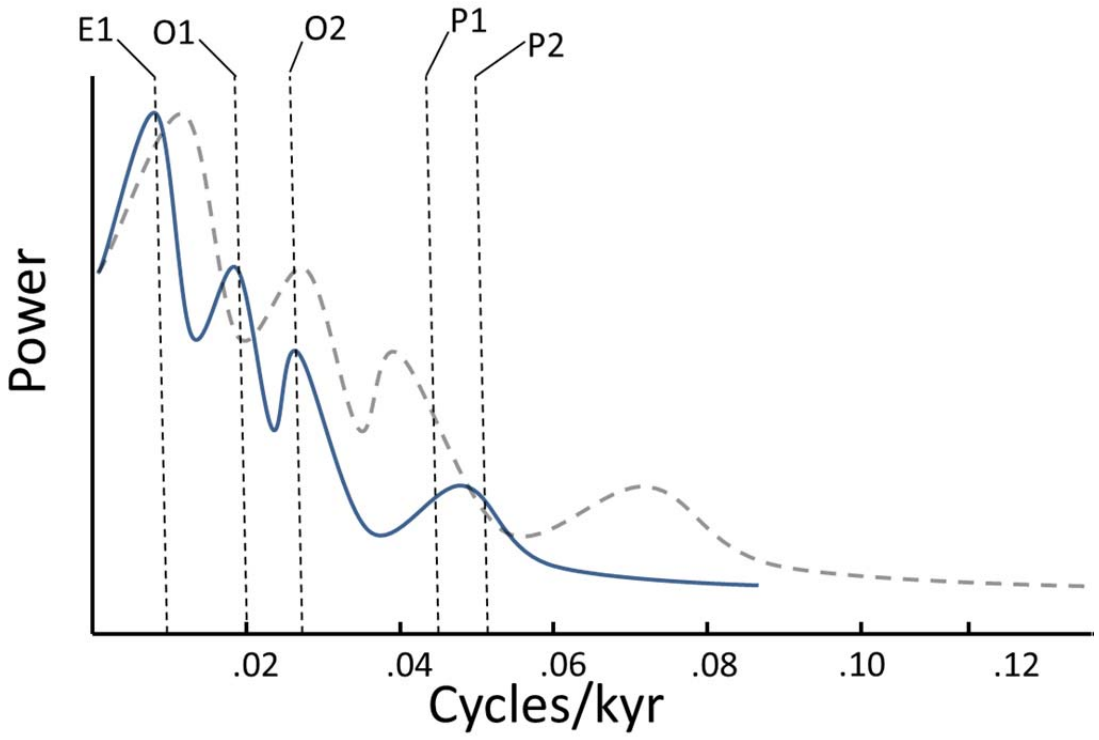

Figure 6: A model showing the process of ASM. In this model, the original frequencies (gray dotted line) are contracted to fit modeled orbital frequencies (vertical dotted lines). Ratios between frequencies are maintained in the optimized model (blue sold line). Modified from Meyers and Sageman (2007).

The orbital models used in this study are the Late Cretaceous estimates developed by Berger et al. (1992). The null hypothesis that no orbital forcing is present is tested through Monte Carlo simulations using 100,000 randomly generated spectra (Meyers and Sageman, 2007). ASM is defined as:

(Eq. 2)

$$ASM = \frac{1}{n}\sum_{k=1}^{n} \alpha_k \; where \; \alpha_k = \begin{cases} 0 & if \left|(f*s) - f_{pred}\right| \leq 0.5 * \Delta f_R * s \\ \left|(f*s) - f_{pred}\right| & if \left|(f*s) - f_{pred}\right| > 0.5 * \Delta f_R * s \end{cases}$$

Where:

n = number of orbital periods in analysis
k = summation index
f = spatial frequency peak location (cycles/meter)
s = sedimentation rate (meters/ky)
f*s = calibrated temporal frequency peak location (cycles/ky)
f_{pred} = predicted orbital frequency (cycles/ky)
Δf_R = spatial frequency resolution bandwidth (cycles/meter), or minimum resolution bandwidth
Δf_R*s = calibrated temporal frequency resolution bandwidth (cycles/ky)

MTM and ASM are conducted using Astrochron: An R package for Astrochronology in R statistical software (Meyers, 2014).

In addition to MTM and ASM, a number of statistical methods were applied to test the robustness of the procedure after results were determined. The first robustness test verified that the results were independent of the interpolation method. Piecewise linear interpolation was used in the initial procedure. To verify that the interpolation method did not influence the results, the procedure was also completed using a natural cubic spline interpolation (Appendix).

Next, potential error in the laboratory mineralogy tests was tested. Because only one data point from each sample depth was produced, a true confidence interval for each data point could not be produced. Therefore, a conservative confidence estimate of 10% above and below the reported value was used. To test that sampling error did not influence MTM results, a random point was calculated within each confidence estimate at each sampled depth. MTM was then conducted on the randomized data series. Results were then compared to MTM results from the original data series and tested for variation. This process was repeated 1,000 times (Appendix).

Finally, in order to validate comparisons between wells, analysis of variance (ANOVA) tests were conducted between carbonate results of the five wells used in the study (Davis, 2002). ANOVA tables were computed in R statistical software. Additionally, Tukey's Honest Significant Difference test was conducted to identify the source of variance between the studied wells. (Appendix).

Figure 7 broadly outlines the method used in this study.

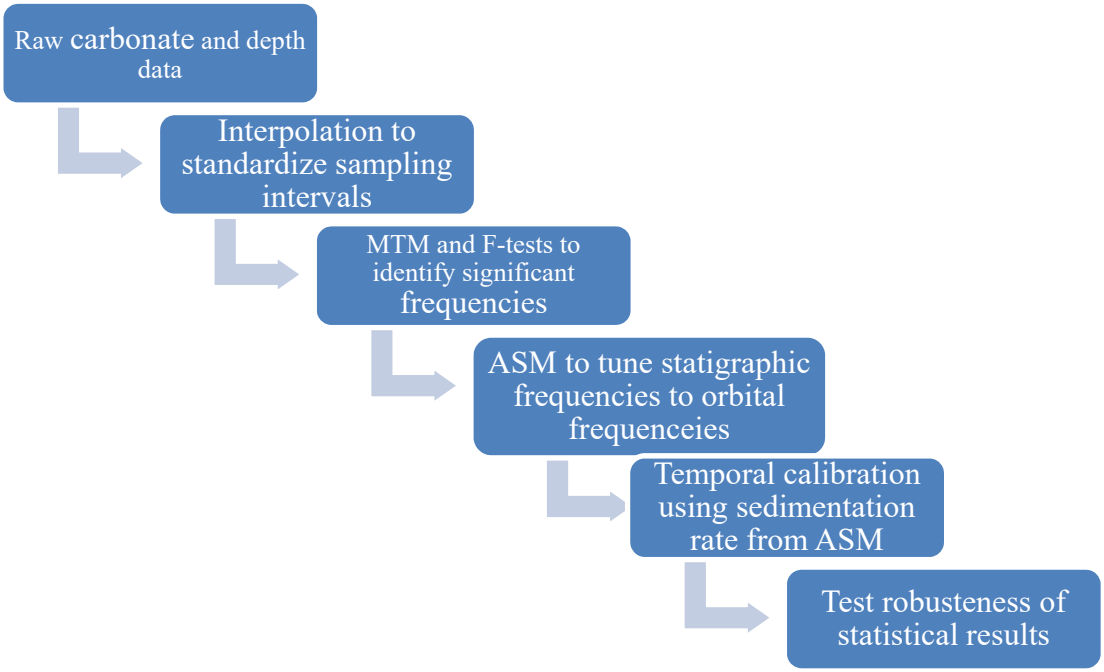

Figure 7: Outline of methods in this study.

V. RESULTS

MINERAL ASSEMBLAGES

Whole Rock Mineral Assemblage

Figures 8 through 12 show whole rock mineralogy data and TOC data for the 5 cored wells included in this study. GR and resistivity are also included to display the stratigraphic framework of the cored interval in each well.

The #1 Spinks core represents continuous footage from 10,750' to 11,060'. 10,750' to 11,030' is TMS. The last 30' between 11,030' and 11,060' was recovered from the lower Tuscaloosa Formation. The result is 280' of continuous TMS core, and represents the most complete interval of TMS core in this study. Average percent tectosilicate in the TMS interval is 14%, and varies from 10% to 20%. Average percent carbonate is 10%, and varies from 0.28% to 27%. Average percent clay is 54% and varies from 35% to 62%. Average percent TOC is 1.38% and varies from 0.75% to 2.85%.

The Beech Grove 94H core was sampled between 13,765' and 13,925'. This represents 160' of sampled core from the basal section of the TMS. The average percent tectosilicate is 37% and varies from 14% to 78%. Average percent carbonate is 20% and varies from 4% to 82%. Average percent clay is 39% and varies from 3% to 63%. Average percent TOC is 1.13% and varies from 0.11% to 2.8%.

The Crosby 12-1H core was sampled between 12,082' and 12,192'. This represents 110' of sampled core from the basal section of the TMS. The average percent tectosilicate is

32% and varies from 19% to 65%. Average percent carbonate is 12% and varies from 0% to 35%. Average percent clay is 52% and varies from 31% to 69%. Average percent TOC is 1.61% and varies from 0.50% to 3.1%.

The Lane 64H core was sampled between 15,056' and 15,238'. This represents 182' of sampled core from the basal section of the TMS. The average percent tectosilicate is 32% and varies from 15% to 57%. Average percent carbonate is 14% and varies from 5% to 58%. Average percent clay is 50% and varies from 16% to 62%. Average percent TOC is 1.08% and varies from 0.49% to 2.1%.

The Soterra 6H core was sampled between 12,481' and 12,617'. This represents 136' of sampled core from the basal section of the TMS. The average percent tectosilicate is 26% and varies from 8% to 77%. Average percent carbonate is 24% and varies from 0% to 75%. Average percent clay is 43% and varies from 9% to 64 %. Average percent TOC is 1.64% and varies from 0.16% to 3.20%.

The Thomas 38H core was sampled between 11,668' and 11,902'. This represents 234' of sampled core from the basal section of the TMS. The average percent tectosilicate is 36% and varies from 14% to 86%. Average percent carbonate is 15% and varies from 0% to 58%. Average percent clay is 45% and varies from 6% to 65 %. Average percent TOC is 1.31% and varies from 0.34% to 3.57%.

Relative Mineral Assemblages

Figures 13 through 17 show relative mineral assemblage data of five of the six cored wells. The #1 Spinks well was not sampled at an adequate interval for inclusion in relative

mineral analysis. Quartz and feldspar contents were normalized to total tectosilicate content. Illite, kaolinite, and chlorite were normalized to total clay content.

The Beech Grove 94H core averages 75% relative quartz and varies from 58% to 95%. Average relative percent potassium feldspar is 12% and varies from 0% to 35%. Average relative percent plagioclase is 12% and varies from 0% to 28%. Average relative percent illite is 23% and varies from 10% to 31%. Average relative percent kaolinite is 26% and varies from 12% to 47%. Average relative percent chlorite is 14% and varies from 7% to 43%.

The Crosby 12-1H core averages 84% relative quartz and varies from 77% to 88%. Average relative percent plagioclase is 16% and varies from 12% to 23%. Average relative percent illite is 30% and varies from 24% to 37%. Average relative percent kaolinite is 28% and varies from 17% to 46%. Average relative percent chlorite is 17% and varies from 13% to 24%.

The Lane 64H core averages 72% relative quartz and varies from 56% to 88%. Average relative percent plagioclase is 18% and varies from 4% to 36%. Average relative percent orthoclase is 9% and varies from 0% to 33%. Average relative percent illite is 33% and varies from 13% to 61%. Average relative percent kaolinite is 31% and varies from 20% to 44%. Average relative percent chlorite is 13% and varies from 4% to 21%.

The Soterra 6H core averages 83% relative quartz and varies from 72% to 94%. Average relative percent plagioclase is 13% and varies from 6% to 22%. Average relative percent orthoclase is 5% and varies from 0% to 13%. Average relative percent illite is 16% and varies from 0% to 37%. Average relative percent kaolinite is 48% and varies from 26% to 68%. Average relative percent chlorite is 9% and varies from 4% to 21%.

The Thomas 38H core averages 83 % relative quartz and varies from 73% to 93%. Average relative percent plagioclase is 13% and varies from 6% to 20%. Average relative percent orthoclase is 4% and varies from 0% to 9%. Average relative percent illite is 30% and varies from 16% to 45%. Average relative percent kaolinite is 40% and varies from 19% to 60%. Average relative percent chlorite is 9% and varies from 2% to 22 %.

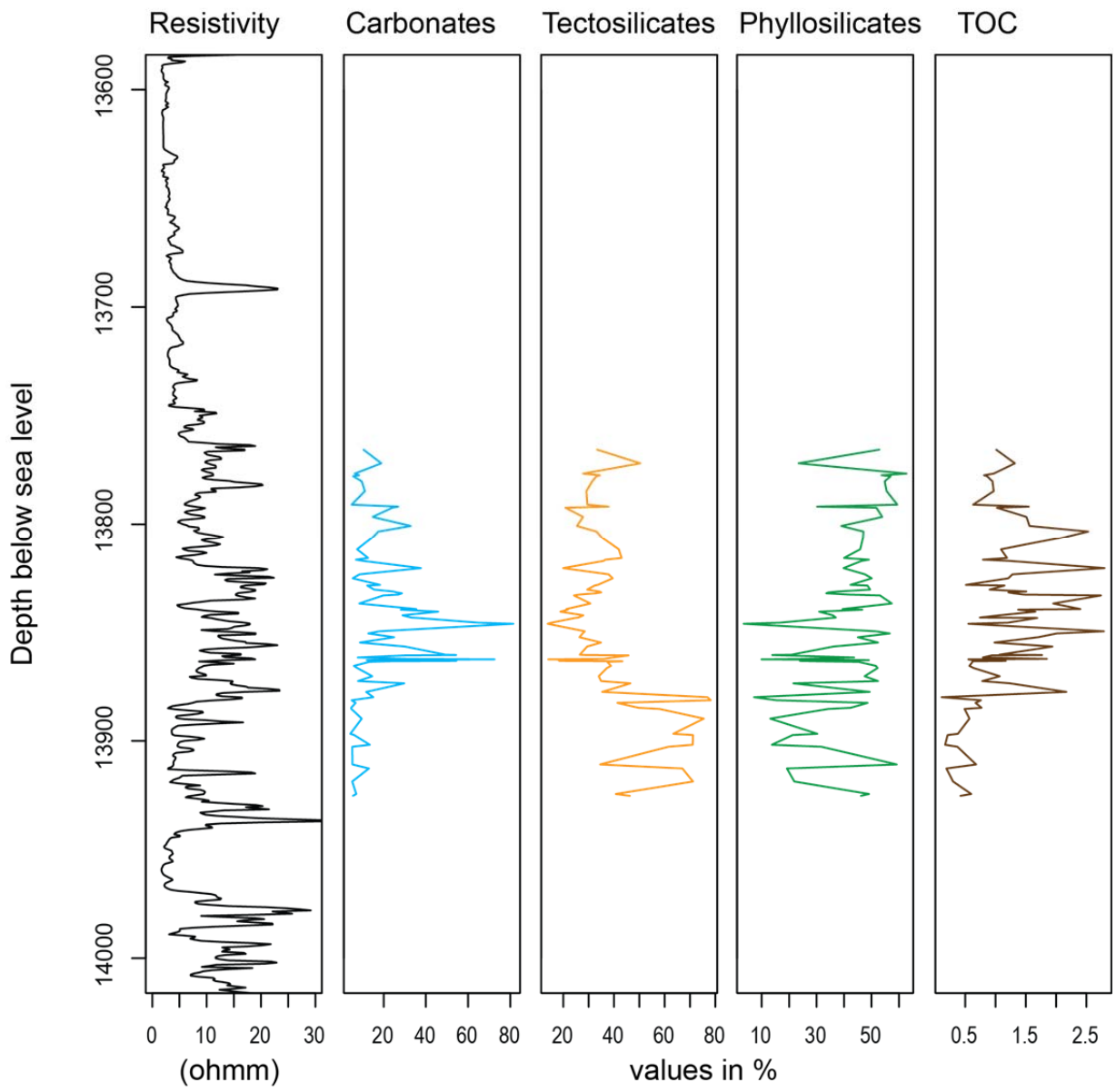

Figure 8: Bulk-Rock mineralogy data from the cored section of the Beech Grove 94H. Resistivity data included for reference.

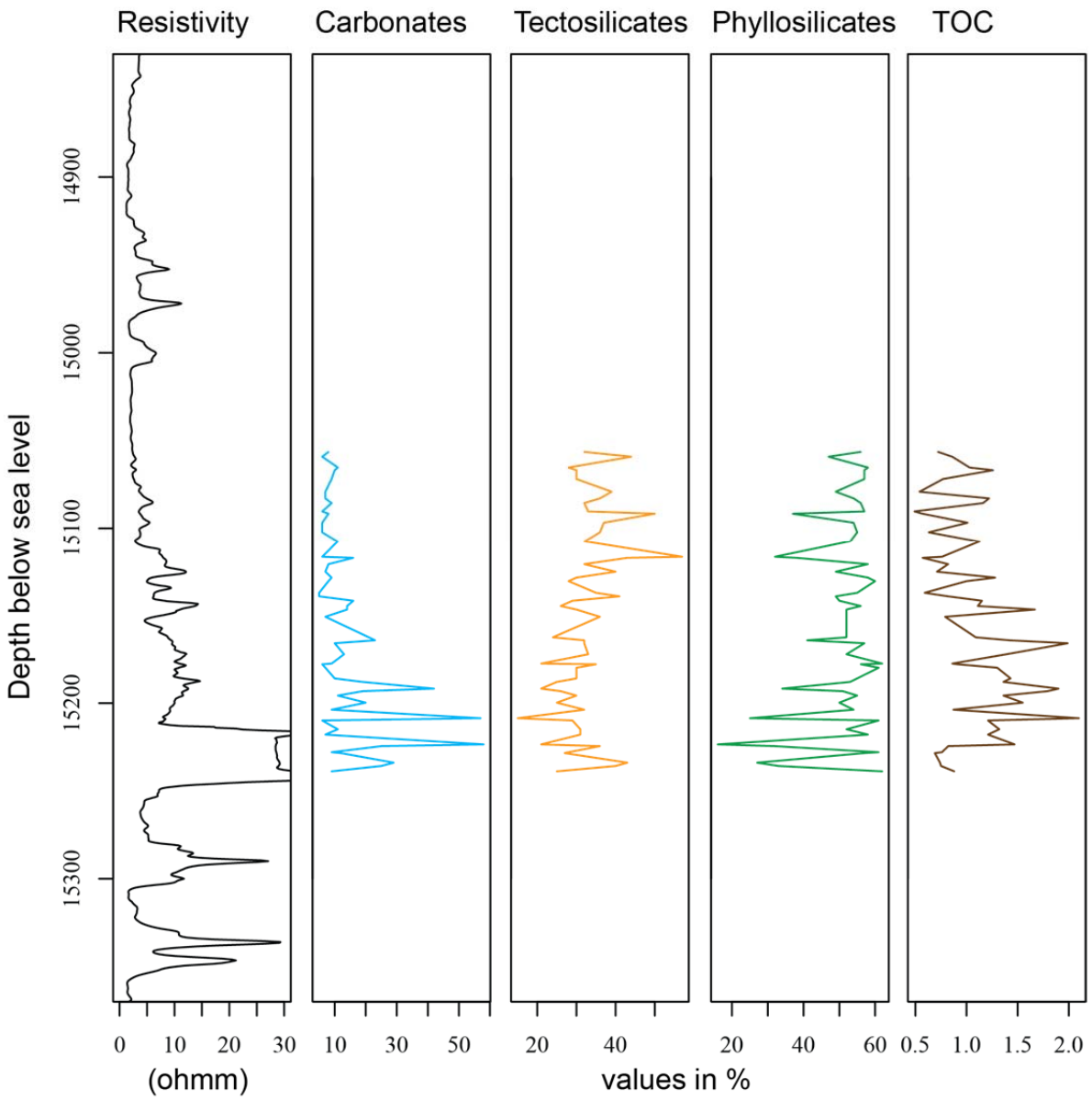

Figure 9: Bulk-Rock mineralogy data from the cored section of the Lane 64H. Resistivity data included for reference.

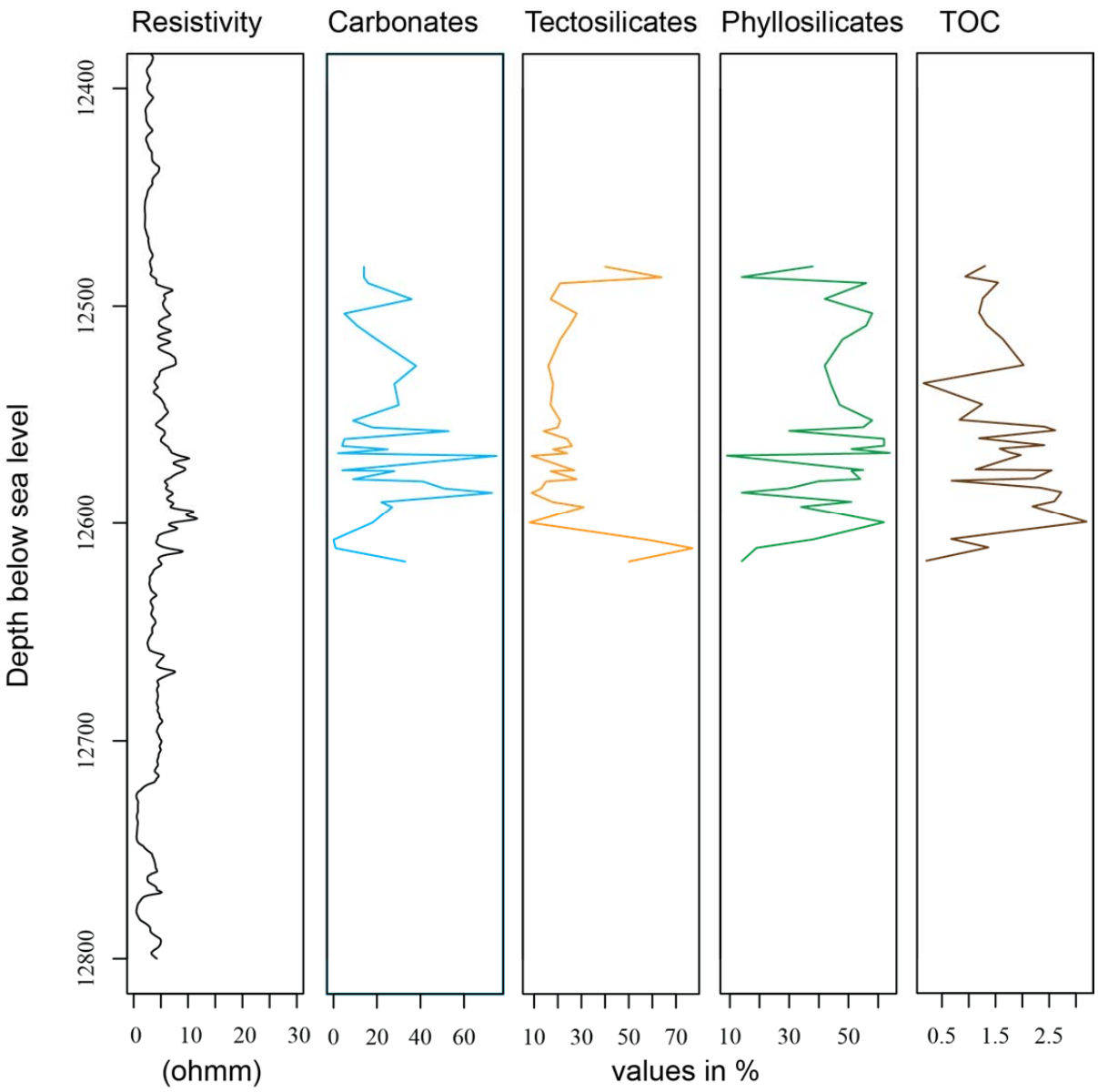

Figure 10: Bulk-Rock mineralogy data from the cored section of the Soterra 6H. Resistivity data included for reference.

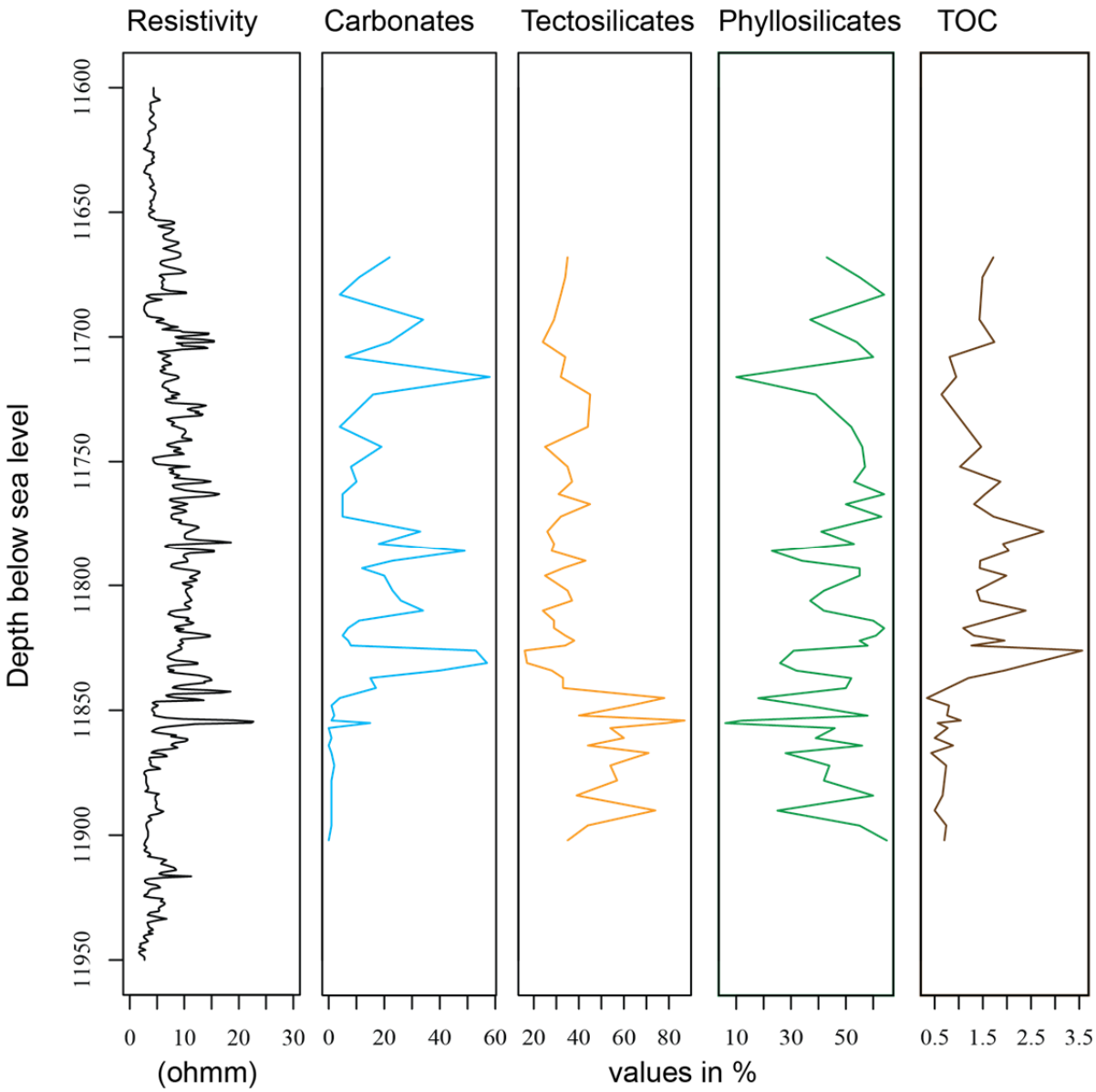

Figure 11: Bulk-Rock mineralogy data from the cored section of the Thomas 38H. Resistivity data included for reference.

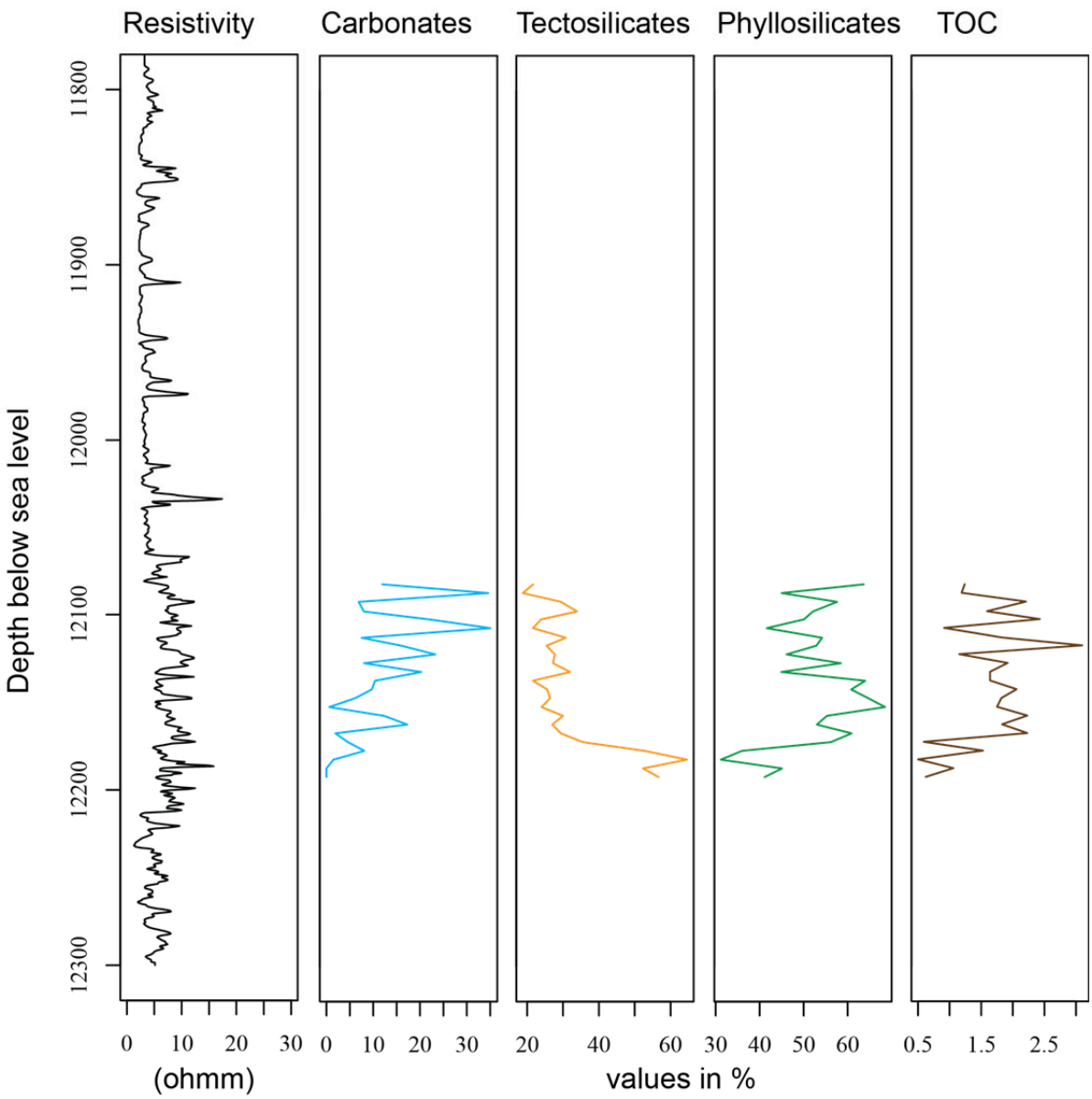

Figure 12: Bulk-Rock mineralogy data from the cored section of the Crosby 12-1H. Resistivity data included for reference.

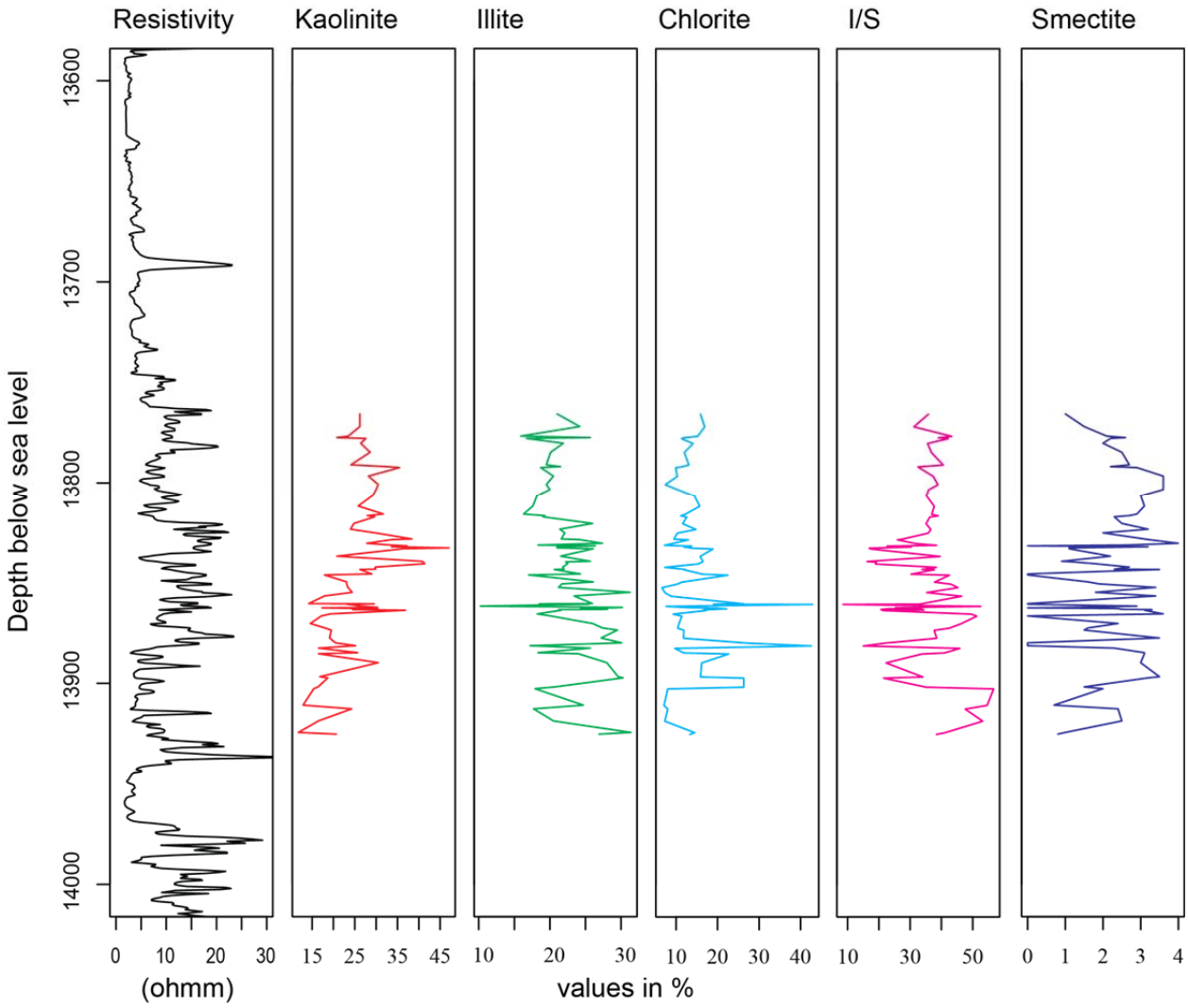

Figure 13: Clay mineralogy data from the cored section of the Beech Grove 94H. Resistivity data included for reference.

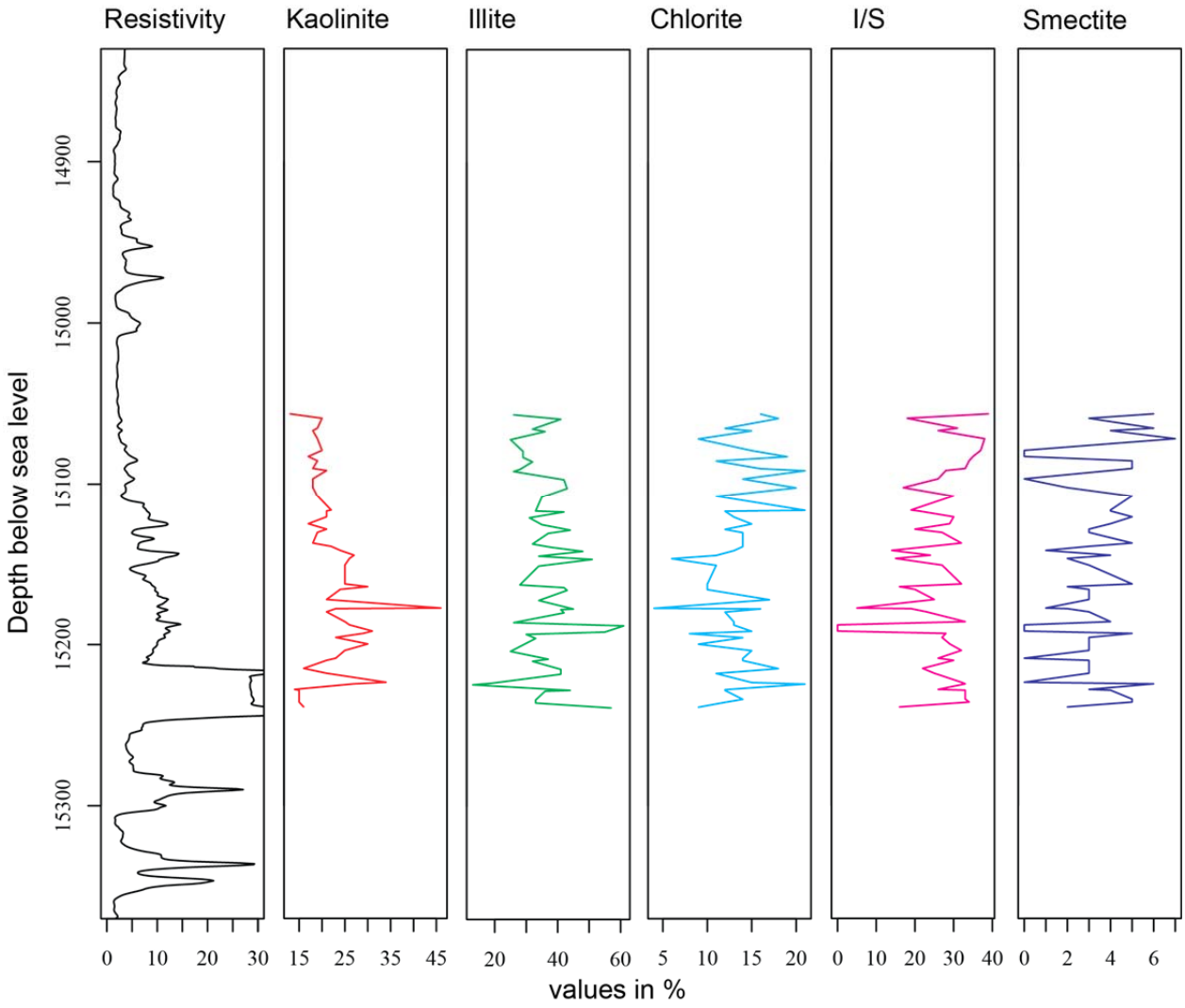

Figure 14: Clay mineralogy data from the cored section of the Lane 64H. Resistivity data included for reference.

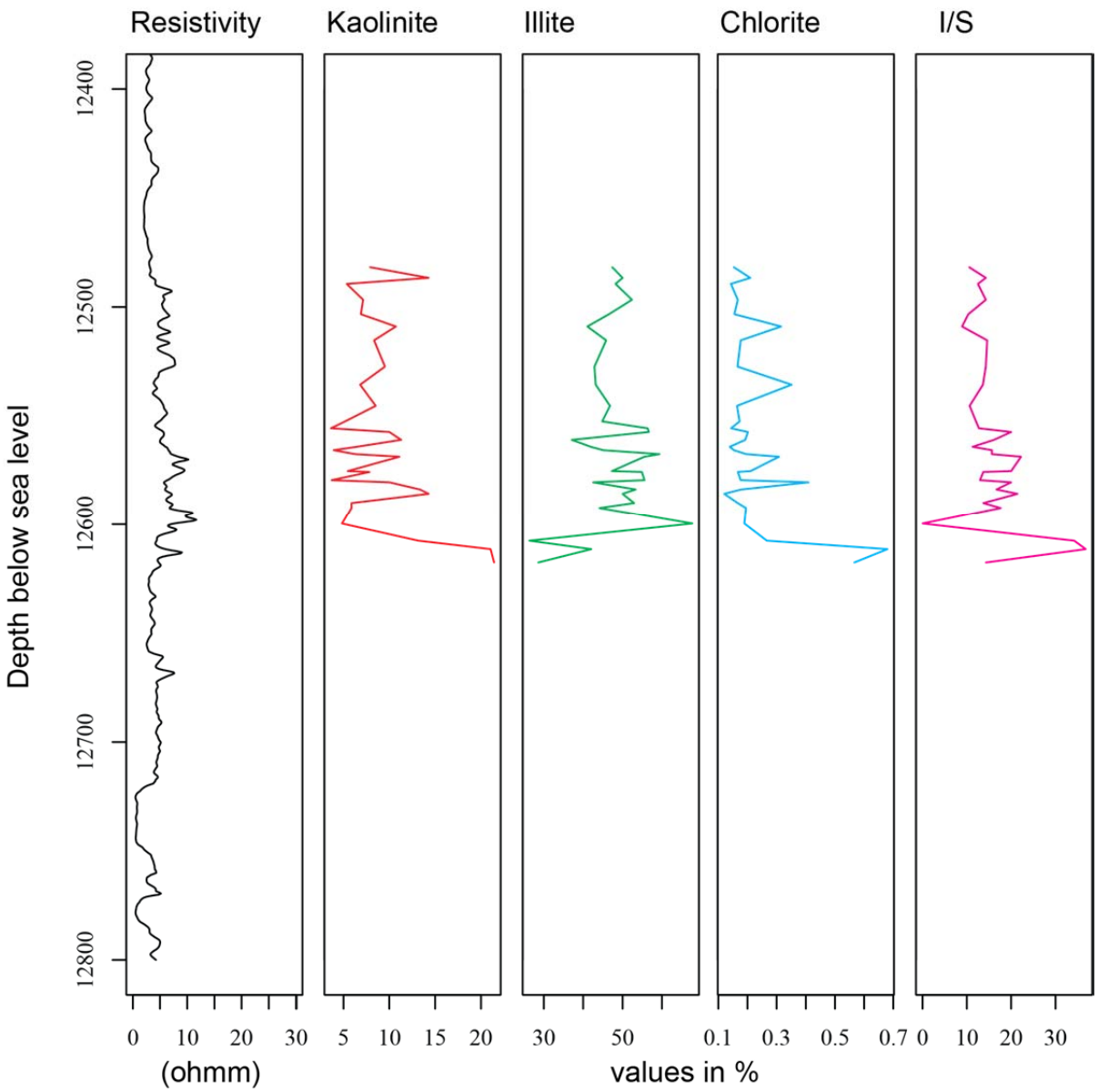

Figure 15: Clay mineralogy data from the cored section of the Soterra 6H. Resistivity data included for reference.

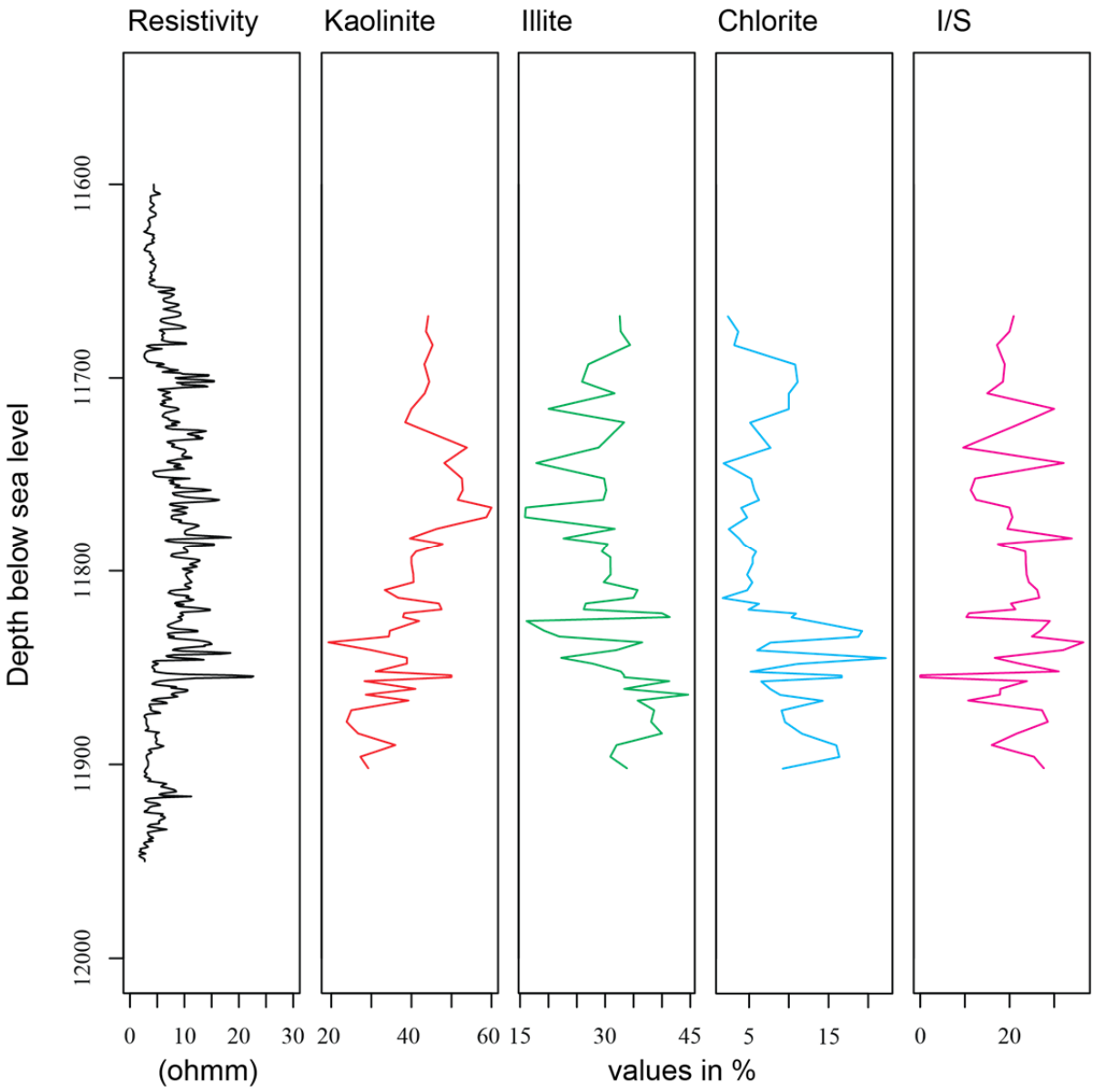

Figure 16: Clay mineralogy data from the cored section of the Thomas38H. Resistivity data included for reference

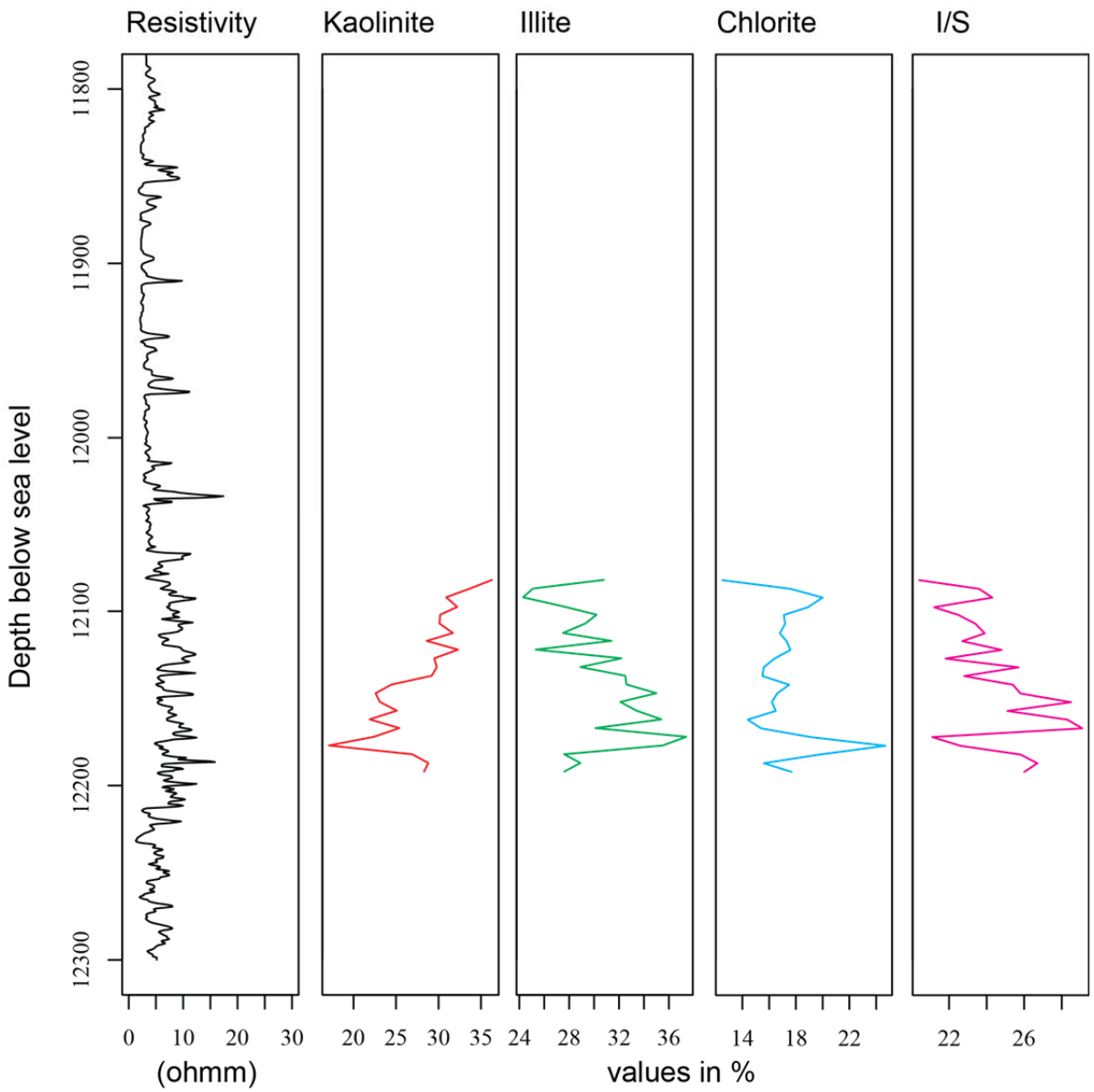

Figure 17: Clay mineralogy data from the cored section of the Crosby 12-1H. Resistivity data included for reference

SPECTRAL ANALYSIS

The orbital cycles used as targets for ASM calculations are displayed in Table 1. The detailed results of MTM and ASM are contained in Table 2. Graphic results for each well are displayed in Figures 18-27.

Orbital Cycle	Cretaceous Periodicity(ky)
Eccentricity (L)	404.18
Eccentricity(M)	123.82
Eccentricity(S)	94.78
Obliquity(L)	50.44
Obliquity(S)	38.94
Precession(L)	22.34
Precession(S)	18.54

Table 1: Target orbital cycles and associated Cretaceous periodicity used in this study (Berger et al., 1992).

Figures 28-32 show percent carbonate data for each well transformed from the depth dimension to the temporal dimension. Alongside the percent carbonate data in each figure are the significant frequencies as determined by MTM plotted both individually as well as convolved.

Well Name	Frequency (cycles/meter)	MTM Confidence (%)	Periodicity (ky)	Orbital Cycle
Beech Grove 94H				
	0.02871206	95.163	395.285	Eccentricity (L)
	0.3568499	95.064	31.805	Obliquity(S)
	0.4922067	94.698	23.058	Precession(L)
S(cm/ky)			8.811	
ASM			0.002	
H_0			0.336	
p-value			0.003	
Lane 64H				
	0.02138841	92.84067	393.853	Eccentricity(L)
	0.07485944	95.41009	112.529	Eccentricity(M)
S(cm/ky)			11.871	
ASM			1.016×10^{-4}	
H_0			0.66	
p-value			0.0066	
Thomas 38H				
	0.03048078	96.61401	394.132	Eccentricity(L)
	0.14409094	91.09695	83.374	Eccentricity(S)
	0.23276229	90.71543	51.613	Obliquity(L)
	0.3131207	93.27786	38.367	Obliquity(S)
S(cm/ky)			8.324	
ASM			2.162×10^{-4}	
H_0			0.055	
p-value			5.5×10^{-4}	
Soterra 6H				
	0.06213712	99.22635	130.618	Eccentricity(M)
	0.1433934	93.51307	56.601	Obliquity(L)
	0.21986981	94.05436	36.914	Obliquity(S)
S(cm/ky)			12.321	
ASM			2.256×10^{-4}	
H_0			0.533	
p-value			0.005	
Crosby12-1H				
	0.179733	92.10837	52.154 (?)	Obliquity(L)
S(cm/ky)			10.668 (?)	
ASM			0	
H_0			9.475	
p-value			0.09475	

Table 2: Detailed tabular results from MTM and ASM analysis. Periodicities were determined using the optimal sedimentation rate from ASM.

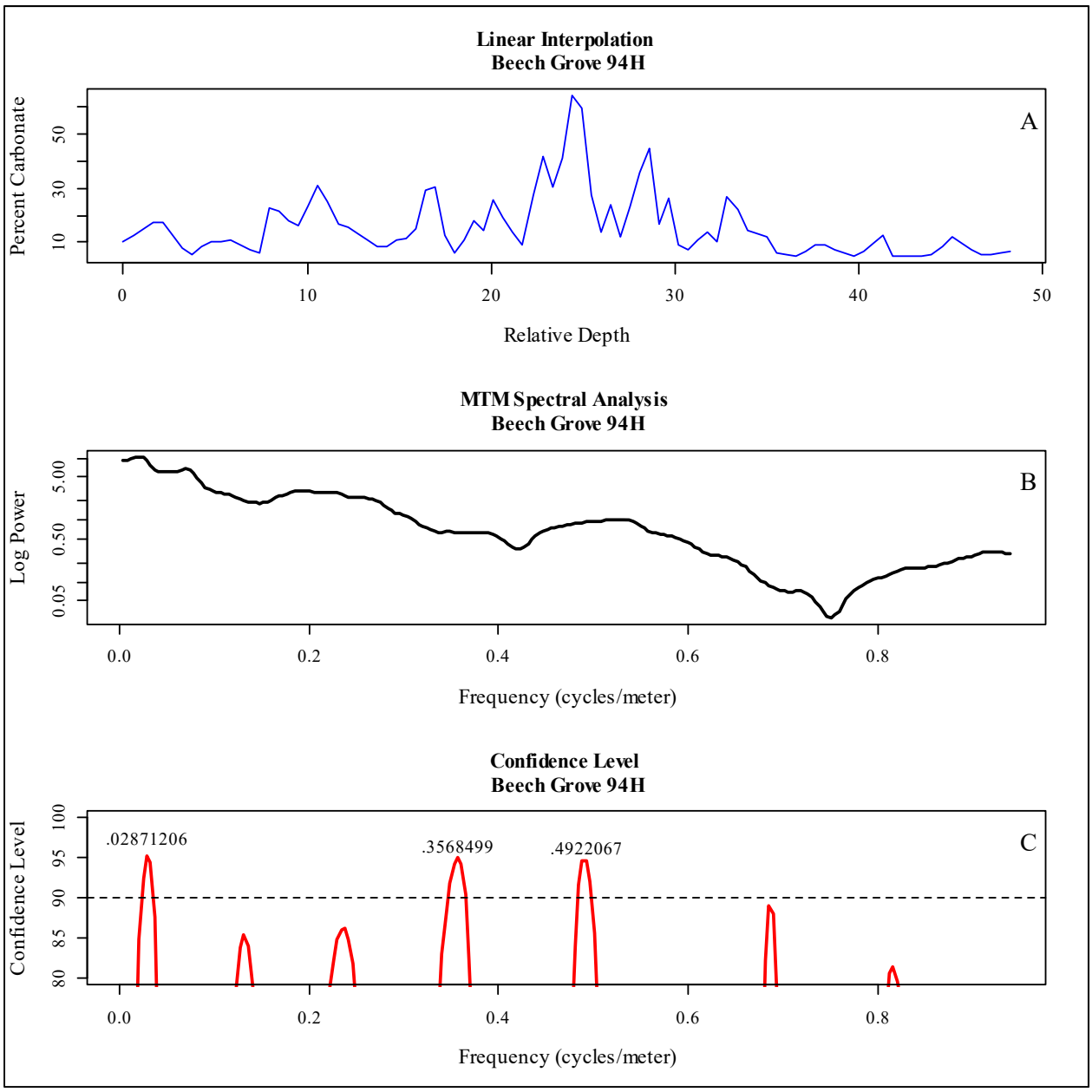

Figure 18: Graphical MTM spectral analysis from the Beech Grove 94H well. (A) Linear interpolation of raw percent carbonate data. Data interpolated at the median sampling interval. (B) Three-taper 2π MTM spectral results plotted in log-space. (C) F-test confidence results. Dotted lined represents the 90% confidence level threshold.

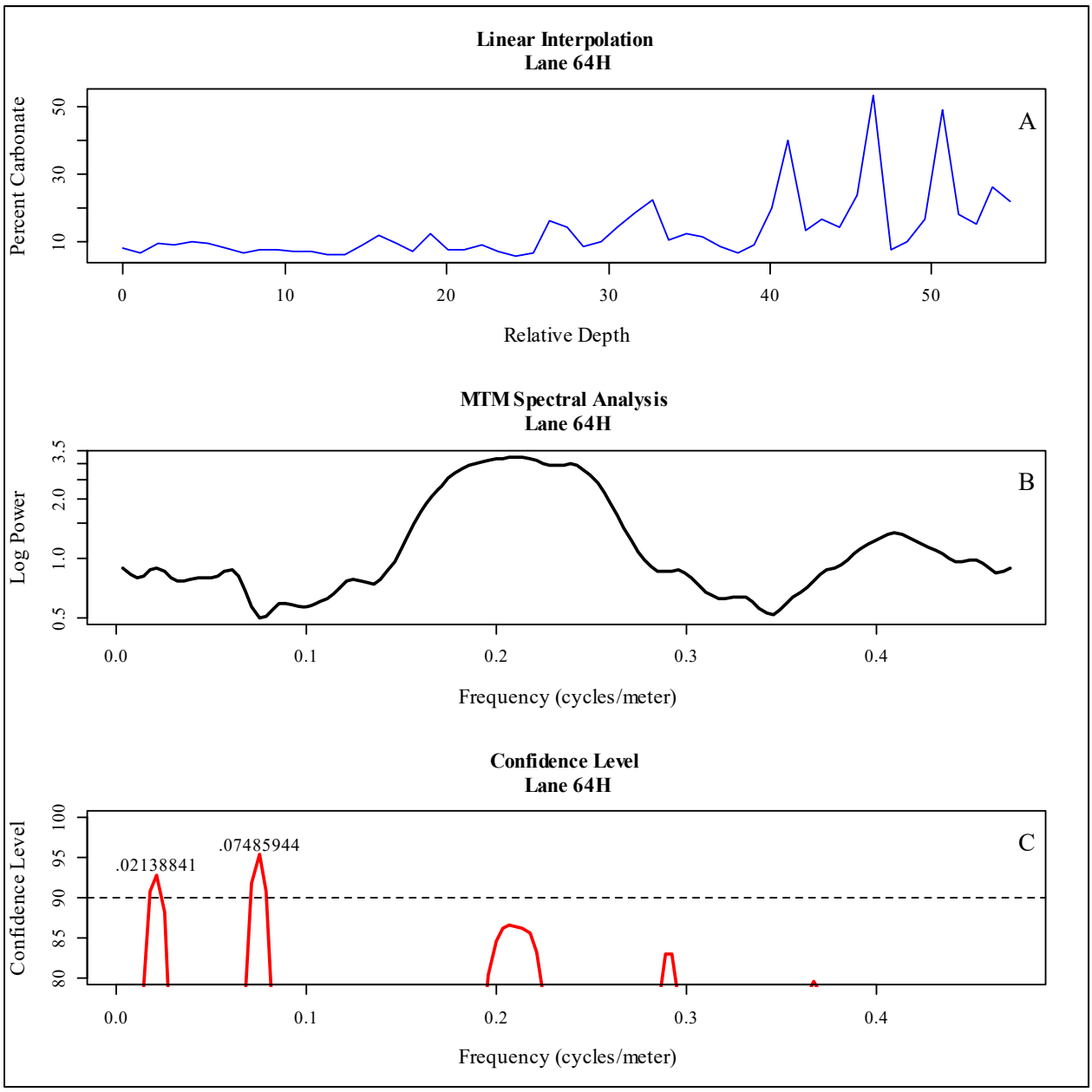

Figure 19: Graphical MTM spectral analysis from the Lane 64H well. (A) Linear interpolation of raw percent carbonate data. Data interpolated at the median sampling interval. (B) Three-taper 2π MTM spectral results plotted in log-space. (C) F-test confidence results. Dotted lined represents the 90% confidence level threshold.

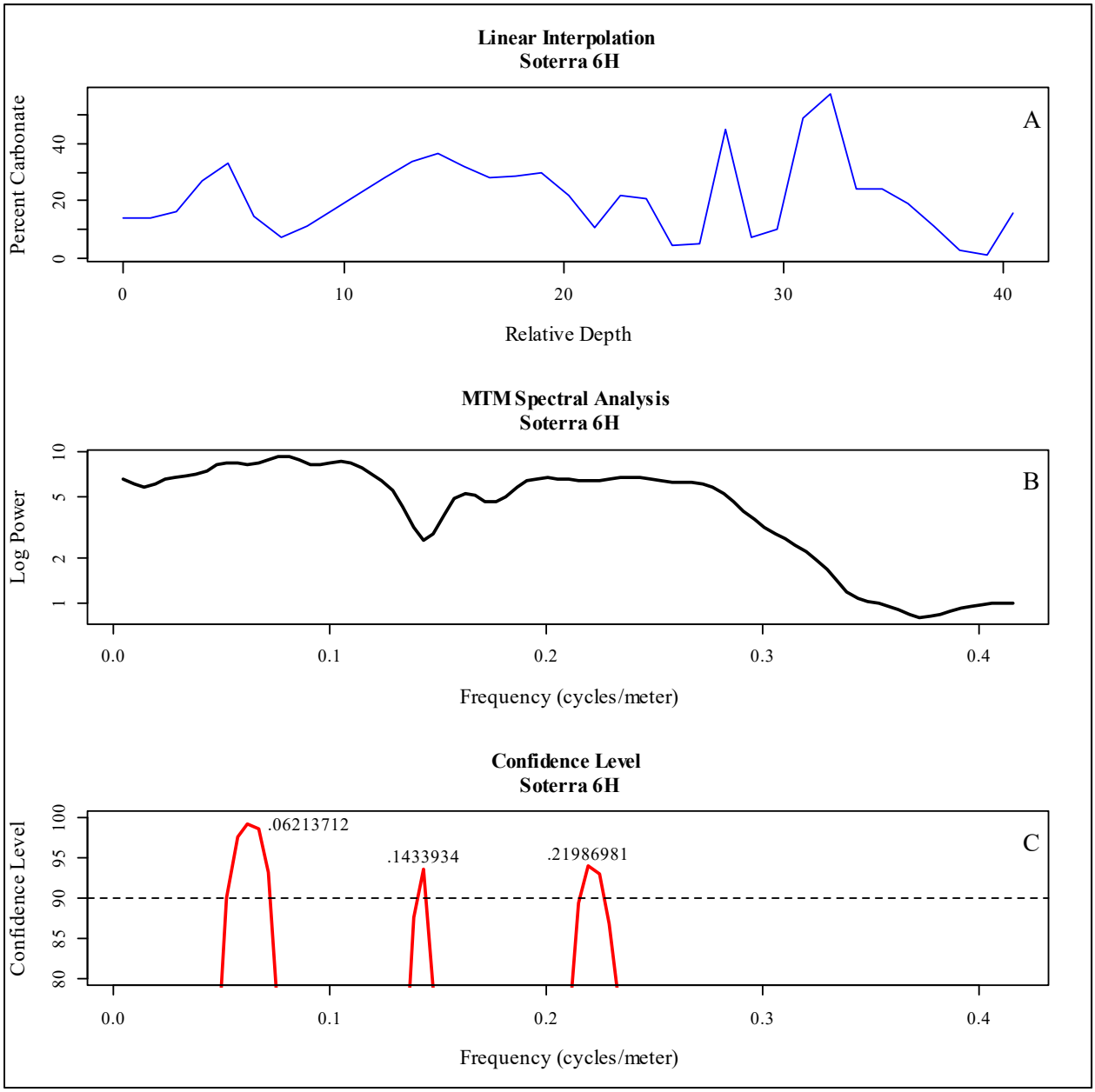

Figure 20: Graphical MTM spectral analysis from the Soterra 6H well. (A) Linear interpolation of raw percent carbonate data. Data interpolated at the median sampling interval. (B) Three-taper 2π MTM spectral results plotted in log-space. (C) F-test confidence results. Dotted lined represents the 90% confidence level threshold.

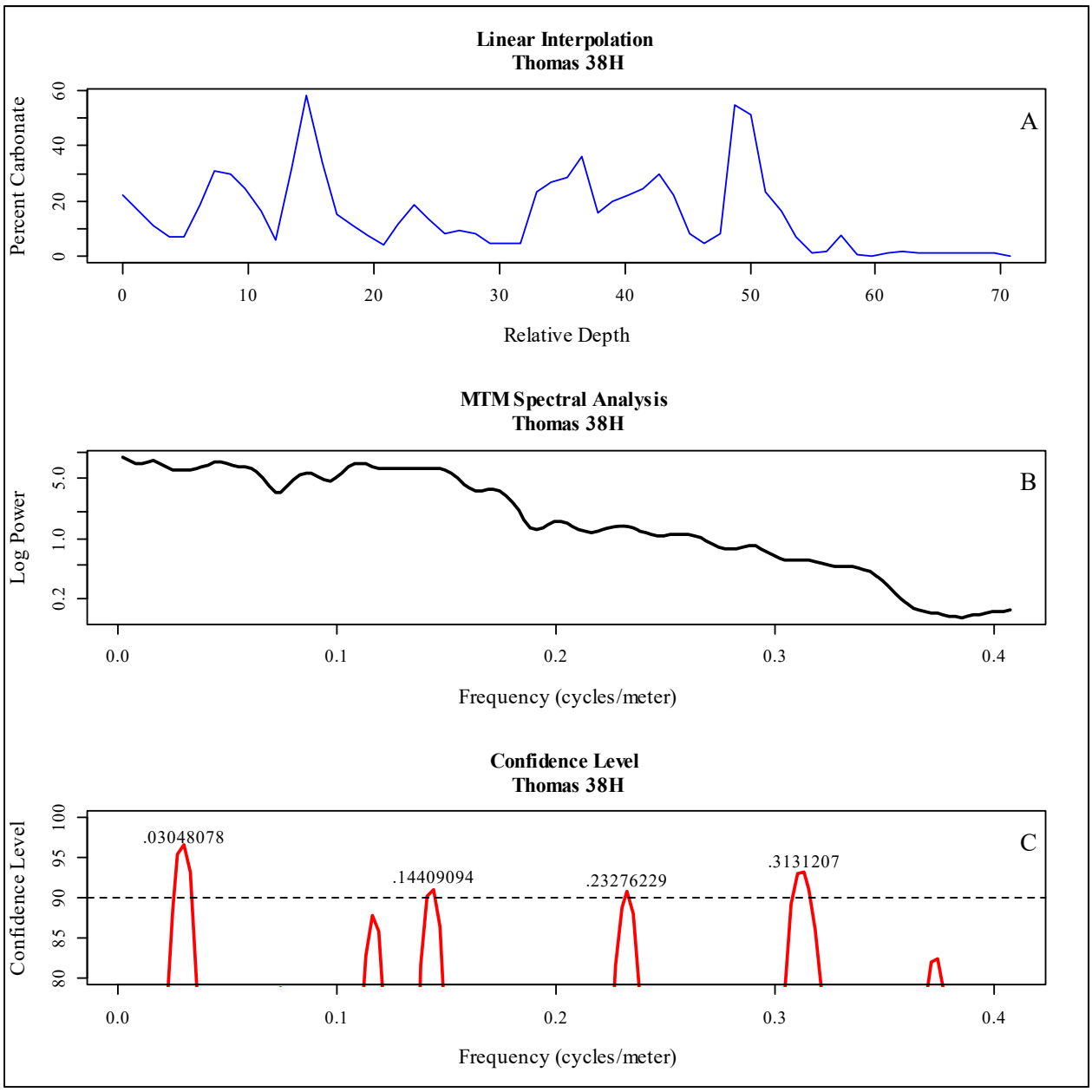

Figure 21: Graphical MTM spectral analysis from the Thomas 38H well. (A) Linear interpolation of raw percent carbonate data. Data interpolated at the median sampling interval. (B) Three-taper 2π MTM spectral results plotted in log-space. (C) F-test confidence results. Dotted lined represents the 90% confidence level threshold.

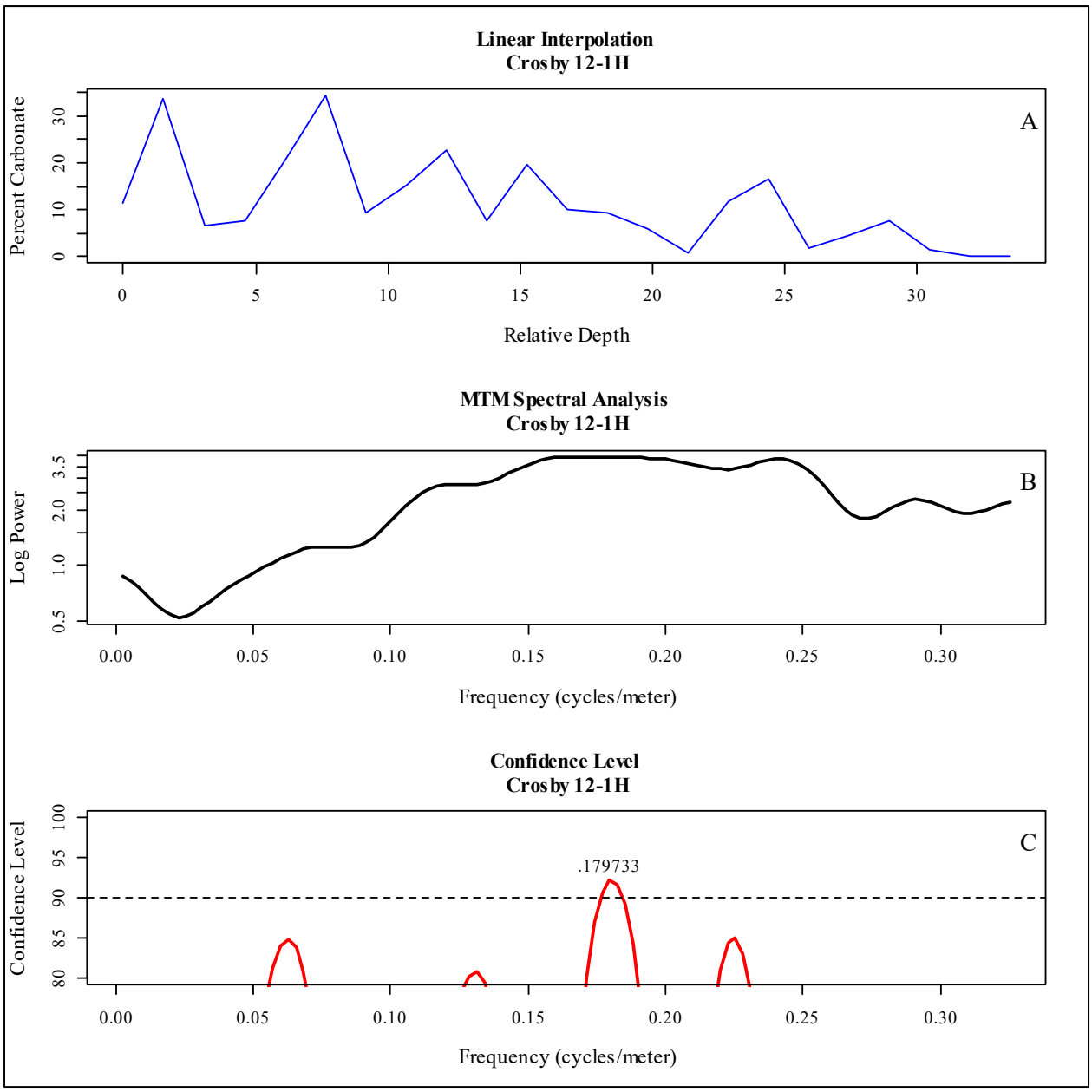

Figure 22: Graphical MTM spectral analysis from the Crosby 12-1H well. (A) Linear interpolation of raw percent carbonate data. Data interpolated at the median sampling interval. (B) Three-taper 2π MTM spectral results plotted in log-space. (C) F-test confidence results. Dotted lined represents the 90% confidence level threshold.

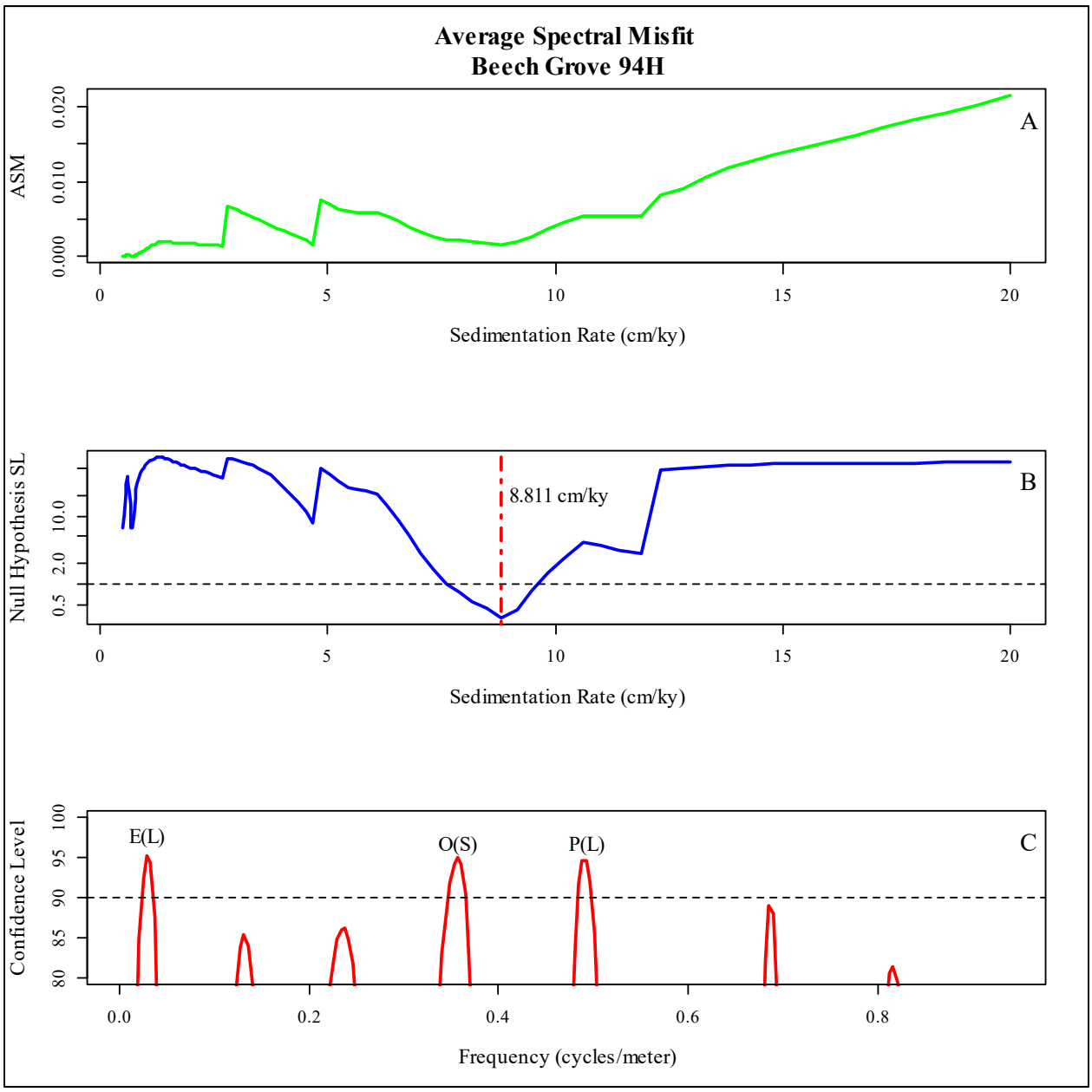

Figure 23: Spectral misfit analysis from the Beech Grove 94H well. (A) Average spectral misfit metric calculated at sedimentation rates between 0.5 cm/ky and 20 cm/ky. (B) Null hypothesis significance levels based on a Monte Carlo simulation using 100,000 random spectra. Dashed line represents critical significance threshold. Red dot-dashed line located at optimal sedimentation rate. (C) MTM F-test confidence results. Significant frequencies are labeled with corresponding orbital cycles based on the optimal sedimentation rate from ASM analysis. Dotted lined represents the 90% confidence level threshold.

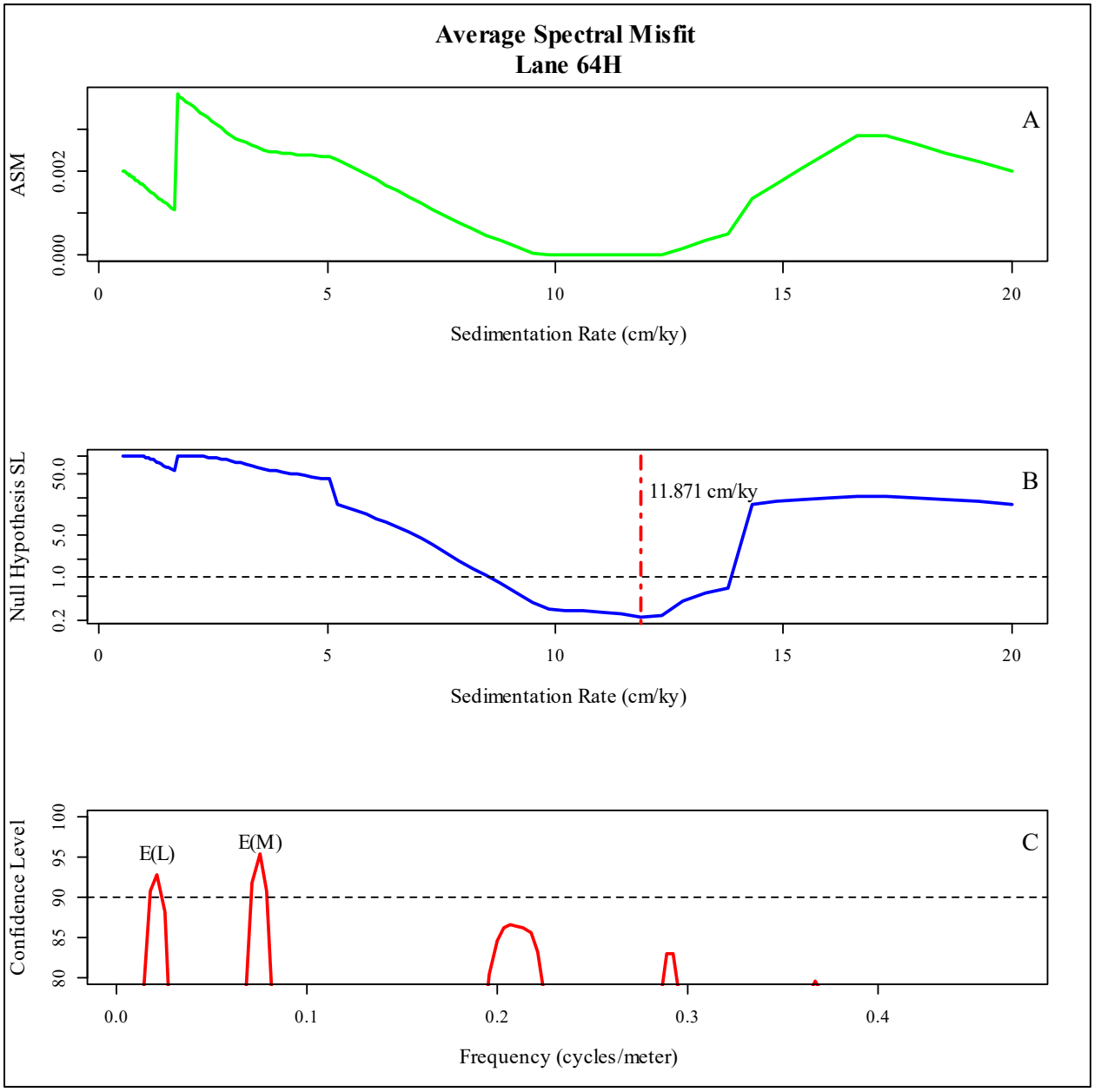

Figure 24: Spectral misfit analysis from the Lane 64H well. (A) Average spectral misfit metric calculated at sedimentation rates between 0.5 cm/ky and 20 cm/ky. (B) Null hypothesis significance levels based on a Monte Carlo simulation using 100,000 random spectra. Dashed line represents critical significance threshold. Red dot-dashed line located at optimal sedimentation rate. (C) MTM F-test confidence results. Significant frequencies are labeled with corresponding orbital cycles based on the optimal sedimentation rate from ASM analysis. Dotted lined represents the 90% confidence level threshold.

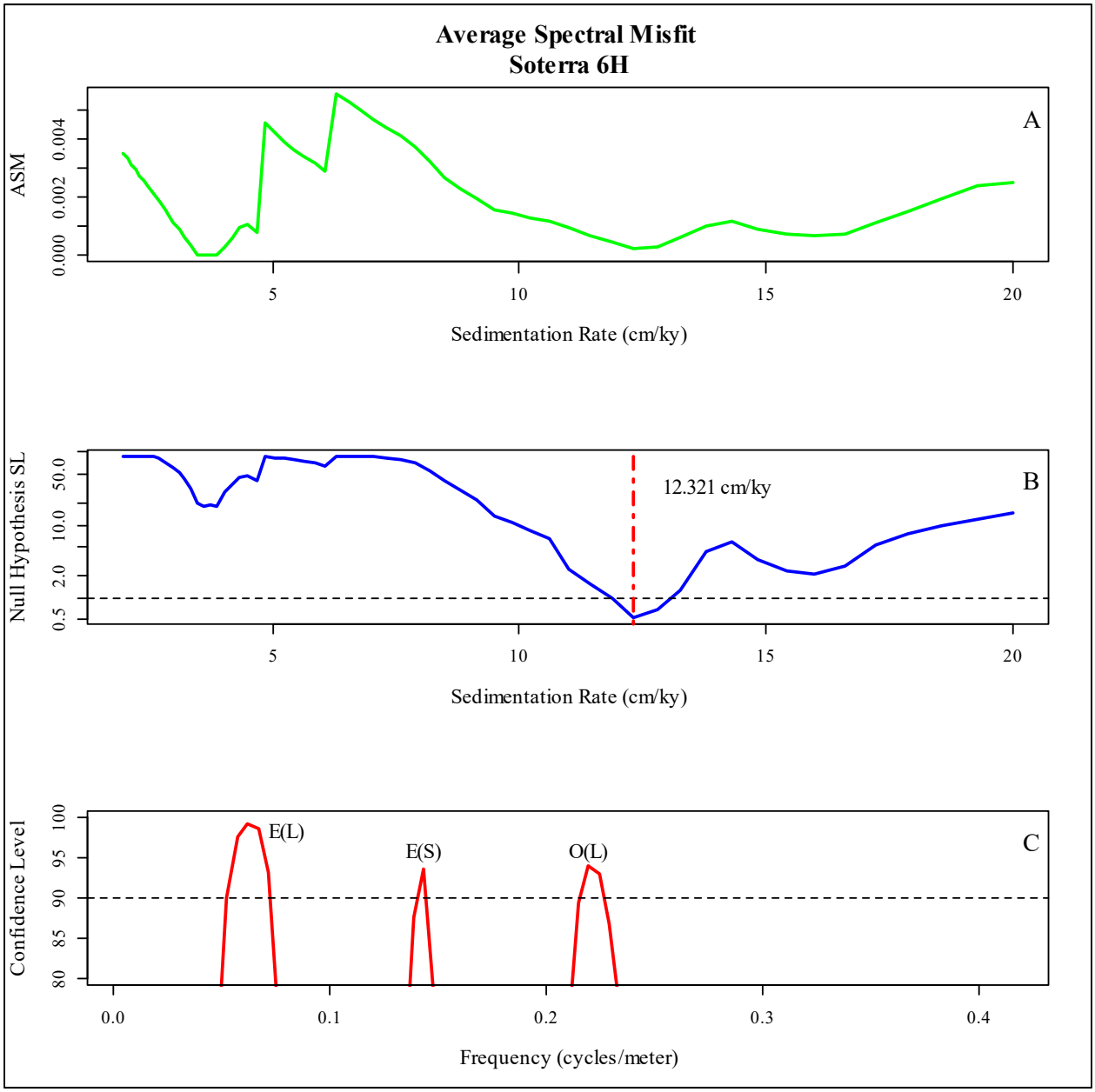

Figure 25: Spectral misfit analysis from the Soterra 6H well. (A) Average spectral misfit metric calculated at sedimentation rates between 0.5 cm/ky and 20 cm/ky. (B) Null hypothesis significance levels based on a Monte Carlo simulation using 100,000 random spectra. Dashed line represents critical significance threshold. Red dot-dashed line located at optimal sedimentation rate. (C) MTM F-test confidence results. Significant frequencies are labeled with corresponding orbital cycles based on the optimal sedimentation rate from ASM analysis. Dotted lined represents the 90% confidence level threshold.

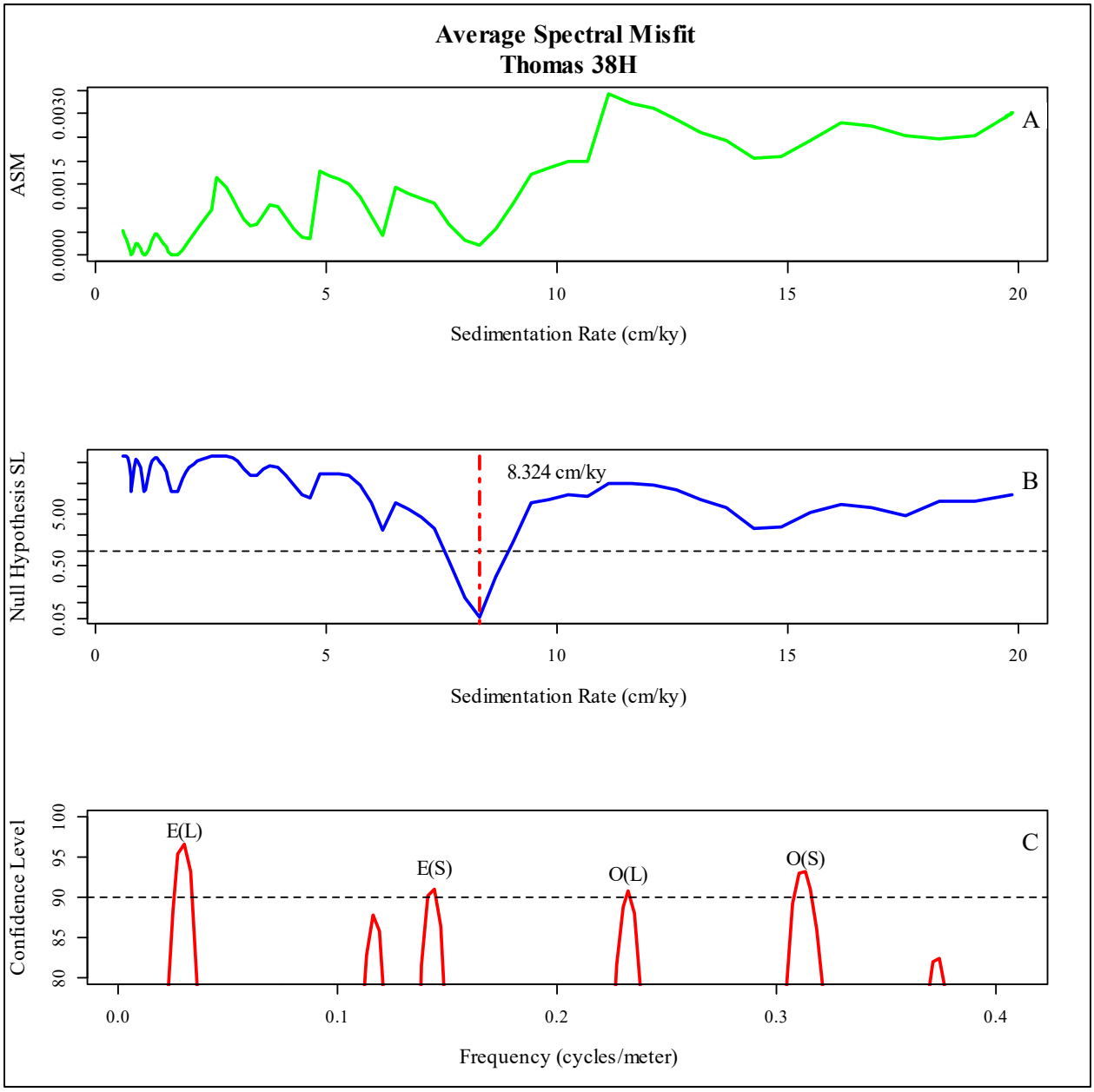

Figure 26: Spectral misfit analysis from the Thomas 38H well. (A) Average spectral misfit metric calculated at sedimentation rates between 0.5 cm/ky and 20 cm/ky. (B) Null hypothesis significance levels based on a Monte Carlo simulation using 100,000 random spectra. Dashed line represents critical significance threshold. Red dot-dashed line located at optimal sedimentation rate. (C) MTM F-test confidence results. Significant frequencies are labeled with corresponding orbital cycles based on the optimal sedimentation rate from ASM analysis. Dotted lined represents the 90% confidence level threshold.

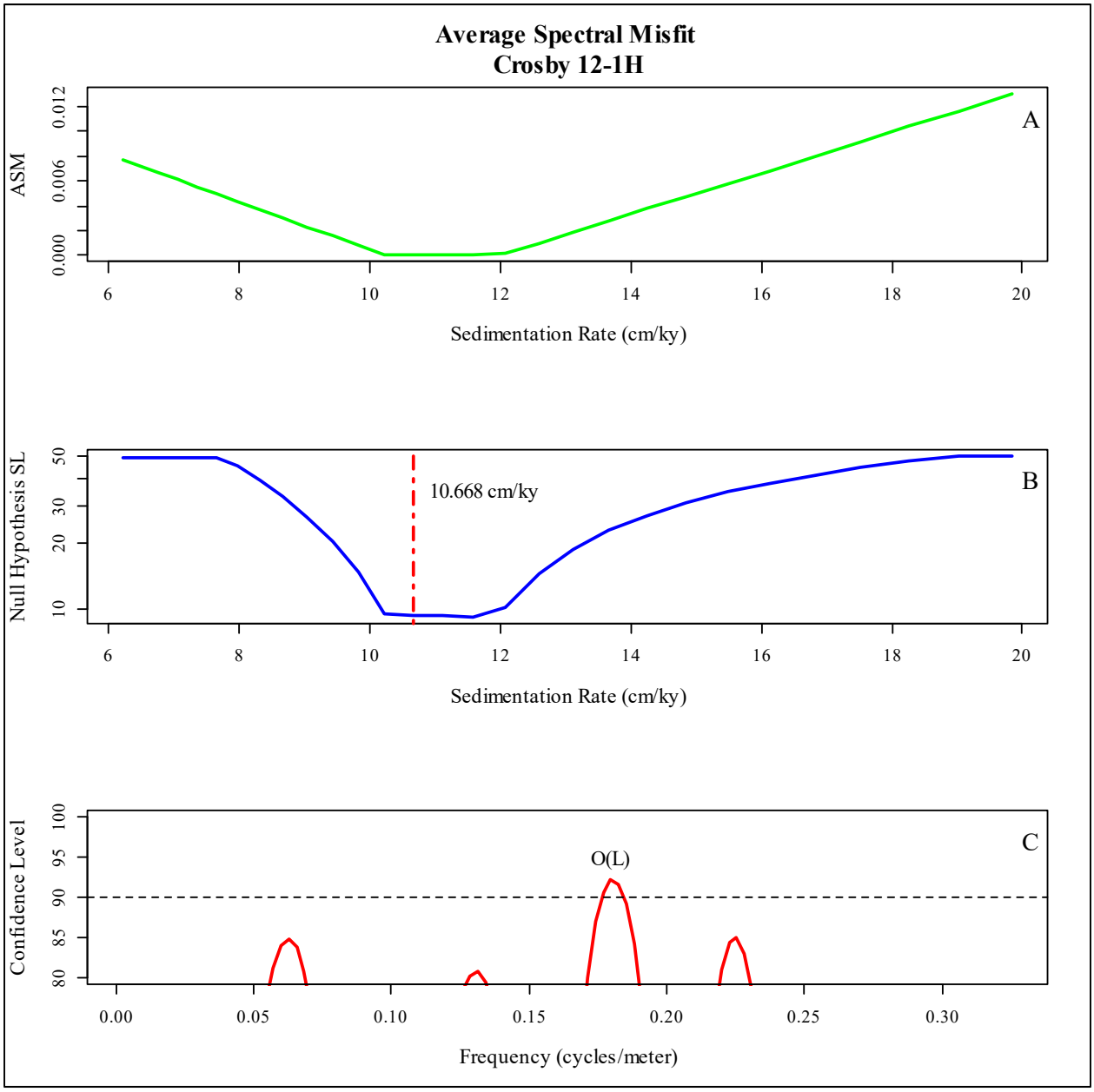

Figure 27: Spectral misfit analysis from the Crosby 12-1H well. (A) Average spectral misfit metric calculated at sedimentation rates between 0.5 cm/ky and 20 cm/ky. (B) Null hypothesis significance levels based on a Monte Carlo simulation using 100,000 random spectra. Dashed line represents critical significance threshold. Red dot-dashed line located at optimal sedimentation rate. (C) MTM F-test confidence results. Significant frequencies are labeled with corresponding orbital cycles based on the optimal sedimentation rate from ASM analysis. Dotted lined represents the 90% confidence level threshold.

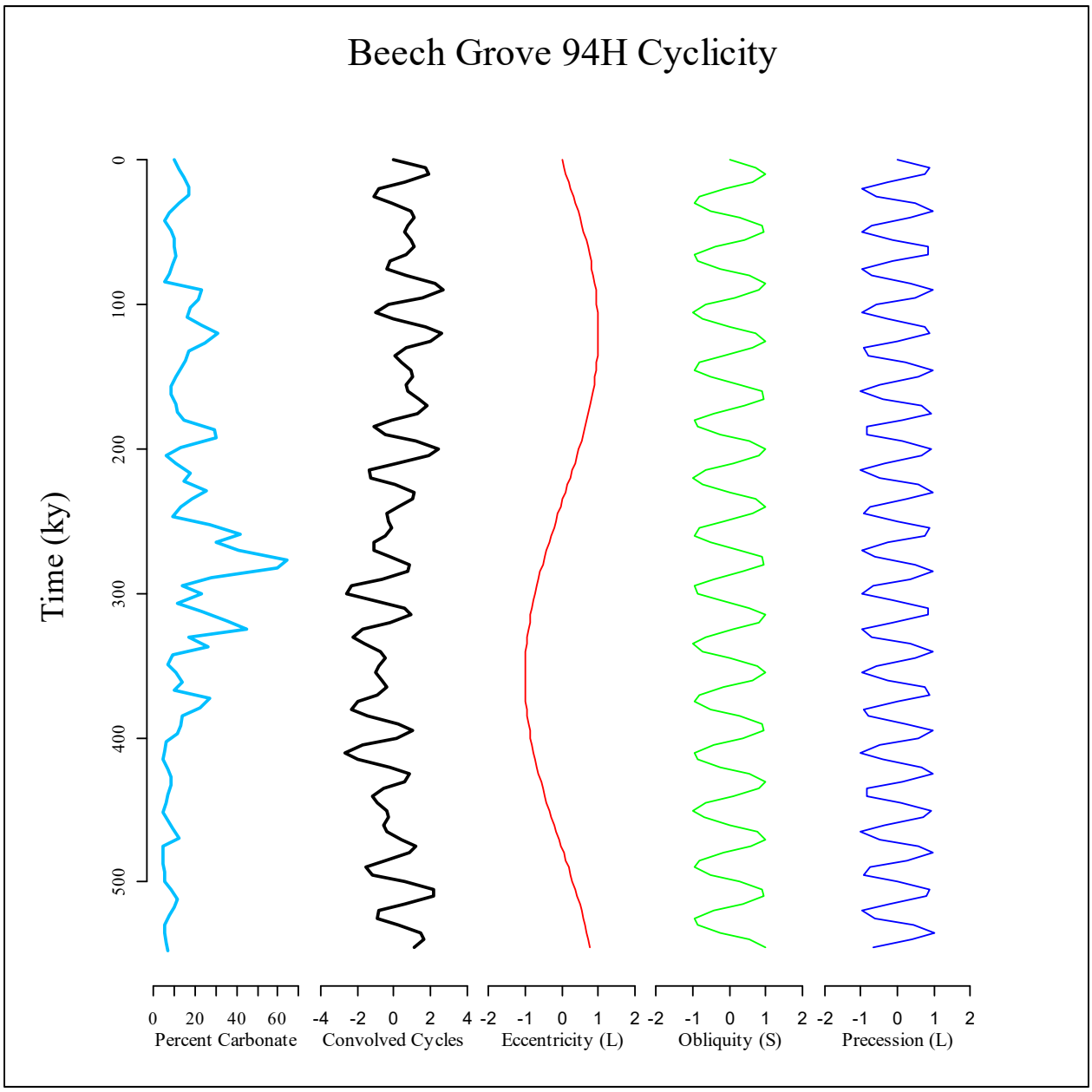

Figure 28: Comparison of significant frequencies to percent carbonate in the Beech Grove 94H well. Significant frequencies are labeled according to their corresponding orbital cycle.

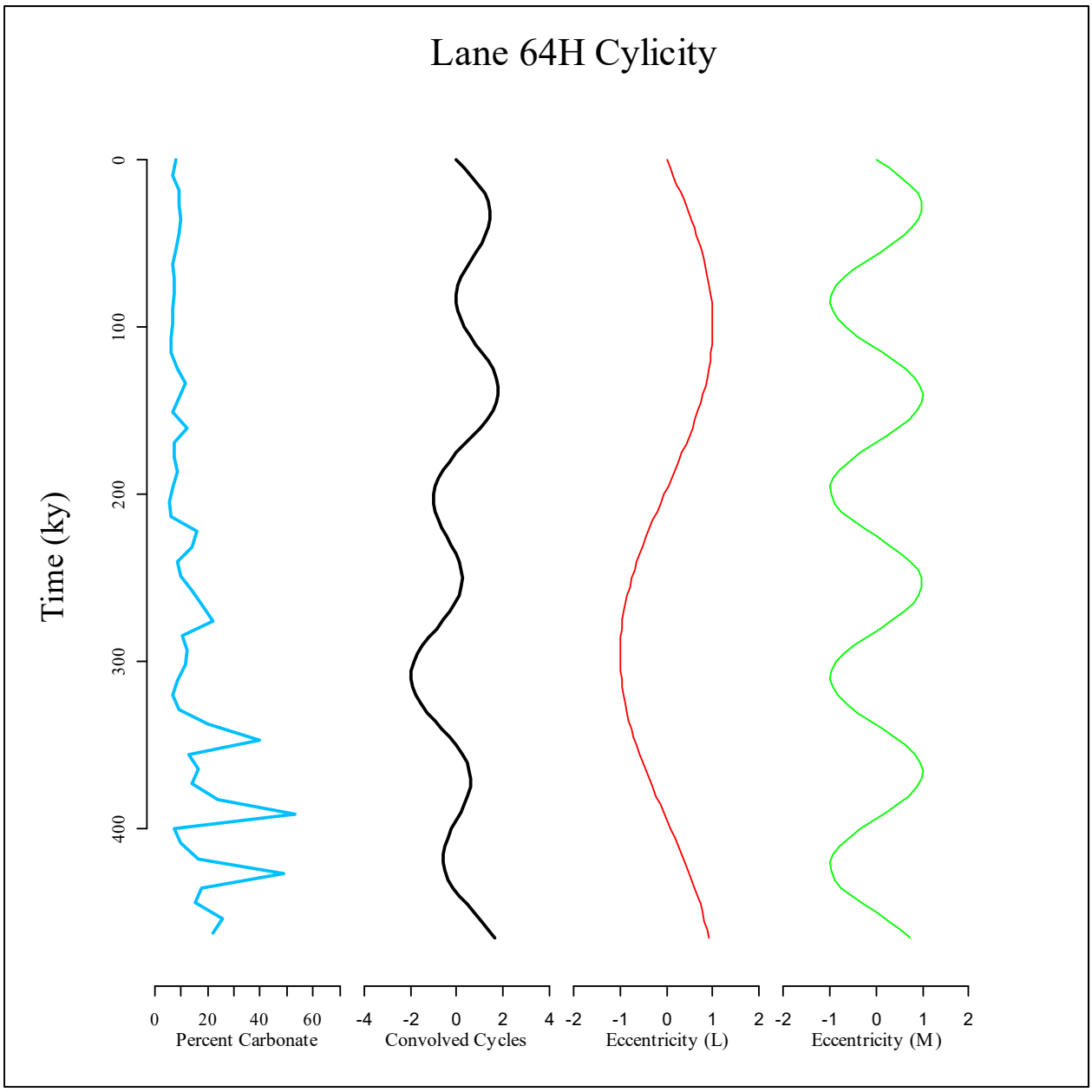

Figure 29: Comparison of significant frequencies to percent carbonate in the Lane 64H well. Significant frequencies are labeled according to their corresponding orbital cycle.

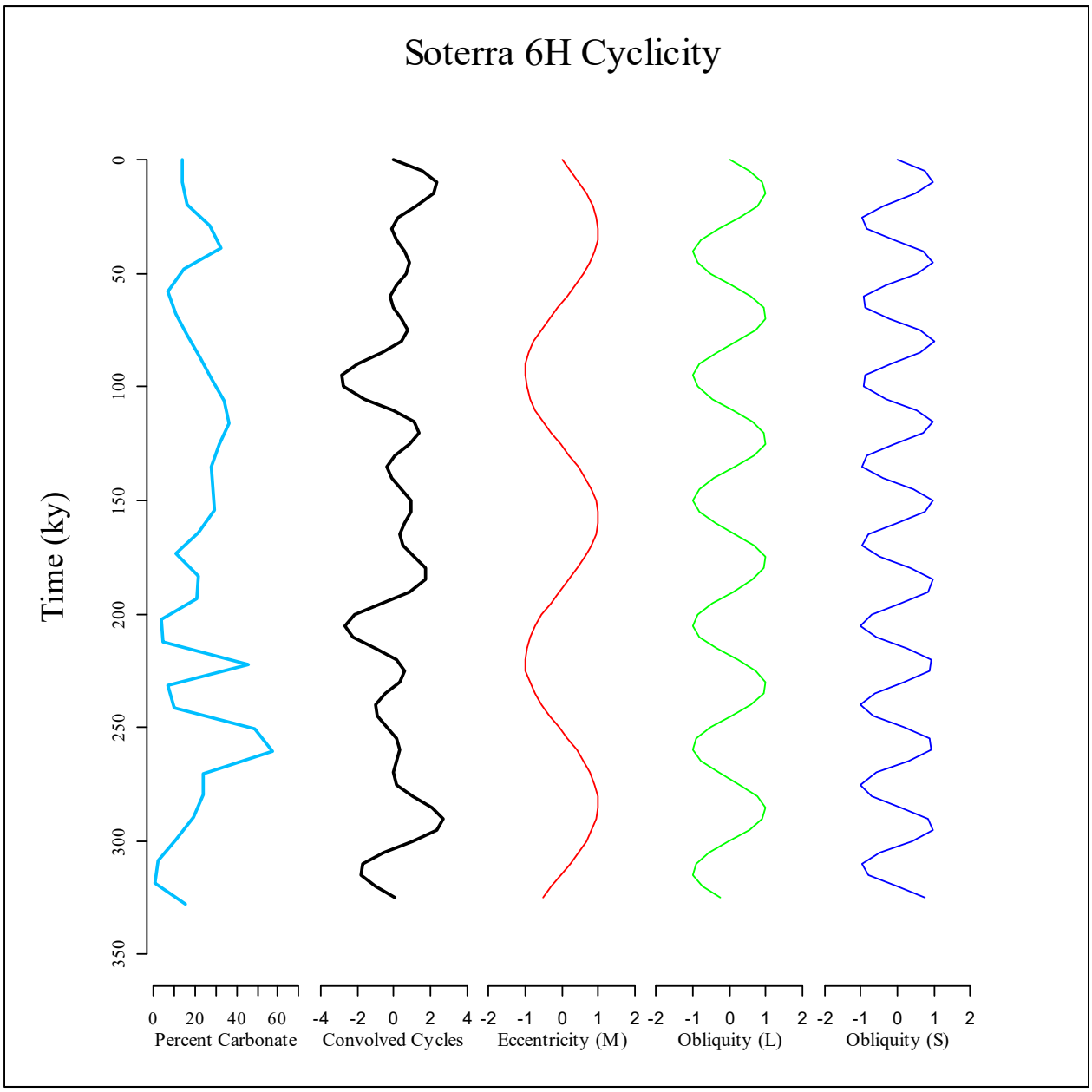

Figure 30: Comparison of significant frequencies to percent carbonate in the Soterra 6H well. Significant frequencies are labeled according to their corresponding orbital cycle.

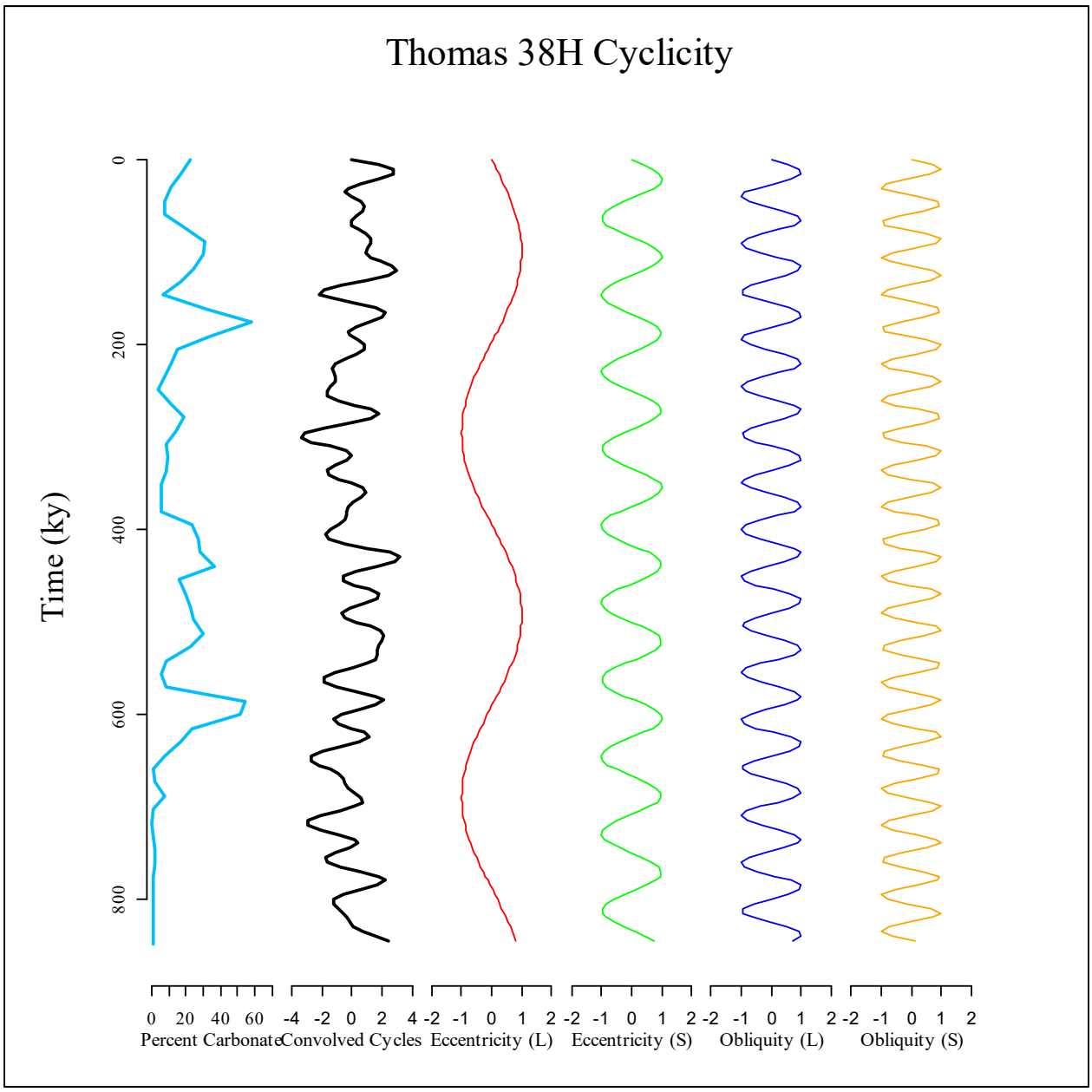

Figure 31: Comparison of significant frequencies to percent carbonate in the Thomas 38H well. Significant frequencies are labeled according to their corresponding orbital cycle.

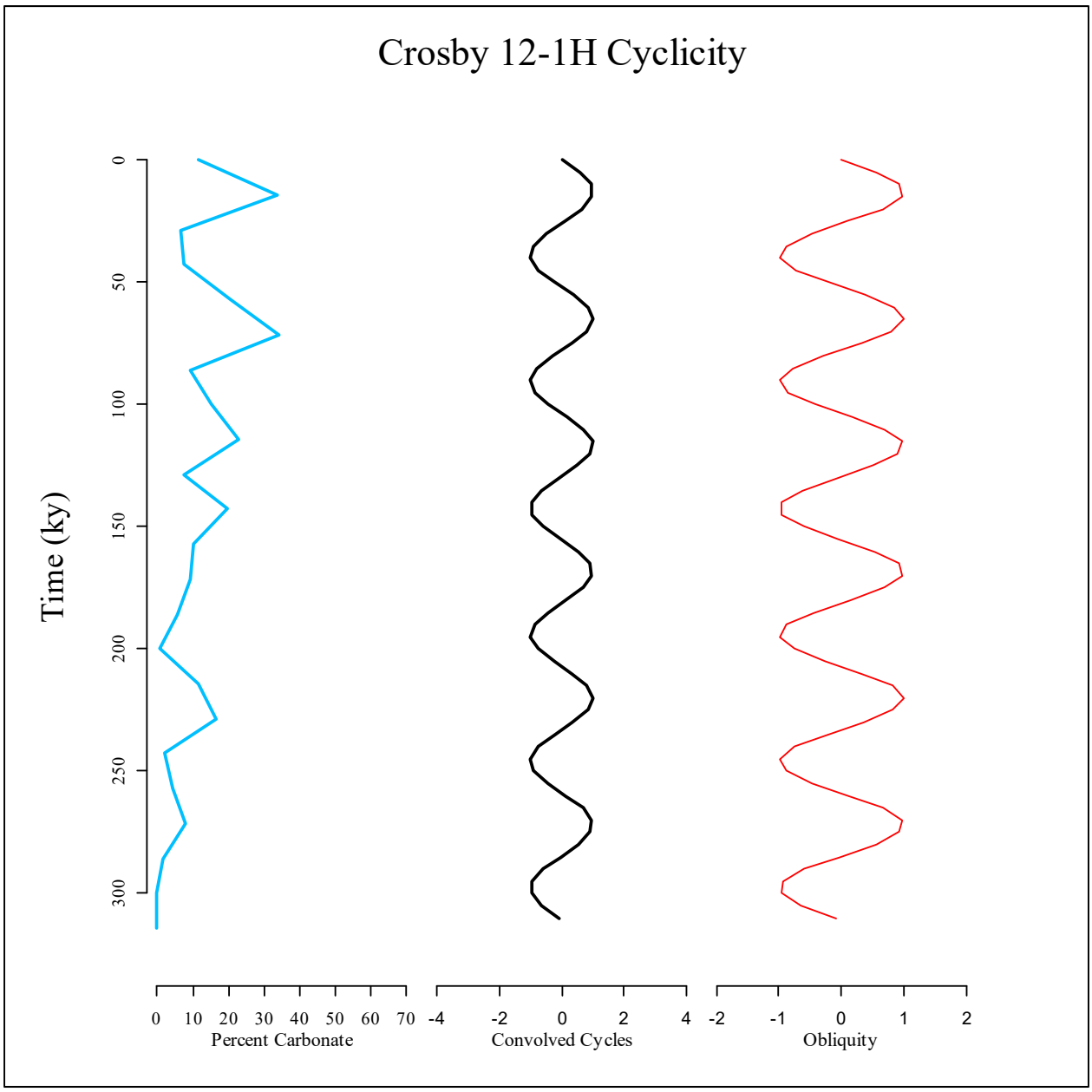

Figure 32: Comparison of significant frequencies to percent carbonate in the Crosby 12-1 well. Significant frequencies are labeled according to their corresponding orbital cycle.

VI. DISCUSSION

ORBITAL CYCLES, SEDIMENTATION RATES, AND OAE 2

MTM spectral density estimates reveal multiple statistically significant frequencies in carbonate content data in four out of the five studied wells. The Crosby 12-1H well is the exception. The carbonate data from the Crosby 12-1H contained only one statistically significant frequency. This is attributed to the relatively short coring interval and inconsistent sampling intervals. A sedimentation rate of 10.668 cm/ky is cautiously assigned to this well based on similar frequencies identified in other wells. However, because fewer than two significant frequencies were identified, the ASM results were insignificant, and the Crosby 12-1H is removed from further interpretations in this study.

In the four wells that contain greater than one significant frequency, ASM analysis revealed periodicities consistent with eccentricity, obliquity, and precession periods of the Late Cretaceous. Each of these wells contains at least one eccentricity term, making eccentricity the dominant orbital force identified in this study. The Beech Grove 94H also contains the short obliquity and long precession terms. The resulting sedimentation rate of 8.811 cm/ky is the slowest sedimentation rate of the five wells studied. The Lane 64H contains the short and middle eccentricity terms, and the resulting sedimentation rate of 13.779 cm/ky is the fastest sedimentation rate identified in the study. The Thomas 38H and Soterra 6H both contain the short and long obliquity terms. However, the Soterra 6H contains only the middle eccentricity term, while the Thomas 38H contains the long and short eccentricity terms. The Thomas 38H sedimentation rate of 8.324 cm/ky is similar to that of the Beech Grove 94H, whereas the Soterra

6H sedimentation rate of 12.321 cm/ky is more similar to the maximum sedimentation rate identified in the Lane 64H. The time span expressed in the cored intervals of the studied wells varies from 328 ky to 850 ky. The variance in duration observed between the wells is attributed to variations in cored intervals. The #1 Spinks well from Pike Co., Mississippi provides the most complete core record of the TMS. The nearly complete record of the TMS allows the identification of a zone of enriched TOC content contained in the basal ~100 ft of the TMS. The increase in TOC also coincides with the high resistivity zone that has been identified as a promising target for oil production. Correlation to the studied wells based solely upon the zone of TOC enrichment is inhibited by relatively short coring intervals. However, the stability of the resistivity signatures allows for reasonable interpretation of the carbon enrichment across the studied wells (Figure 33). Additionally, recently acquired unpublished stable carbon isotope data from the #1 Spinks well allows correlation of TOC-enriched zone to published carbon isotope records of OAE 2 and the C/T boundary. Based on well constrained stable carbon isotope records, the TOC-enriched zone represents the recovery period immediately following OAE 2 (Lowery et al., in prep.).

Figure 33 shows the correlation of the enriched zone of TOC. Calculated durations for the recovery period in the TMS range from 212 ky to 251 ky. The shortest duration, observed in the Lane 64H, occurred in the most distal location. TOC-enriched zone durations for wells located more proximally to the sediment source are more tightly varied between 240 ky and 251 ky. Because recovery period durations decrease with distance to the sediment source, a link between deposition and preservation of TOC to continental sediment supply is likely.

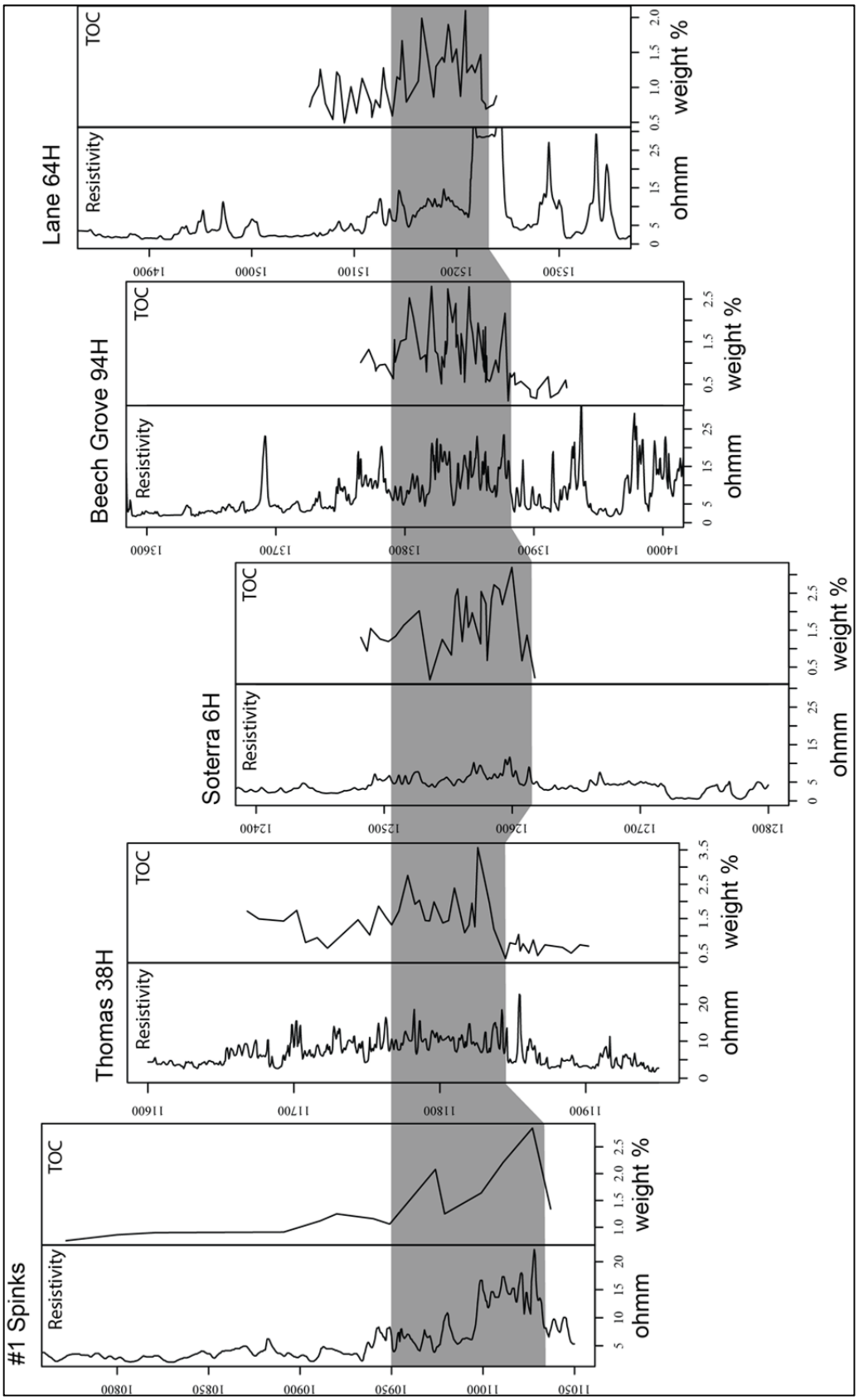

Figure 33: Stratigraphic framework based on TOC content and resistivity. The gray box represents the TOC enrichments in each well.

ANCHORING THE FLOATING TIME SCALE

Recent studies of OAE 2 and the C/T boundary have supplied precise ages for the location of the C/T boundary in geologic time (Meyers et al., 2012, Eldrett et al., 2015). The approximate location is 94 Ma. The C/T boundary also coincides with the approximate termination of OAE 2. By anchoring the end of OAE 2 as established in this study to the C/T boundary at 94 Ma, it is possible to compare geochemical proxies to modeled insolation values projected by Laskar (2004) (Figures 34 through 37).

ORBITAL FORCING OF TMS SEDIMENTATION

The previous sections have identified cyclicity in the TMS, and tied the cyclicity to orbital periods. From these results, the depth series of the cored intervals have been transformed into time series, and anchored upon the termination of OAE 2 near C/T boundary. However, the question of the mechanism of orbital forcing remains.

Variations in the orbital geometry of Earth lead to variations in insolation (Milankovitch, 1941). At the fundamental level, insolation is the mechanism by which orbital geometry affects sedimentation. However, the Earth climate system is complex, with many factors contributing to global climate fluctuations. The Cenomanian climate optimum, characterized by mean sea surface temperatures varying between 30°C and 36°C was likely driven by activation of large igneous provinces and accompanying influxes of CO_2, and augmented by periods of high solar insolation (Wilson, 2002; Hay, 2008; Hay, 2011). Ice-free poles caused a eustatic high that was enhanced by thermosteric expansion of the seas (MacLeod et al., 2013). The resulting third-order transgression of the study area is associated with the flooding of coastal regions and the development of epeiric seas (Hay, 2008; Hay, 2011). While these factors played a role in developing the environment for marine shale deposition landward of the Cretaceous shelf break

in the proto Gulf of Mexico, these processes operated on time-scales greater than the resolution of TMS carbonate content cyclicity identified in this study.

A likely candidate for a more direct mechanism of orbital forcing is variation in primary productivity and the hydrologic cycle in the proto Gulf of Mexico. The increase in TOC during the OAE 2 recovery interval in the TMS appears to be driven by a substantial increase in productivity. As sea level rose and flooded coastal regions, inundated vegetation would have provided sufficient nutrients to support high populations of pelagic organisms. Higher sea water temperature would have also increased productivity in the water column. High rates of water column productivity therefore provided the source for increased TOC deposition. A synchronous increase in carbonate content in the OAE 2 recovery interval supports this theory; high populations of pelagic calcareous organisms led to increased preservation of carbonate content in the studied interval.

As a result of increases in temperature during the OAE 2 recovery, evaporation and precipitation rates would have also increased (Hofmann et al., 2001; Beckmann et al., 2005). Additionally, varying orientation of the dominant surface currents in the proto Gulf of Mexico related to development of the WIS would have varied dominant weather patterns (Johnson, 1999). These fluctuations could have caused variations between a dominantly humid and a more arid hinterland. This, in turn, would have affected hydrolysis rates in the source area. The relationship between humid/arid cycles and sediment supply is shown by geochemical proxies such as the ratio between tectosilicates and phyllosilicates and the ratio between clays formed dominantly via hydrolysis versus physical weathering (Hofmann et al., 2001; Beckmann et al., 2005). Kaolinite and smectite can be considered proxies for chemical weathering via hydrolysis

which is dominant in humid climates, whereas illite can be considered a proxy for physical weathering, which is dominant in more arid climates.

Figures 34 through 37 show a comparison of the proxy data for primary productivity and precipitation rates, as well as insolation for the approximate time period of the OAE 2 recovery. Insolation values depicted are modeled mean summer insolation values for 30°N latitude. Table 3 summarizes cross correlations and associated lag times between variables. Because the cored interval varies in each of the studied wells, slightly different trends are observed. However, when compiled, a single cohesive interpretation is achieved. Cross correlations and lag times are impacted by distortion in proxy feedbacks, particularly in clay proxies for continental weathering. As such, quantitative correlation lag times may not match interpreted, qualitative correlations shown in figures 34 through 37. Cross correlation does not imply causation between the variables, but is included to show plausible positive relationships between the data sets. Each of the wells, with the exception of the Soterra 6H, show a background proxy level for primary productivity and humidity, and an elevated level of primary productivity and humidity that is associated with the OAE 2 recovery interval. Figure 38 shows schematics of these two climate modes.

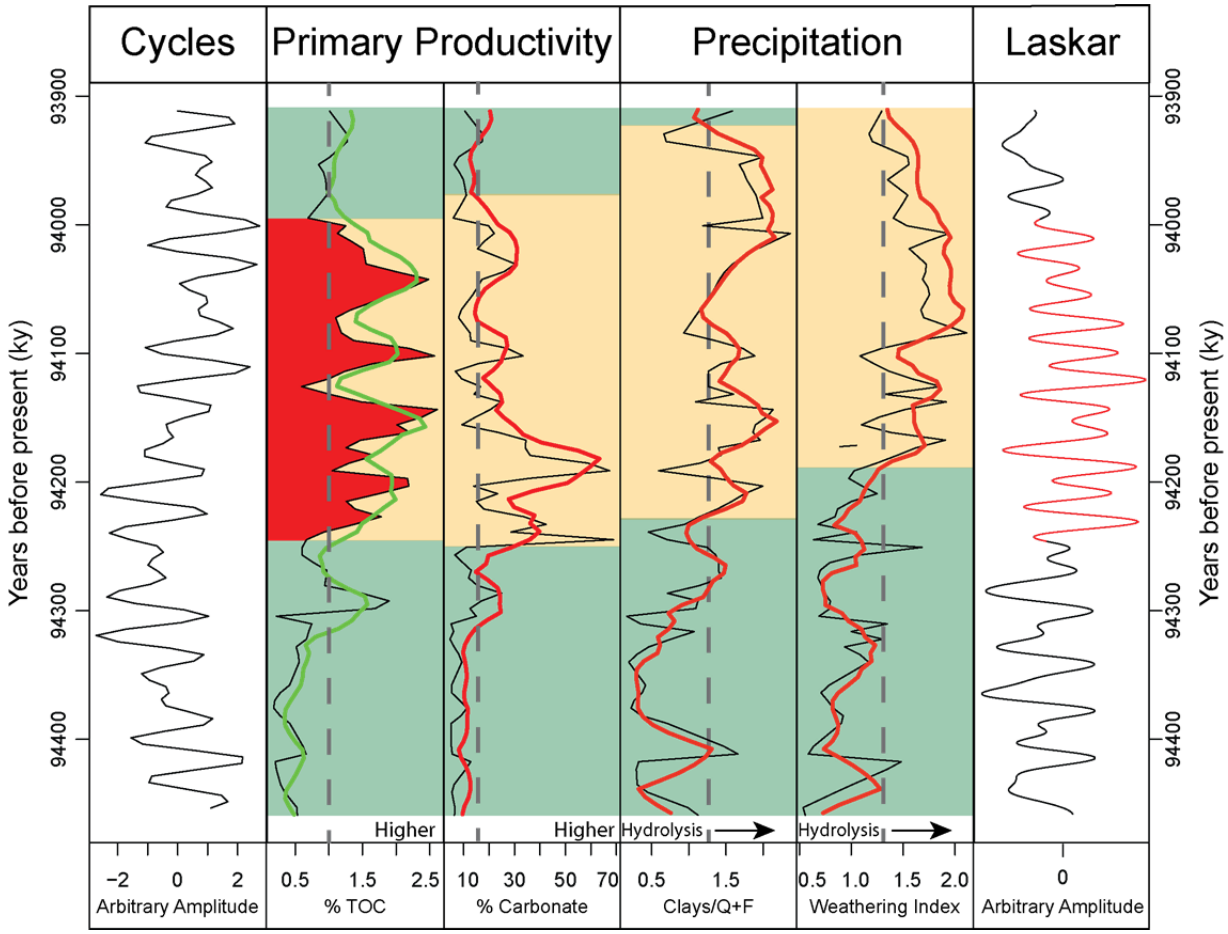

Figure 34: Beech Grove 94H – Comparison of geochemical proxies to convolved cycles identified in MTM analysis and insolation values from Laskar (2004). The TOC interval flagged in red represents the interpreted OAE 2 recovery interval. Gray dashed lines represent the median for each data set, and are used to identify background proxy levels from elevated proxy levels. Black lines are raw data, and red/green lines are five point moving averages of the data. Green areas are interpreted to be more arid, and orange areas are interpreted to be more humid.

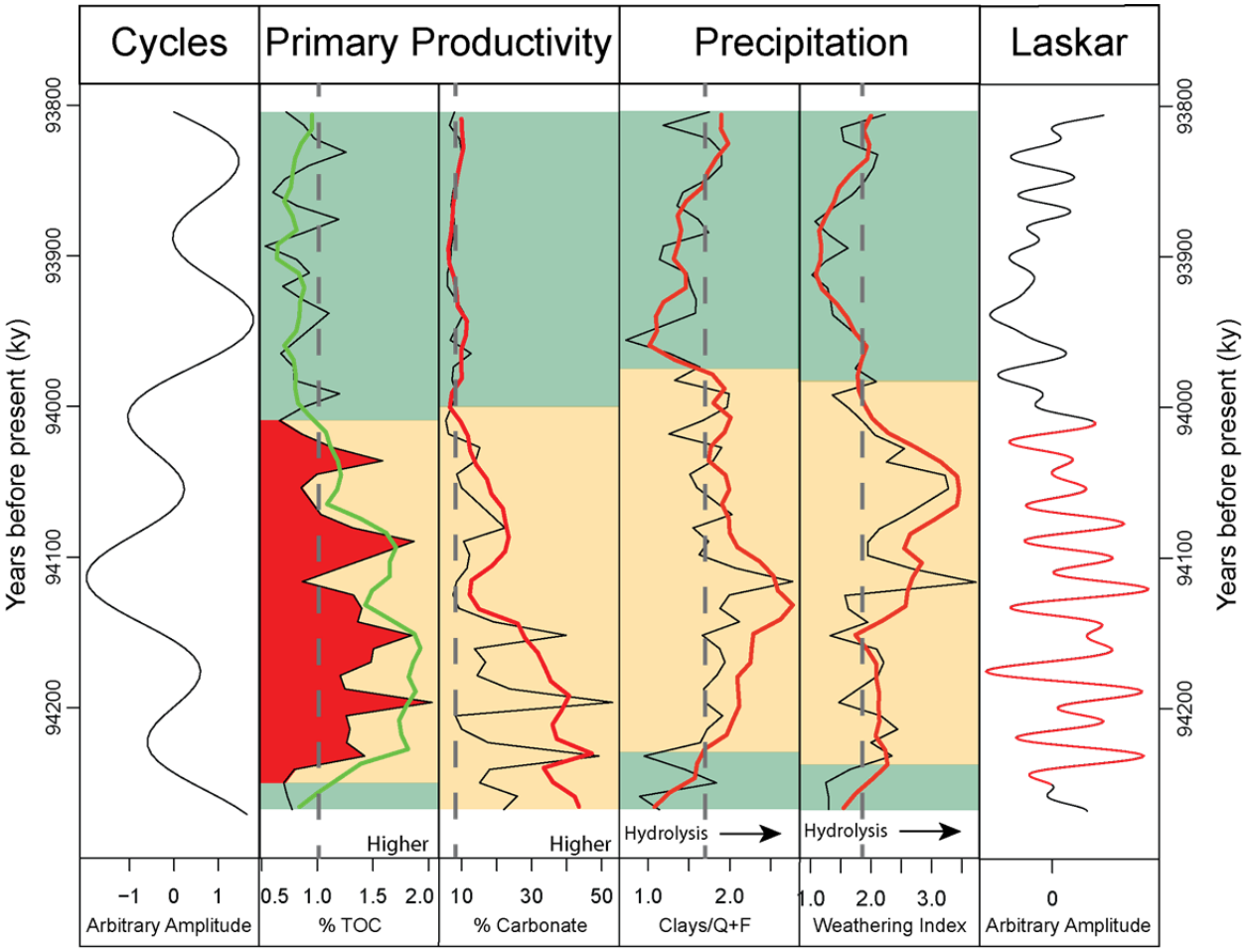

Figure 35: Lane 64H – Comparison of geochemical proxies to convolved cycles identified in MTM analysis and insolation values from Laskar (2004). The TOC interval flagged in red represents the interpreted OAE 2 recovery interval. Gray dashed lines represent the median for each data set, and are used to identify background proxy levels from elevated proxy levels. Black lines are raw data, and red/green lines are five point moving averages of the data. Green areas are interpreted to be more arid, and orange areas are interpreted to be more humid.

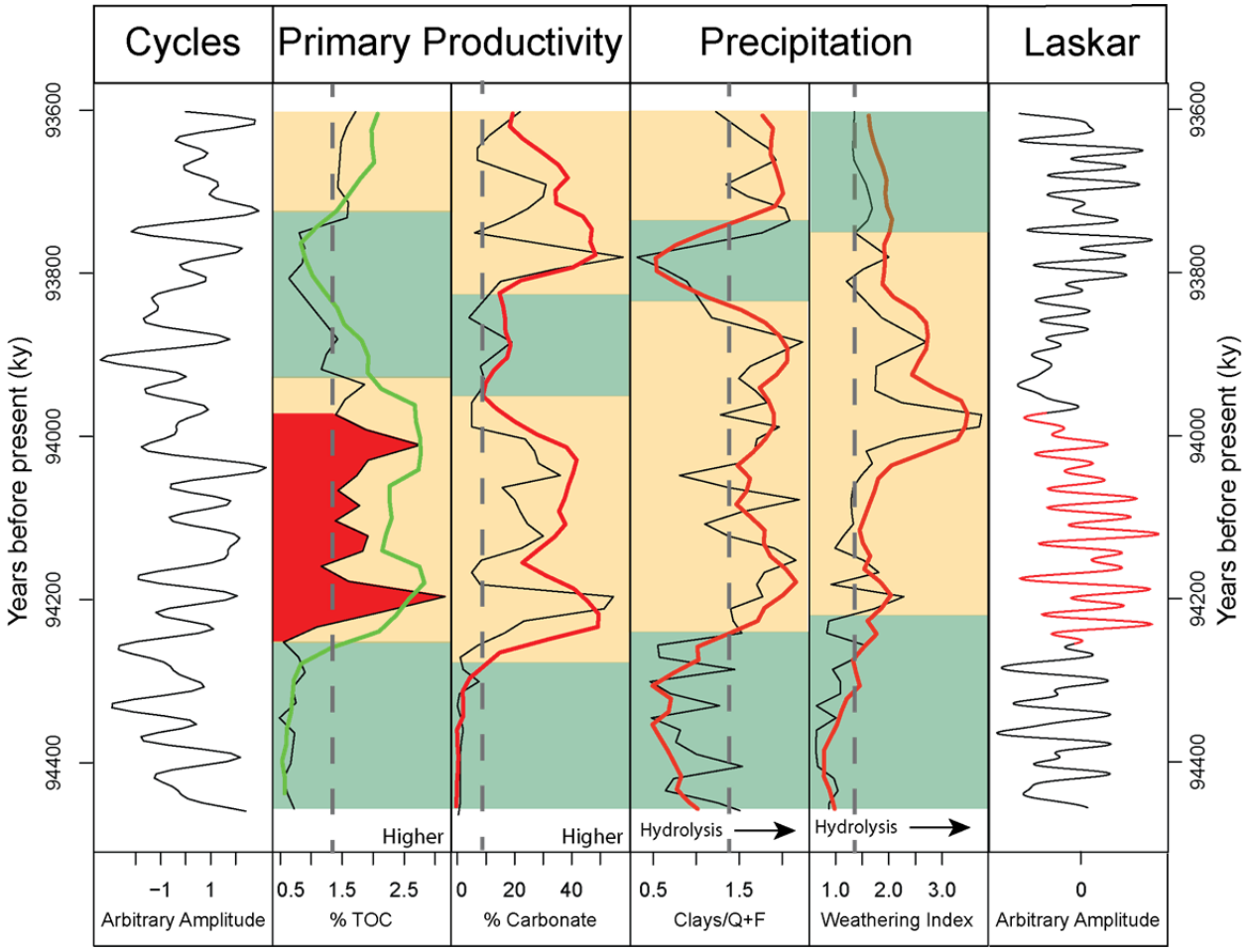

Figure 36: Thomas 38H – Comparison of geochemical proxies to convolved cycles identified in MTM analysis and insolation values from Laskar (2004). The TOC interval flagged in red represents the interpreted OAE 2 recovery interval. Gray dashed lines represent the median for each data set, and are used to identify background proxy levels from elevated proxy levels. Black lines are raw data, and red/green lines are five point moving averages of the data. Green areas are interpreted to be more arid, and orange areas are interpreted to be more humid.

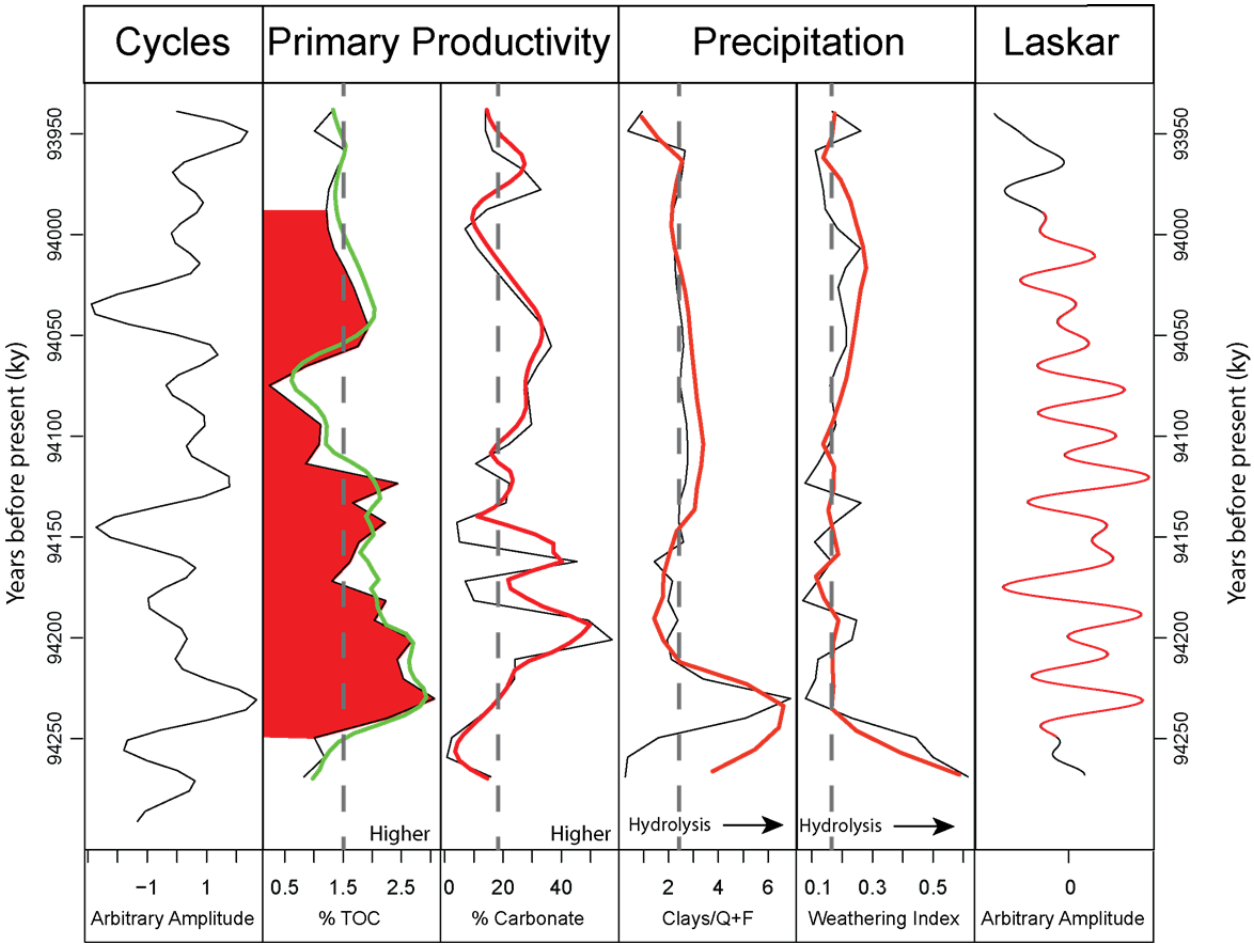

Figure 37: Soterra 6H – Comparison of geochemical proxies to convolved cycles identified in MTM analysis and insolation values from Laskar (2004). The TOC interval flagged in red represents the interpreted OAE 2 recovery interval. Gray dashed lines represent the median for each data set, and are used to identify background proxy levels from elevated proxy levels. Black lines are raw data, and red/green lines are five point moving averages of the data. Because of short cored intervals before, and after OAE 2 recovery, periods of relative and aridity and humidity are not interpreted on the diagram.

Variables (lag in ky)	Carbonate	TOC	Clay/Q+F	WI
Beech Grove 94H				
Insolation	.58 (0)	.73 (0)	.52 (65)	.80 (47)
Lane 64H				
Insolation	.53 (0)	.88 (0)	.78 (0)	.77 (9)
Thomas 38H				
Insolation	.68 (0)	.61 (18)	.49 (36)	.45 (198)
Soterra 6H				
Insolation	.12 (0)	.14 (80)	.43 (0)	.12 (0)

Table 3: Correlation table between insolation values and proxy variables. Insolation values used in cross correlation were modeled global annual averages. Correlation coefficients and lags represent the strongest positive correlation identified. Max lag tested was 20.

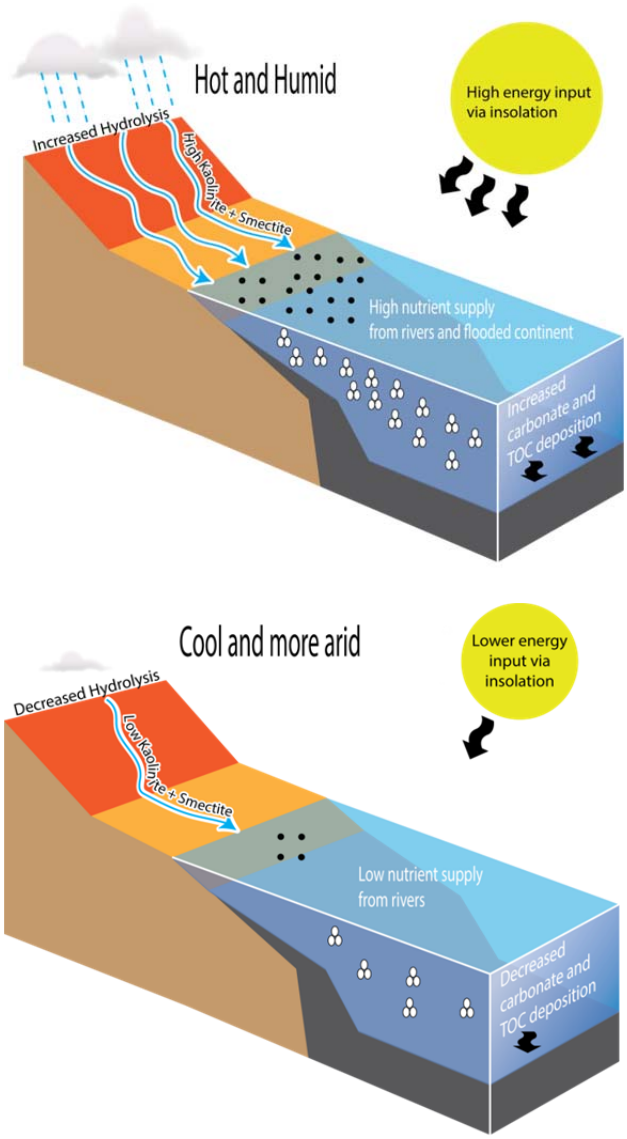

Figure 38: Schematics of the two modes of climate affecting TMS deposition. The Hot and Humid mode is characterized by elevated levels of carbonate, TOC, and clay minerals sensitive to chemical weathering. The Warm and Arid mode is characterized by background levels of TOC and carbonate, and higher levels of clay minerals sensitive to physical weathering.

The Beech Grove 94H and Thomas 38H wells each depict the interval leading up to OAE 2 recovery. This interval is characterized by low levels of primary productivity proxies and sediment supply proxies indicating a more arid environment. At the onset of OAE 2 recovery, an increase in carbonate accompanying the TOC enrichment indicates an increase in primary productivity during the event. The increase in proxy values is correlated with an increase in insolation beginning at ~94,280 ky. Proxy values for precipitation and hydrolysis also increase during OAE 2 recovery, though the increase lags behind both increases in insolation and primary productivity proxies. The lag is likely caused by delays in feedback response such as sediment transport time and slow increases in rates of chemical weathering via hydrolysis.

All of the cored intervals of the studied wells depict the OAE 2 recovery period. Primary productivity proxies indicate that primary productivity peaked relatively quickly and remained above background levels for the duration of the event. Although precipitation/hydrolysis proxies display some fluctuation throughout the recovery, values remain above background levels, indicating a continuously humid climate with high levels of precipitation. The Soterra 6H does not appear to follow this pattern (Table A2, Table A3, Figure A1). However, given the short intervals preceding and following OAE 2 recovery included in the core data, background versus elevated levels of sediment supply proxies are difficult to identify.

The Lane 64H and Thomas 38H display the return of primary productivity and sediment supply proxies to background levels following OAE 2 recovery. Primary productivity proxies return to background levels concurrently with a decrease in insolation. The return of precipitation/hydrolysis proxies to background levels lags behind the primary productivity proxies. This is again likely due to distortion and delays in the feedback response.

VII. CONCLUSION

The TMS has garnered attention in recent years for its potential as an unconventional oil reservoir. The target for oil production has been the basal, high resistivity zone. This section of the TMS is ideal for cyclostratigraphic analysis due to continuous sedimentation and availability of cored sections. MTM and ASM analysis were conducted on five cored intervals in order to determine bulk sedimentation rate in the basal section of the TMS. A sixth cored section from the #1 Spinks well that represents nearly the entire TMS section was used to correlate TOC values between the studied wells. Additionally, proxy geochemical data were used to determine possible mechanisms of orbital forcing in TMS strata. The conclusions of this are summarized below:

1. MTM analysis revealed multiple statistically significant frequencies in carbonate data in four of the five studied wells. The Crosby 12-1H well revealed only one statistically significant frequency and was consequently removed from further analysis.
2. ASM analysis revealed statistically significant correlations between significant frequencies from MTM analysis and modeled orbital periods from the Late Cretaceous. Using these correlations, sedimentation rates were calculated to range from 8.811 cm/ky to 12.321 cm/ky and average 10.332 cm/ky.
3. Using the #1 Spinks well and resistivity data to compensate for short core intervals in the studied wells, TOC-enriched zones were correlated between the wells. These enrichments were interpreted to represent the recovery period following OAE2.

Durations of the OAE 2 recovery were calculated to range from 212 ky to 251 ky. The most distal well location, the Lane 64H, displays the shortest duration of 212 ky. OAE 2 recovery durations in more proximal locations range between 240 ky and 251 ky and average 245 ky. The disparity between distal and proximal locations is interpreted to imply a link between continental runoff and TOC enrichment.

4. The floating timescale developed through ASM and correlation was anchored to the geological time scale using previously published age dates for the termination of OAE 2. An insolation model for this time period was also used to anchor the timescale of the OAE 2 terminus at ~94 Ma.
5. Geochemical proxies for primary productivity and precipitation/hydrolysis were investigated for correlation with orbitally driven insolation changes. Two climate modes affecting deposition were interpreted. First, a background mode with lower temperatures and humidity represented by low primary productivity values and precipitation proxy values. Second, an elevated mode representing the OAE 2 recovery interval characterized by higher proxy values for primary productivity and precipitation/hydrolysis indicates a warmer, more humid climate. Precipitation/hydrolysis proxies tended to lag behind primary productivity and insolation trends, suggesting a more delayed feedback response in continental weathering processes when compared with primary productivity fluctuations.

The conclusions developed in this study reveal opportunities for further research into orbitally driven sedimentation in the TMS. In order to develop a more precise framework for OAE 2 along the US Gulf Coast, a high-resolution stable carbon isotope study should be conducted utilizing the #1 Spinks core because of its near complete representation of the

TMS. Additionally, trace element analysis of the #1 Spinks well would provide a means to test the hypothesis that cyclic TMS deposition was driven by fluctuation in primary productivity and sediment supply. Proxies for redox conditions should be investigated to determine the degree to which water column anoxia may have controlled organic carbon preservation.

LIST OF REFERENCES

AL-HUSSEINI, M.I., 2015, Arabian Orbital Stratigraphy revisited–AROS 2015: GEOARABIA, v. 20, p. 183–216.

ARTHUR, M.A., DEAN, W.E., and PRATT, L.M., 1988a, Geochemical and climatic effects of increased marine organic carbon burial at the Cenomanian/Turonian boundary: Nature, v. 335, p. 714–717, doi: 10.1038/335714a0.

ARTHUR, M.A., JENKYNS, H.C., BRUMSACK, H.-J., and SCHLANGER, S.O., 1988b, Stratigraphy, geochemistry, and paleo-oceanography of organic carbon-rich Cretaceous sequences: NATO Advanced Study Institutes Series. Series C: Mathematical and Physical Sciences, v. 304, p. 75–119.

BABADI, B., and BROWN, E.N., 2014, A Review of Multitaper Spectral Analysis: IEEE Transactions on Biomedical Engineering, v. 61, p. 1555–1564, doi: 10.1109/TBME.2014.2311996.

BECKMANN, B., 2005, Linking Coniacian–Santonian (OAE3) black-shale deposition to African climate variability: a reference section from the eastern tropical Atlantic at orbital time scales (ODP site 959, off Ivory Coast and Ghana): SEPM Special Publication No. 82, p.125–143.

BERGER, A., IMBRIE, J., HAYS, J., KUKLA, G., and SALTZMAN, B., 1984, Milankovitch and climate: understanding the response to astronomical forcing: D. Reidel Publishing Company.

BERGER, A., LOUTRE, M.F., and LASKAR, J., 1992, Stability of the Astronomical Frequencies Over the Earth's History for Paleoclimate Studies: Science, v. 255, p. 560–566.

BRADLEY, W.H., 1930, The varves and climate of the Green River epoch: USGS Numbered Series No. 158, p. 87–110.

BRYANT, W.R., LUGO, J., CORDOVA, C., and SALVADOR, A., 1991, Physiography and bathymetry: The Gulf of Mexico Basin: Boulder, Geological Society of America, Decade of North American Geology, v. J, p. 13–30.

CANTALEJO, B., and PICKERING, K.T., 2014, Climate forcing of fine-grained deep-marine systems in an active tectonic setting: Middle Eocene, Ainsa Basin, Spanish Pyrenees: Palaeogeography, Palaeoclimatology, Palaeoecology, v. 410, p. 351–371, doi: 10.1016/j.palaeo.2014.06.005.

CANTALEJO, B., and PICKERING, K.T., 2015, Orbital forcing as principal driver for fine-grained deep-marine siliciclastic sedimentation, Middle-Eocene Ainsa Basin, Spanish Pyrenees: Palaeogeography, Palaeoclimatology, Palaeoecology, v. 421, p. 24–47, doi: 10.1016/j.palaeo.2015.01.008.

CHAMLEY, H., 1989, Clay sedimentology: Springer-Verlag, London;New York, 623 p.

DE BOER, P.L., and SMITH, D.G., 1994, Orbital forcing and cyclic sequences, International Association of Sedimentologists Special Publication no. 19, Blackwell Scientific Publications.

ELDRETT, J.S., MA, C., BERGMAN, S.C., LUTZ, B., GREGORY, F.J., DODSWORTH, P., PHIPPS, M., HARDAS, P., MINISINI, D., OZKAN, A., RAMEZANI, J., BOWRING, S.A., KAMO, S.L., FERGUSON, K., et al., 2015, An astronomically calibrated stratigraphy of the Cenomanian, Turonian and earliest Coniacian from the Cretaceous Western Interior Seaway, USA: Implications for global chronostratigraphy: Cretaceous Research, v. 56, p. 316–344, doi: 10.1016/j.cretres.2015.04.010.

EWING, T.E., 1991, Structural framework: The Gulf of Mexico Basin: Geological Society of America, The Geology of North America, v. J, p. 31–52.

FOURIER, J, 1822, Theorie analytique de la chaleur: Firmin Didot.

GALLOWAY, W.E., 2008, Depositional evolution of the Gulf of Mexico sedimentary basin: Sedimentary basins of the world, v. 5, p. 505–549.

GILBERT, G.K., 1895, Sedimentary measurement of Cretaceous time: The Journal of Geology, v. 3, p. 121–127.

HAY, W.W., 2011, Can humans force a return to a "Cretaceous" climate? Sedimentary Geology, v. 235, p. 5–26.

HAY, W.W., 2008, Evolving ideas about the Cretaceous climate and ocean circulation: Cretaceous Research, v. 29, p. 725–753.

HAYS, J.D., and PITMAN, W.C., 1973, Lithospheric plate motion, sea level changes and climatic and ecological consequences: Nature, v. 246, p. 18–22.

HAYS, J.D., IMBRIE, J., SHACKLETON, N.J., and OTHERS, 1976, Variations in the Earth's orbit: pacemaker of the ice ages, *in* American Association for the Advancement of Science.

HERSCHEL, J.F.W., 1832, On the Astronomical Causes which may influence Geological Phaenomena.: Transactions of the Geological Society of London, v. 3, p. 293–300.

HOFMANN, P., RICKEN, W., SCHWARK, L., and LEYTHAEUSER, D., 2001, Geochemical signature and related climatic-oceanographic processes for early Albian black shales: Site 417D, North Atlantic Ocean: Cretaceous Research, v. 22, p. 243–257.

HUBER, B.T., NORRIS, R.D., and MACLEOD, K.G., 2002, Deep-sea paleotemperature record of extreme warmth during the Cretaceous: Geology, v. 30, p. 123–126, doi: 10.1130/0091-7613(2002)030<0123:DSPROE>2.0.CO;2.

HUTTON, J., 1788,Theory of the Earth: Transactions of the Royal Society of Edinburgh, v. 1, p. 209–304.

JENKYNS, H.C., 2010, Geochemistry of oceanic anoxic events: Geochemistry, Geophysics, Geosystems, v. 11, p. 1-30, doi: 10.1029/2009GC002788.

JOHNSON, C.C., 1999, Evolution of Cretaceous surface current circulation patterns, Caribbean and Gulf of Mexico: Special Papers-Geological Society of America, p. 329–344.

KUIPER, K.F., DEINO, A., HILGEN, F.J., KRIJGSMAN, W., RENNE, P.R., and WIJBRANS, J.R., 2008, Synchronizing Rock Clocks of Earth History: Science, v. 320, p. 500–504, doi: 10.1126/science.1154339.

KUYPERS, M.M., PANCOST, R.D., NIJENHUIS, I.A., and SINNINGHE DAMSTÉ, J.S., 2002, Enhanced productivity led to increased organic carbon burial in the euxinic North Atlantic basin during the late Cenomanian oceanic anoxic event: Paleoceanography, v. 17, p. 3-1–3-13.

LASKAR, J., 1989, A numerical experiment on the chaotic behaviour of the solar system: Nature, v. 338, p. 237-238.

LASKAR, J., 1990, The chaotic motion of the solar system: a numerical estimate of the size of the chaotic zones: Icarus, v. 88, p. 266–291.

LASKAR, J., 1999, The limits of Earth orbital calculations for geological time-scale use: Philosophical Transactions of the Royal Society of London A: Mathematical, Physical and Engineering Sciences, v. 357, p. 1735–1759.

LASKAR, J., FIENGA, A., GASTINEAU, M., and MANCHE, H., 2011, La2010: a new orbital solution for the long-term motion of the Earth: Astronomy & Astrophysics, v. 532, p. A89.

LASKAR, J., ROBUTEL, P., JOUTEL, F., GASTINEAU, M., CORREIA, A.C.M., and LEVRARD, B., 2004, A long-term numerical solution for the insolation quantities of the Earth: Astronomy & Astrophysics, v. 428, p. 261–285.

LEBEDEL, V., LEZIN, C., ANDREU, B., WALLEZ, M.-J., ETTACHFINI, E.M., and RIQUIER, L., 2013, Geochemical and palaeoecological record of the Cenomanian–Turonian Anoxic Event in the carbonate platform of the Preafrican Trough, Morocco: Palaeogeography, Palaeoclimatology, Palaeoecology, v. 369, p. 79–98, doi: 10.1016/j.palaeo.2012.10.005.

LEES, J.M., and PARK, J., 1995, Multiple-taper spectral analysis: A stand-alone C-subroutine: Computers & Geosciences, v. 21, p. 199–236.

LOWERY, C., 2016, Stable carbon isotope results from the #1 Spinks Well, Manuscript in preparation.

LU, J., RUPPEL, S.C., and ROWE, H.D., 2015, Organic matter pores and oil generation in the Tuscaloosa marine shale: AAPG Bulletin, v. 99, p. 333–357, doi: 10.1306/08201414055.

LYELL, C., 1837, Principles of geology: Being an inquiry how far the former changes of the Earth's surface are referable to causes now in operation: J. Kay, jun. & brother.

MA, C., MEYERS, S.R., SAGEMAN, B.B., SINGER, B.S., and JICHA, B.R., 2014, Testing the astronomical time scale for oceanic anoxic event 2, and its extension into Cenomanian strata of the Western Interior Basin (USA): Geological Society of America Bulletin, v. 126, p. 974–989, doi: 10.1130/B30922.1.

MACLEOD, K.G., HUBER, B.T., BERROCOSO, Á.J., and WENDLER, I., 2013, A stable and hot Turonian without glacial $\delta^{18}O$ excursions is indicated by exquisitely preserved Tanzanian foraminifera: Geology, v. 41, p. 1083–1086.

MALINVERNO, A., ERBA, E., and HERBERT, T.D., 2010, Orbital tuning as an inverse problem: Chronology of the early Aptian oceanic anoxic event 1a (Selli Level) in the Cismon APTICORE: Paleoceanography, v. 25, p. PA2203.

MANCINI, E.A., LI, P., GODDARD, D.A., and ZIMMERMAN, R.K., 2005, Petroleum Source Rocks of the Onshore Interior Salt Basins, North Central and Northeastern Gulf of Mexico: v. 55, p. 486–504.

MANCINI, E.A., OBID, J., BADALI, M., LIU, K., and PARCELL, W.C., 2008, Sequence-stratigraphic analysis of Jurassic and Cretaceous strata and petroleum exploration in the central and eastern Gulf coastal plain, United States: Aapg Bulletin, v. 92, p. 1655–1686.

MANCINI, E.A., and PUCKETT, T.M., 2005, Jurassic and Cretaceous transgressive-regressive (TR) cycles, northern Gulf of Mexico, USA: Stratigraphy, v. 2, p. 31–48.

MANCINI, E.A., PUCKETT, T.M., and TEW, B.H., 1996, Integrated biostratigraphic and sequence stratigraphic framework for Upper Cretaceous strata of the eastern Gulf Coastal Plain, USA: Cretaceous Research, v. 17, p. 645–669.

MATTHEWS, R.K., and AL-HUSSEINI, M.I., 2010, Orbital-forcing glacio-eustasy: A sequence stratigraphic time scale: GeoArabia, v. 15, p. 155–167.

MATTHEWS, R.K., and FROHLICH, C., 2002, Maximum flooding surfaces and sequence boundaries: comparisons between observations and orbital forcing in the Cretaceous and Jurassic (65–190 Ma): GeoArabia, v. 7, p. 503–538.

MEYERS, S.R., 2014, Astrochron: An R package for Astrochronology. http://cran.r-project.org/package=astrochron.

MEYERS, S.R., and SAGEMAN, B.B., 2007, Quantification of deep-time orbital forcing by average spectral misfit: American Journal of Science, v. 307, p. 773–792.

MEYERS, S.R., SAGEMAN, B.B., and ARTHUR, M.A., 2012, Obliquity forcing of organic matter accumulation during Oceanic Anoxic Event 2: Paleoceanography, v. 27, p. PA3212, doi: 10.1029/2012PA002286.

MEYERS, S.R., SAGEMAN, B.B., and HINNOV, L.A., 2001, Integrated Quantitative Stratigraphy of the Cenomanian-Turonian Bridge Creek Limestone Member Using Evolutive Harmonic Analysis and Stratigraphic Modeling: Journal of Sedimentary Research, v. 71, p. 628–

644, doi: 10.1306/012401710628.

MILANKOVITCH, M., 1941, Kanon der Erdebestrahlung und seine Anwendung auf das Eiszeitenproblem: Königlich Serbische Akademie.

PRATT, L.M., and KING, J.D., 1986, Variable marine productivity and high eolian input recorded by rhythmic black shales in Mid-Cretaceous pelagic deposits from central Italy: Paleoceanography, v. 1, p. 507–522.

RAHIM, K., 2014, Applications of Multitaper Spectral Analysis to Nonstationary Data: http://qspace.library.queensu.ca/handle/1974/12584. Checked October 2016.

SAGEMAN, B.B., MEYERS, S.R., and ARTHUR, M.A., 2006, Orbital time scale and new C-isotope record for Cenomanian-Turonian boundary stratotype: Geology, v. 34, p. 125–128.

SAGEMAN, B.B., RICH, J., ARTHUR, M.A., BIRCHFIELD, G.E., and DEAN, W.E., 1997, Evidence for Milankovitch periodicities in Cenomanian-Turonian lithologic and geochemical cycles, Western Interior USA: Journal of Sedimentary Research, v. 67, p. 286–302.

SALVADOR, A., 1991, Origin and development of the Gulf of Mexico basin: The Gulf of Mexico basin, p. 389–444.

SAMES, B., WAGREICH, M., WENDLER, J.E., HAQ, B.U., CONRAD, C.P., MELINTE-DOBRINESCU, M.C., HU, X., WENDLER, I., WOLFGRING, E., YILMAZ, I.Ö., and ZORINA, S.O., 2016, Review: Short-term sea-level changes in a greenhouse world — A view from the Cretaceous: Palaeogeography, Palaeoclimatology, Palaeoecology, v. 441, Part 3, p. 393–411, doi: 10.1016/j.palaeo.2015.10.045.

SCHLANGER, S.O., and JENKYNS, H.C., 1976, Cretaceous oceanic anoxic events: causes and consequences: Geol. Mijnbouw, v. 55, p. 179–185.

SCHWARZACHER, W., 1993, Cyclostratigraphy and the Milankovitch theory: Elsevier.

SLEPIAN, D., 1968, A numerical method for determining the eigenvalues and eigenfunctions of analytic kernels: SIAM Journal on Numerical Analysis, v. 5, p. 586–600.

SLOSS, L.L., 1963, Sequences in the cratonic interior of North America: Geological Society of America Bulletin, v. 74, p. 93–114.

SOHL, N.F., MARTINEZ, R.E., SALMERON-URENA, P., and SOTO-JARAMILLO, F., 1991, Upper Cretaceous: The Gulf of Mexico basin: Boulder, Colorado, Geological Society of America, Geology of North America, v. J, p. 205–244.

THOMSON, D.J., 1982, Spectrum estimation and harmonic analysis: Proceedings of the IEEE, v. 70, p. 1055–1096.

TISSOT, B., and WELTE, D.H., 1978, Petroleum occurrence and formation: Springer-Verlag: Heidelberg.

VAN BENTUM, E.C., REICHART, G.-J., and SINNINGHE DAMSTÉ, J.S., 2012, Organic matter provenance, palaeoproductivity and bottom water anoxia during the Cenomanian/Turonian oceanic anoxic event in the Newfoundland Basin (northern proto North Atlantic Ocean): Organic Geochemistry, v. 50, p. 11–18, doi: 10.1016/j.orggeochem.2012.05.013.

VELDE, B. (ed.), 1995, Origin and mineralogy of clays: Springer, Berlin ; New York, 1 p.

WALTHAM, D., 2015, Milankovitch period uncertainties and their impact on cyclostratigraphy: Journal of Sedimentary Research, v. 85, p. 990–998.

WEAVER, C.E., 1989, Clays, muds, and shales: Elsevier : Distributors for the U.S. and Canada, Elsevier Science Pub. Co, Amsterdam ; New York, 819 p.

WENDLER, J.E., and WENDLER, I., 2015, What drove sea-level fluctuations during the mid-Cretaceous greenhouse climate? Palaeogeography, Palaeoclimatology, Palaeoecology, v. 441, p. 412–419.

WENDLER, J.E., WENDLER, I., VOGT, C., and KUSS, J., 2016, Link between cyclic eustatic sea-level change and continental weathering: Evidence for aquifer-eustasy in the Cretaceous: Palaeogeography, Palaeoclimatology, Palaeoecology, v. 441, Part 3, p. 430–437, doi: 10.1016/j.palaeo.2015.08.014.

WIGNALL, P.B., 1994, Black shales: Clarendon Press ; Oxford University Press, Oxford : New York, 127 p.

WILSON, P.A., NORRIS, R.D., and COOPER, M.J., 2002, Testing the Cretaceous greenhouse hypothesis using glassy foraminiferal calcite from the core of the Turonian tropics on Demerara Rise: Geology, v. 30, p. 607–610, doi: 10.1130/0091-7613(2002)030<0607:TTCGHU>2.0.CO;2.

APPENDIX

Well Name	Frequency (cycles/meter)	MTM Confidence (%)	Periodicity (ky)	Orbital Cycle
Beech Grove 94H				
	0.02845249	96.292	398.891	Eccentricity (L)
	0.1341332	92.103	84.613	Eccentricity(S)
	0.3536238	94.994	32.095	Obliquity(S)
	0.4836923	92.167	23.464	Precession(L)
	0.6056315	95.964	XXX	XXX
S (cm/ky)			8.811	
ASM			0.002	
H_0			0.315	
p-value			0.003	
Lane 64-H				
	0.02461522	95.577	444.235	Eccentricity (L)
	0.1019773	94.128	107.229	Eccentricity(M/S)
	0.2250535	91.213	48.588	Obliquity(L)
	0.2883497	95.402	37.922	Obliquity(S)
S (cm/ky)			9.145	
ASM			0.00017	
H_0			0.002	
p-value			$2x10^{-5}$	
Thomas 38H				
	0.03022026	96.243	397.53	Eccentricity (L)
	0.1456067	91.118	82.506	Eccentricity(S)
	0.2307729	92.607	52.057	Obliquity(L)
	0.3076972	90.43	39.043	Obliquity(S)
S (cm/ky)			8.324	
ASM			0.0009	
H_0			0.825	
p-value			0.00825	
Soterra 6H				
	0.0652918	97.38763	144.285(?)	Eccentricity(M)
S (cm/ky)			10.615(?)	
ASM			0	
H_0			5.922	
p-value			0.05922	
Crosby 12-1H				
	0.179733	92.01301	48.014(?)	Obliquity(L)
S (cm/ky)			11.588(?)	
ASM			0	
H_0			9.655	
p-value			0.0966	

Table A1: Results of MTM and ASM analysis, as in Table 2, but using spline interpolation.

	Degrees of Freedom	Sum of Squares	Mean of Squares	F-Value	P-values
Carbonate Concentration	4	3490	872.45	3.6754	0.006
Residuals	221	52460	237.37		

Table A2: ANOVA table calculated from percent carbonate data from the five studied wells.

Relationship	Difference	Lower	Upper	p-adjusted
Crosby-BG	-8.5572855	-18.673634	1.5590629	0.1403969
Lane-BG	-6.0494595	-13.8070646	1.7081457	0.2050452
Soterra-BG	3.9575405	-5.2143291	13.1294102	0.7589844
Thomas-BG	-5.0563982	-12.8611006	2.7483042	0.3867312
Lane-Crosby	2.5078261	-8.1687058	13.184358	0.9672303
Soterra-Crosby	12.5148261	0.7704194	24.2592328	0.0303423
Thomas-Crosby	3.5008873	-7.2099145	14.2116891	0.8970347
Soterra-Lane	10.007	0.2207331	19.7932669	0.0422747
Thomas-Lane	0.9930612	-7.5252254	9.5113478	0.9976982
Thomas-Soterra	-9.0139388	-18.8375818	0.8097042	0.0890776

Table A3: Results of Tukey's Honest Significant Difference test on ANOVA results from Table A2. The Soterra 6H well is the clearest source of differing variance among the studied wells.

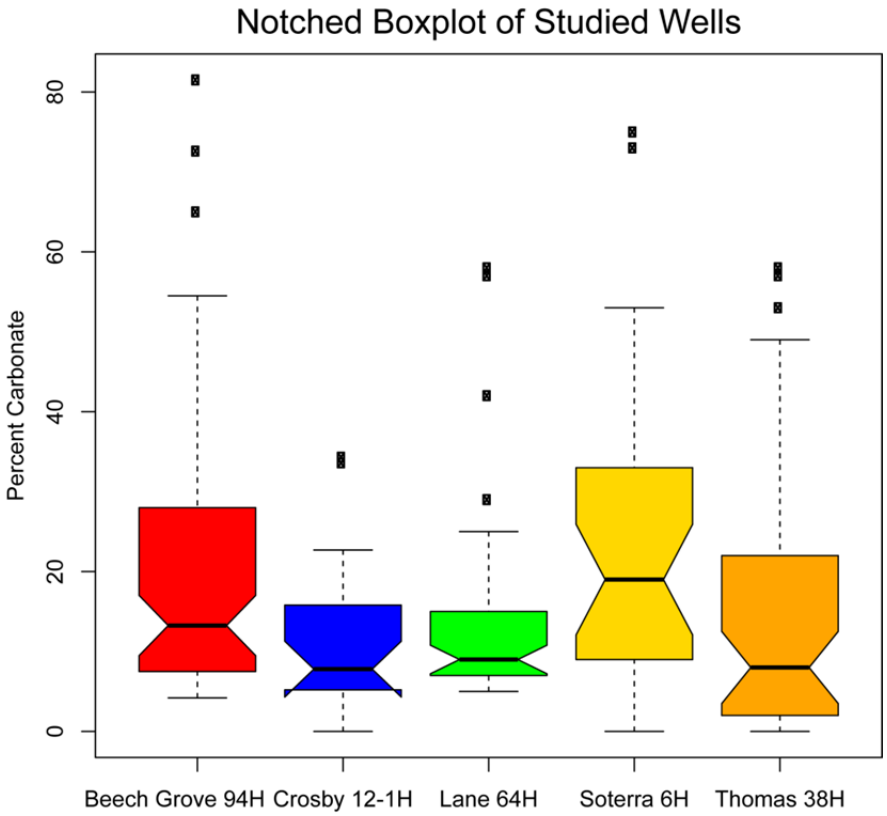

Figure A1: Notched boxplot of studied wells.

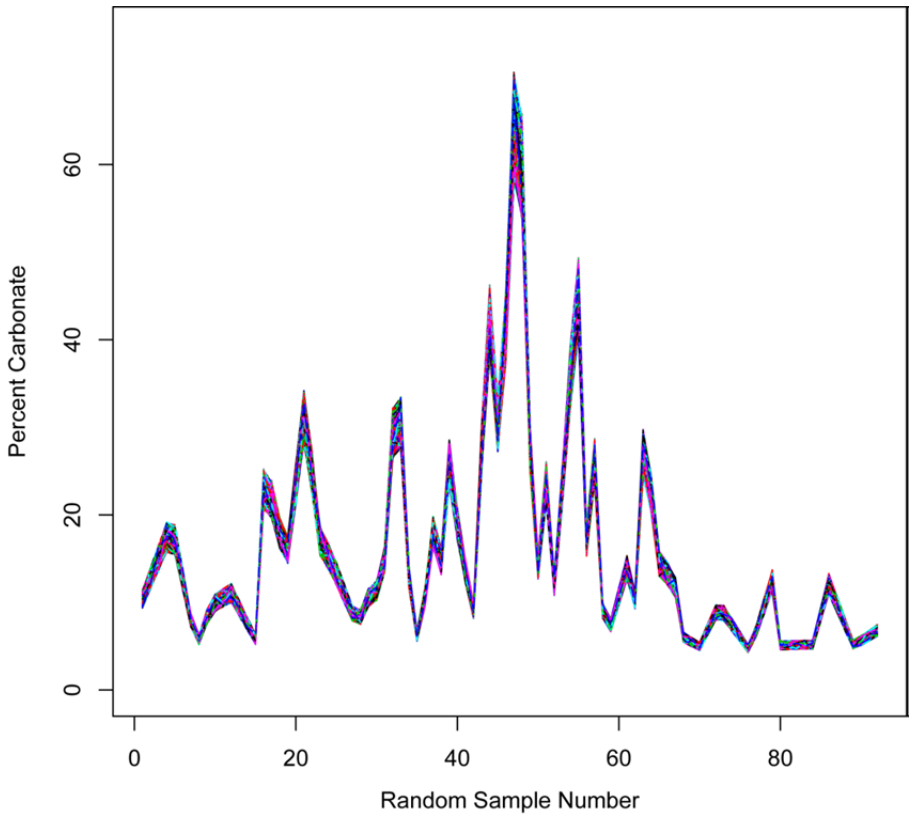

Figure A2: 1000 random samples taken between 10% confidence intervals of laboratory data points for the Beech Grove 94H.

VITA

Christian Kunhardt graduated from St. Paul's high school in Baltimore, Maryland in 2006. He earned a Bachelor's degree in Geosciences from Hamilton College in Clinton, NY where he also played lacrosse and sang in the a capella group The Buffers. After graduating in 2010, Christian entered the workforce as a Field Geologist monitoring drilling operations in the Marcellus Shale. Upon promotion, he gained experience with the geology of many of the major unconventional reservoirs in the continental United States, including: the Eagle Ford shale, the Barnett shale, the Haynesville shale, the Niobrara Formation, the Mississippian limestone, and the Utica shale. In the fall of 2014, Christian enrolled in the graduate program at the University of Mississippi for Geology and Geological Engineering where he earned his Master of Science in 2016. Christian's career and research interests include responsible energy resource development, mudstone geochemistry, and paleoclimate reconstruction.